Understanding the Cloud Structure on the Giant Planets

by

Kristen M. Mihalka

A dissertation submitted in partial fulfillment
of the requirements for the degree of
Doctor of Philosophy
(Atmospheric and Space Sciences)
in The University of Michigan
2012

Doctoral Committee:

Professor Sushil K. Atreya, Chair
Emeritus Professor William R. Kuhn
Associate Professor Edwin Anthony Bergin
Senior Scientist Mark D. Hofstadter, Jet Propulsion Laboratory

For my loving husband and family

ACKNOWLEDGMENTS

I have been told many times that this is the hardest section of the thesis to write. Sure enough one sentence in I am already have a difficult time. I am going to start at the beginning and would like to thank God and my parents for everything that they have done to help get me to this point. It is not often that we thank people for all that they have done, but I am very grateful for all that my parents have done. From encouraging me from an early age to enjoy learning to always physically being there for me, I honestly can not thank them enough. I also very much appreciate them sending me to space camp, despite the fact that it was my brother that wanted to go. Now I am very grateful for them always being interested in what I do and trying to understand what it is I actually do. I would be remise if I did not also thank my brother Matthew for all that he has done for me. I am glad that we went through graduate school at the same time. He understood what I was going through, and was always there to listen and to encourage me to do what ever made me happy.

There are a slew of teachers that have also inspired me over the years. First and foremost I need to thank my 5th grade teacher that first introduced me to weather. While I know it was part of the curriculum, I was truly inspired by what I learned. I still have the weather map that I made in 5th grade in a closet. I would also like to thank the Kansas City locale meteorology Gary Lesak for coming to my elementary school after I

wrote him a letter with the corniest line ever in it, "you make even a cloudy day seem sunny". Watching the weather report in Kansas City, means more then it does in other cities. They take the time to teach you about why weather is happening, and I am grateful for them teaching me every morning and evening. My high school calculus teacher Ms. Mullins also deserves praise as she encouraged me. Once I got to collage I was very thankful that she convinced me to take Calc 2 in high school even though I didn't get a chance to stage craft. I can see now that it was much better for me to take that class in a small setting as I believe calc 2 is the hardest of all the Calculus.

In undergrad, I loved my small department at the University of Missouri, and I'm glad that my parents convinced me last minute to apply. And while I based my decision of going to Mizzou based off of the fact that there scholarship form was easier, I'm now proud to be a tiger. Mizzou offered me the small department that I never knew I wanted and I hope that eventually they will get the fourth professor that we have been trying for for years. I would like to thanks my advisor Dr. Patrick Market. He is one of the best teachers I have ever had, and really knew how to explain things in a way that made you excited. I would also like to thank him for encouraging me in taking research internships. When I first told him that I wanted to be a broadcast meteorologist he looked at me like I was nuts. Dr. Lupo and Dr. Fox also did a lot to encourage me, including helping me study abroad. I really wouldn't trade that time for anything. It was such a growing experience, and I really appreciated all I learned and the time to see the world a little more. The students in the department did a lot to make my time there more manageable and fun especially Willie Gilmore, Christina Crowe, Chris Shultz, Marc Dahmer, Colleen Heck, Emily Sutton and Natalie Stool. Many of these people were storm chase partners,

and Marc even had to deal with my mom's threatening looks when he picked me up for a chase. Christina kept me striving to do more, and Natalie helped me get my abs on.

In graduate school I owe a lot to my committee, and especially my advisor. I would like to thank Dr. Sushil Atreya. He was there for me when I thought the world ended when MSL was postponed, and I had to find a new thesis. He has also giving me many incites on not only planetary science, but also the state of the field and is always willing to help me develop my future career. Dr. William Kuhn's help is something that I greatly appreciated. Whether it was comments on a paper, or an interesting mind test he always gave me something to think and learn about. Dr. Mark Hofstadter was gracious enough to allow me to use his code, and worked with me to make sure that I really understood what his code was doing. I would like to thank Dr. Edwin Bergins for agreeing to be on my committee and his incite on my Thesis. Finally, I would like to thank Dr. Paul Mahaffy for allowing me the opportunity to work with SAM during my first year as a graduate student.

I need to also thank my friends both in graduate school and before. I would like to thank my high school girls for being there to put a smile on my face, and to at least try to understand what graduate school is all about. I would also like to thank the 11 different officemates I've had over the years that kept me entertained. Then there are my fellow comrades that waged the war on gradschool together on this ship we call friend. I would like to thank my entire year of graduate students for the hours of tailgating, the apple to apples, the bang, and the tea times. Thanks go out to Kevin Reed, Jacob Gruesbeck, Matt Trantham, Paul Ulrich, and Sid Mishra. A special thanks goes out to all of those who I played broomball with despite the fact that I had to be up to odd hours of the night. I really love the sport. Of course I also need to thank Daniel Gershman for

his friendship and robot shopping. I would also like to thank Tami McDunn and Amanda Brecht for being there for me when I needed female time in a department filled with men. Finally, I would like to thank Susan Cheng who despite only being here for the last two years really made my graduate school experience better.

This last paragraph goes out to my husband Ahmed Tawfik. There really are no good words to describe how much support this man has given me over there years. From the very beginning he was there for me when I got frustrated, and always allowed me to bounce my ideas off of him. Thank you for forever encouraging me to do what I wanted to do and for loving me. I feel very lucky that we both ended up at Michigan, and am very excited to see where life takes us from here.

TABLE of CONTENTS

LIST OF FIGURES

LIST OF TABLES

LIST OF APPENDICES

Chapter 1 : INTRODUCTION

1.1 Overview of Dissertation

Research into the clouds of the giant planets make up the bulk of this work. Chapter 1 surveys the research on the Solar System origin and atmospheres of these planets, including their thermal profile and atmospheric composition. In Chapter 2, the Equilibrium Cloud Condensation Model, ECCM, and the updates that have been made to this model are examined, including an examination of how the lapse rate is calculated and the application of cloud microphysics. Chapter 3 details the basic radiative transfer principles, the derivation of phosphine's saturated vapor pressure equation, and the VLA data. The addition of phosphine to the radiative transfer code and the coupling of the radiative transfer model with the cloud code and the fits found to match the VLA data are also examined. In Chapter 4, the results from the changes made in Chapter 2 and the fits found in Chapter 3 are related to each other. In the final chapter, conclusions and suggestions for future research are presented. Appendix A details the numerical method for the cloud code, and Appendix B defines the variables and acronyms used.

1.2 History of the Ice Giants

Before the invention of the telescope over four centuries ago, mankind thought there were only six planets. After its invention, numerous planets have been discovered both in and out of our Solar System; thus, expanding the final frontier. In 1781, William Herschel was the first to discover a planet with a telescope. Herschel chose to name the planet Gerogium Sidus, in honor of his benefactor King George III of England, but this decision was not viewed favorably outside of England. Thus, the planet was renamed Uranus, a Latinized version of the Greek god of the sky, Ouranos. It took another 65 years before Urbain Le Verrier, John Couch Adams, and Johann Galle discovered the next planet, Neptune, independently in 1846. Neptune was not found by randomly searching the sky, but instead through Alexis Bouvard's mathematical predictions that were derived to explain Uranus' odd orbital behavior. Neptune only orbits the Sun once every 165 years, and is only now completing its first full orbit since discovery. The 1846 observation is not actually the first documented observation of Neptune, as Galileo Galilee accidentally observed the planet in 1612 while examining Jupiter's moons. Galileo did not recognize it as a planet, and thus, it was not officially recognized as a planet until 234 years later.

The giant planets have similar composition to each other. However, Uranus and Neptune have a lower gas to ice ratio than Jupiter and Saturn. The gas giants, Jupiter and Saturn, are composed primarily of hydrogen and helium with only traces of other species, such as hydrocarbons, ammonia, and water. The ice giants, Uranus and Neptune, are composed of hydrogen and helium as well, but also have a higher

proportion of "ices" such as water, ammonia, and methane. Furthermore, the interior of the ice giants are believed to be composed of ices, while the interiors of the gas giants are thought to be composed primarily of metallic hydrogen. The ice giants have been relatively ignored compared to their "big brothers," the gas giants. The only data for Uranus and Neptune is from Voyager 2 spacecraft observations and Earth-based observations. Research is still performed with this limited data set because these planets are of great importance.

Uranus' atmosphere is relatively featureless compared to Neptune's, with its more active visible weather patterns. While Jupiter is famous for its Great Red Spot, Neptune had its own Great Dark Spot, which was large enough to fit Earth inside of it. When Voyager 2 flew by Neptune in 1989 the spot was visible, but it disappeared by the time Hubble tried imaging the spot in November of 1994 (Baines *et al.*, 2002). The Great Dark Spot, unlike the Great Red Spot, was a cloudless region of the atmosphere. There are many cloud features observed on Neptune, which are indicative of how dynamic Neptune is even though it only receives 3% the sunlight Jupiter receives. The basic characteristics of all of the giant planets and how they compare to Earth can be viewed in Table 1.1.

Table 1.1 Basic orbital characteristics of Earth compared to the giant planets.

Characteristics of the outer planets and comparison with the Earth

	Earth	Jupiter	Saturn	Uranus	Neptune
Mean distance from Sun (AU)	1.000	5.204	9.582	19.2011	30.047
Mass, M (10_{24} kg)	5.975	1,898.6	568.46	86.832	102.43
Equitorial Raduis, R_E (km)	6,378	71,492	60,268	25,559	24,764
Ellipicity	0.00335	0.06487	0.09796	0.02293	0.01708
Mean Density (gm cm-3)	5.515	1.326	0.687	1.27	1.638
Equatorial surface gravity (cm s-2)	978	2479	1044	878	1115
Escape velocity (km s-1)	11.19	59.5	33.5	21.3	23.5
Equatorial rotation period (h)	23.9345	9.841	10.233	17.24	16.11
Orbital sidereal period (yrs)	1.00	11.8623	29.457	84.011	164.79
Inclination of equator (degrees)	23.45	3.13	26.73	97.77	32
Temperature at 1 bar (K)	273	165	134	76	72

All of the giant planets have clouds present in their atmospheres. The Equilibrium Condensation Cloud Model, ECCM, is often used to model cloud structures using hydrostatic equilibrium and thermodynamics (Lewis, 1969; Weidenschilling and Lewis, 1973; Atreya and Romani, 1985). There are only sources for the clouds in the model and no sinks, namely precipitation, and detrainment. When applied to Earth, the ECCM predicted clouds that were three orders of magnitude greater in concentration than the clouds observed on Earth. To remedy the higher than expected cloud concentrations, microphysics was added to the model and will be further explored in Chapter 2.

1.3 Solar System Theory of Formation

By understanding the composition of the giant planets, we can work toward better understanding of the Solar System's formation. Two models of planetary formation are examined in this section: core accretion, and condensate due to gravitational instabilities in the protoplanetary disk. The core accretion model is more widely accepted. The core accretion model and gas instability model are summarized in Figure 1.1. Current observations and simulations both support and conflict with each of the models, therefore, further study and examination is needed. Each model will be discussed individually, and then the implications to Uranus' formation. The elemental abundances in the upper troposphere of the Uranus will be examined in Chapter 3. These elemental abundance are correlated to Solar System formation models as giant planets further from the Sun are expected to be more enriched in ices than those closer to the Sun. If this trend is not seen in the giant planets in the troposphere, than a loss mechanism, such as a deep ionic ocean (Chapter 4), may be needed.

1.3.1 Core Accretion

The core accretion model requires that the giant planets accrete an initial terrestrial rocky core through the agglomeration of dust and particles from the original protoplanetary disk. The agglomeration of dust builds up and forms planetesimals. Collisions and coagulations of these planetesimals resulted in the formation of the dense core, 5-10 Earth masses (Klahr and Bodenheimer, 2006). Current equation of state calculations predict that the present day core mass of Jupiter is approximately three Earth masses (Saumon and Guillot, 2004), though the original core may have been larger

(Saumon and Guillot, 2004; Guillot, 2005). Once the core formed, a gaseous envelope that surrounded the core formed from gravitationally capture of remaining gases in the protoplanetary disk. The core accretion model was first proposed by Safranov (1969). His work resulted in the foundation for the minimum mass of the solar nebula needed to form the Solar Systtem, and an equation for the rate of accretion of the planetesimals. Models using core accretion have been able to produce Jupiter and Saturn simultaneously in the same system. They also have the planets at approximately the right distances from the Sun, and with the appropriate enrichment of heavy species as compared to the Sun (Alibert *et al.*, 2005). Furthermore, planets and moons continue to be bombarded by meteors, asteroids, and comets, proving that the process of accretion is still active in the Solar System.

The atmospheres of both Jupiter and Saturn contain enriched concentrations of heavy elements as compared to the Sun, as will be discussed in greater detail in section 1.4. Observations of planets around other stars support this pattern of enriched species as stars with higher metallicity have been found more likely to have planets orbiting them. (Udry and Santos, 2007). However, this trend may be due to an observational bias since most exoplanet searches target stars of higher metallicity. Higher metallicity favors the core accretion model because it raises the surface density of the solids and dramatically increases the growth of the core (Pollack *et al.*, 1996). Conversely, it increases the opacity, which hinders planets' formation in the gravitational instability model by making it harder for the atmospheres to collapse (Podolak, 2003). Further study of exoplanets is needed to call this a true trend.

Computer simulations have been performed to support the core accretion model. The previously mentioned study by Alibert *et al.* (2005) showed that the metallicity and

location of Jupiter and Saturn could be produced simultaneously. It is one of the few models to have successfully created two giant planets. Their model found that in order for Saturn to form, Jupiter's creation would have had to precede its creation by 0.2 million years. Saturn's embryo would have formed at a distance of 11.9 AU. Model simulations have been performed to address how planetesimals are created. Johansen *et al.* (2006) showed how boulder-sized objects can quickly accumulate in zones of high pressure turbulent gas and become gravitationally bonded. The work of Johansen *et al.* work elucidated how the cores could have formed.

Once we accurately model the formation of Jupiter and Saturn, the formation of the ice giants still needs to be considered. Wucheterl's (1995) hydrostatic model presented a way to create both Uranus and Neptune using core accretion. Through using mixing length theory and a critical core mass of 15 Earth masses, Wucherterl created a gas envelope that pulsated. This pulsation resulted in mass loss and continued until a quasi-equilibrium state was achieved between gravitational accretion of nebular gas and loss during pulsation. The planets that resulted from this pulsation had similar properties to Uranus and Neptune, proving that the core accretion model contains mechanisms for creating all the giant planets.

The outstanding problem of the core accretion model is it takes time to form cores of 5 to 15 Earth masses, vary from 100 million years (Ikoma *et al.*, 2000) to 1 million years (Alibert *et al.*, 2005). This degree of variance is due to the unknowns about the protoplanetary nebula, such as the gas to dust ratio, disk density distribution, disk opacity, and the role of migration of the planetary cores. The time scale for a star to lose its circumstellar disk has been found to vary from as little as 0.1 million years for stars in the Orion Nebula (Richling *et al.*, 2006) to as long as 30 million years (Haisch *et al.*, 2001).

Therefore, it is difficult to determine if there was enough time for core accretion to take place based on the variable lifetimes found for circumstellar disks. The long lifetime required for the core accretion theory is its major outstanding problem.

1.3.2 Gravitational Instability

The gravitational instability model creates planets via a direct collapse of the solar nebula under its own gravity due to experiencing an instability (Cameron, 1978). The collapse results in high-density regions that collapse even further. As the regions collapse, they draw in surrounding gas and dust to increase in mass and create gravitationally-bound protoplanets (Boss, 2001). In order for the disk to collapse, an instability must have formed. Jeans (1929) formula is used to describe the collapse of an uniform density disk, assuming an uniform speed of sound. Jeans examined the likelihood of a disk collapsing. He found that if a density fluctuation is present in a disk, it is unstable to gravitational collapse if:

$$\lambda > \frac{\pi c_s^2}{G\rho} \qquad 1.1$$

where c_s is the speed of sound, λ is the wavelength of the instability, G is the gravitational constant, and ρ is the density. This criteria was later improved on by the creation of the Toomre Q equation, which gauges the stability of a non-axisymmetric perturbation in a flat disk. The Toomre Q is given by:

$$Q = \frac{c_s \kappa}{G \pi \sigma} \qquad 1.2$$

where σ is the surface density and κ is the epicycle frequency (Bodenheimer, 2006). A disk is considered stable if Q is greater than 1.5. This theory assumes that regions of instability will arise in a disk and that the regions will be long-lived enough to grow. The disk will begin to fragment as regions of greater density form, resulting in disk instability. The high density regions will draw in more material and eventually collapse into a planet.

The main advantage of this model over the core accretion model is the time scale requirement. This model can form giant planets on extremely quick time scales, on the order of 10^3 years (Mayer *et al.*, 2004) to about 10^5 years (Bodenheimer, 2006). Both of these time scales are shorter than the expected lifetime of the circumstellar disk, thus allowing plenty of time for the planets to form. The Spitzer Space Telescope shows indirect evidence of the formation of a gas giant around CoKu Tau/4, a star around 1 million years old (Forrest *et al.*, 2004). This, therefore, shows that planets may be able to form in less than 1 million years. The planet's presence supports the gas instability model, as the core accretion model suggests there are no planets accompanying young stars.

Another argument in support of the gravitational instability model is the current core sizes of the gas giants. As previously mentioned, the core of Jupiter is thought to currently be 3 Earth masses (Saumon and Guillot, 2004) and may have undergone erosion (Saumon and Guillot, 2004; Guillot, 2005). Saturn's core, on the other hand, may be larger than Jupiter's core (Guillot, 1999a; Saumon and Guillot, 2004). This would conflict with core accretion as Jupiter is thought to have formed early and closer to the Sun when more material was available. Gravitational instability has no constraints on

core size as they are formed during the initial collapse of the planet. A larger core simply means that Saturn started with more mass (Boss, 2002).

There are a few major problems with the gravitation instability model. The presence of chondrules in meteorites is difficult to explain without dust accumulation. Another problem that arises is revealed by the Toomre Q factor. The Toomre Q factor is used to describe the disk stability. For planetary formation, Q needs to be less than 1.4, which requires the gas to be near isothermal. This may be possible if local isothermal behaviors existed in the disk (Boss, 2001; Mayer *et al.*, 2004). The work of Cai *et al.* (2006) shows that in their simulations they do not require the disk to be isothermal. The difference in the results may be due to different techniques and assumptions. Figure 1.1 summarizes the theories of the Solar System formation.

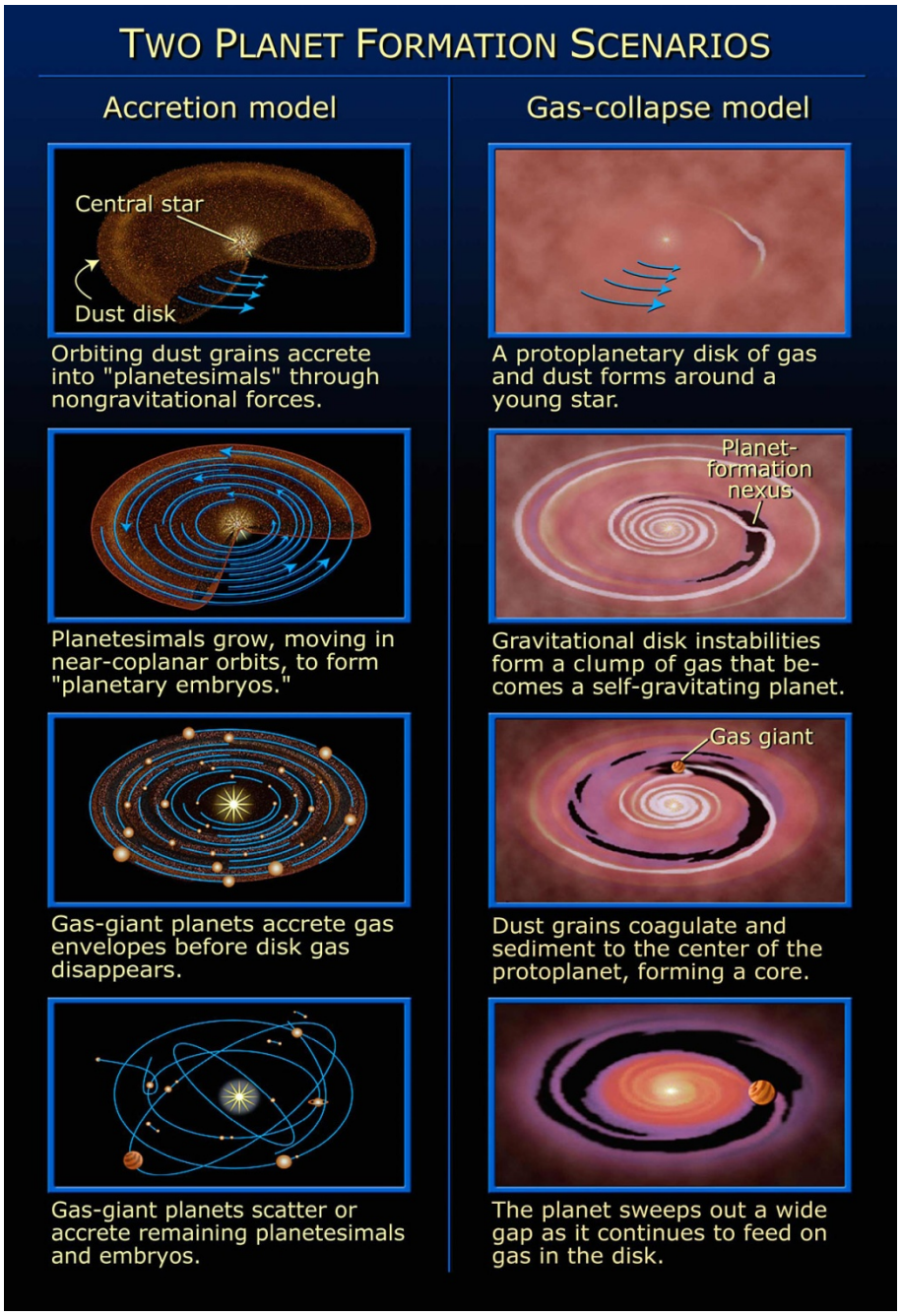

Figure 1.1 A summary of both the core accretion model and the gravitational instability model. Source: NASA/ESA and A Feild (STScI). The core accretion model is generally more favored of the two models.

1.3.3 Clathrate

Clathrates have been invoked to explain the enrichment of heavy elements. Clathrate hydrates are water-ice compounds that form an open lattice structure of ice in the shape of cages. Molecules inside the cages stabilize them, and these cages transport volatiles to areas where they would not be stable or present on their own. The first proposed clathrates in our Solar System were in cometary nuclei (Delsemme and Swings, 1952). Miller (1961) examined the presence of clathrates by using the van der Waals and Platteeuw model along with his own experiments to determine the likelihood of clathrates existing in a wide variety of objects: envelopes of the outer planets, Saturn's rings, satellite interiors, terrestrial planet atmospheres, Mars' polar caps, and comets. If these cages existed during Solar System formation, then they might be the source of volatiles in the giant planets, but they would also require that water be highly enriched over the solar value. Gautier *et al.* (2001) modeled the enrichment that would result from clathrates. After their model calculation, argon, carbon, krypton, nitrogen, and xenon's enrichments were found to be within the error bars of the Galileo measurement. Sulfur, however was found to be higher than the observed value. To determine the accuracy of this model, a better measurement of water is needed. Gautier *et al.* (2001) requires water to be enriched to at least 8 × solar in the deep gaseous envelope of Jupiter. The Juno spacecraft will arrive at Jupiter in 2016, with the goal of measuring and mapping Jupiter's deep water and will hopefully be able to determine if clathrates were possible in the early Solar System.

1.3.4 Formation Theories and Uranus

The amount of ammonia and helium in the atmosphere of Uranus may explain the formation of Urauns. The amount of helium relative to hydrogen in the initial protoatmosphere should mirror that of the solar nebula (Pollack and Bodenheim, 1989) as the physical conditions in the region of formation would have inhibited the condensation and fractionation of helium. If the ratio does not mirror the solar nebula, than hydrogen may be being used create molecules inside the planet.

The atmosphere's composition is dependent on the composition of the grains imbedded in the solar nebula. Fegley and Prinn (1986) and Prinn and Fegley (1989) modeled the condensates that could have accreted to form Uranus. If complete thermochemical equilibrium is assumed, ammonia and methane formed prior to arriving at Uranus, and no hydrogen was needed to create ammonia and methane in the planet. However, if Uranus formed in a reservoir of carbon monoxide, carbon dioxide, molecular nitrogen ices, and clathrates, the hydrogen present in the initial atmosphere would have been used to produce methane and ammonia. This would have resulted in the helium to hydrogen ratio increasing inside the planet. This could increase the relative helium abundance in the atmosphere by 30% (Prinn and Fegley, 1989). The helium to hydrogen ratio would depend on the exact enrichment of carbon and nitrogen (Fegley and Prinn, 1986). Knowing the helium to hydrogen ratio provides information about the composition of the solar nebula, and in what form the volatiles arrived at the planet.

The microwave spectrum of Uranus indicates that ammonia is depleted in the upper troposphere relative to solar abundances (Gulkis *et al.*, 1978). It has been hypothesized that there is a sink for ammonia in a deep cloud, such as an ammonia hydrogen sulfide cloud or an aqueous solution with water. However, Lewis and Prinn

(1980) proposed different solution, namely, that nitrogen is depleted in the bulk of the planet. Instead of nitrogen and carbon taking the form of ammonia and methane in the solar nebula, they were instead in the form of molecular nitrogen and carbon monoxide. This would result in Uranus not accreting as much nitrogen in the molecular form, as molecular nitrogen would have been found mainly in the inner part of the nebula. Another possible explanation for the depletion of nitrogen is given in Chapter 4. Therefore, the amount of ammonia found at Uranus can be very telling about the initial conditions in the solar nebula.

Computer simulations attempt to replicate the interiors of the ice giants. In core accretion theory, the first process that occurs is the settling of grains towards the mid-plane of the nebula. The grains continue to grow through accretion until the protoplanetary core reaches a mass of approximately 10^{26} g, at which point it interacts with the surrounding nebula (Podolak *et al.*, 1991b). The nebular gas is under the influence of the protoplanetary core, and becomes the protoplanetary atmosphere. This atmosphere grows by accretion, and will grow rapidly once the core reaches a mass of 15 Earth masses (Bodenheimer and Pollack, 1986). Another estimate of the critical core mass suggests a similar formation scenario, but in this case the grains that form in the solar nebula in the mid-plane are enriched with water. This results in the atmosphere having a higher mean molecular mass due to the additional water. Most of the material is bound in larger bodies, which leaves very little gas (Stevenson, 1984). The critical core in this case can be as low as 0.05 to 0.1 Earth masses, much smaller than the 15 Earth masses predicted by Bodenheimer and Pollack. Regardless of the critical size of the core, accretion formation theory suggests a core made up of low volatility rock surrounded by an envelope of more volatile material: an ice and solar mixture of hydrogen and helium.

This will form distinct layering in the interior, as the density of the rocks is much different than the volatile slushy icy layer. More measurements of the interior are needed to support this theory.

1.4 Observations

Modeling the clouds in the atmospheres of the ice giants is achieved by knowing both the pressure and temperature at a specific level, as well as, the composition. With this information, and the use of the hydrostatic and thermodynamic equilibrium, it is possible to calculate the lapse rate of the atmosphere, and to calculate the location and densities of the clouds. The only spacecraft mission to have visited Uranus and Neptune was Voyager 2. Earth-based observations from the ground and the International Ultraviolet Explorer (IUE) provided information on the temperature-pressure structure and the composition of the planet's upper troposphere. It should be noted that the Voyager 2 spacecraft was optimized for measurement at the gas giants and not the ice giants; therefore, the data received was not optimal. However, Voyager 2 was able to make reasonable measurements in the ultraviolet spectrum because there was enough sensitivity overlap with Jupiter's sensitivity. For the infrared spectrum, the peak sensitivity for Jupiter varied from that of Uranus and Neptune, resulting in Voyager 2 having low sensitivity in the infrared spectrum at these planets. Data on Uranus and Neptune have since been obtained using occultations and ground-based telescopes (Lindal *et al.*, 1987; Smith *et al.*, 1989; Klein and Hofstadter, 2006).

1.4.1 Occultation

Occultation is a technique used to observe the atmospheres and ionospheres of celestial bodies. For our study, occultations are used to obtain the temperature and pressure profiles in the giant planets as will be seen in section 1.4.3. When occultations are performed, a source of light must be strategically placed so that it passes through the atmosphere of a body. How the light bends as it passes through provides information about the temperature and composition of the atmosphere. The source of light can vary, from a spacecraft, to the Sun, or to a distant star. The wavelength that the light source emits determines what is learned about the body and what region of the atmosphere is being observed. A variety of wavelengths are desirable to learn about different aspects of the body's atmosphere.

Ultraviolet occultations measure the attenuated intensity. The extinction of light in ultraviolet occultations is due to the absorption and scattering of various gases in the atmosphere and are used to see the temperature and pressure profile above the homopause. Visible occultations are ideal for monitoring the turbulence and thermal structures of a planet's atmosphere. These occultations have the distinct advantage of being possible from the surface of Earth and are used to examine the stratosphere. Lastly, there are radio occultations typically preformed using spacecraft orbiting or passing by a planet. These occultations are unique due to proximity of the source, the planet, and the resulting large bending angles, which allow for the collection of data from deeper in the atmosphere, the lower stratosphere to the 1 bar level.

1.4.2 Radio Science

Planets, stars, and other celestial bodies naturally emit radio waves. To study these emissions, a radio telescope can be used. The Earth's atmosphere can interfere with ground-based observations. For example, the Earth's ionosphere distorts the incoming signals for wavelengths longer than 20 cm, and when the wavelengths are longer than 10 m the atmosphere becomes opaque to incoming signals. Radio telescopes have two major components: a radio antenna to collect energy and a receiver to detect it. The area and the efficiency of the antenna, along with the sensitivity of the receiver, determine the ability of the telescope to measure weak sources of radio emissions.

The first radio antenna used to study astronomical radio sources was built in 1932 by Karl Jansky. Jansky, an engineer at Bell Telephone Laboratories, designed the telescope to receive radio signals at the frequency of 20.5 MHz, or a wavelength of approximately 14.6 m. The antenna was 30 m in diameter and rotatable. After several months of observations, Jansky categorized three types of statics: nearby thunderstorms, far-off thunderstorms, and a faint, steady hiss of unknown origin. The steady hiss would repeat in a cycle of 23 hours and 56 minutes. This is the length of an astronomical sidereal day, which is the time it takes any "fixed" object in the sky to return to the same position in the sky. Jansky hypothesized that the static was from the Milky Way Galaxy, and he started the field of radio astronomy. During World War II, there was a rapid development of radar technology. When the war ended, this technology quickly and easily translated into the field of radio astronomy.

Due to the wide range of frequencies of the radio spectrum, the antennas used varied. The world's largest filled-aperture telescope is the Arecibo radio telescope located in Puerto Rico, which was originally constructed in 1963. Arecibo's dish is 305 m in

diameter and it observes frequencies between 47 MHz to 10 GHz. In 1946, a new technique was developed for radio telescopes called astronomical interferometery (Mccready *et al.*, 1947). This technique requires an array of dishes. Using interferometery increases the amount of energy collected, and allows higher spatial resolution. Interferometery superposes the signal waves from two different telescopes. When the two waves have the same phase they add to each other and when they have the opposite phase they cancel each other out. Multiple antennas are ideal, as it increases the quality of the image. One interferometer radio telescope is the Very Large Array (VLA) in Socorro, New Mexico. There are 27 antennas in the array. Each antenna's disk is 25 m in diameter. The VLA is used to research a plethora of astronomical topics, including radio galaxies, quasars, supernova, the Sun, planets, and black holes. The advantage of radio wavelength is that they probe deeper in the atmospheres than shorter wavelengths. The VLA and interferometery will be discussed further in Chapter 3.

Figure 1.2 Image of the VLA Radio telescope courtesy of NRAO/AUI. The VLA is located in Soccoro, New Mexico and consists of 27 different antennas. Data from the VLA/SMA are used in Chapter 3 to calculate elemental abundances.

1.4.3 Thermal Structure

Before Voyager 2, data on the thermal structure of the ice giants was derived from stellar occultation in the visible spectrum (Dunham *et al.*, 1980; French *et al.*, 1983), and observations in the infrared spectrum (Orton *et al.*, 1983; Tokunaga *et al.*, 1983). Stellar occultations are responsible for nearly all of our information about the .1 to 10 μ-bar region of the atmosphere of Uranus, as it determines the thermal structure more accurately than using infrared data. Uranus is dim, 1.7 to 2.5 μm, due to the strong methane absorption; therefore, the stellar flux used does not need to be bright. The

infrared spectrum probes the 100 mbar region of the atmosphere, and finds a minimum temperature of approximately 50 K in Uranus' atmosphere (Orton *et al.*, 1983).

A variety of experiments have been performed using Voyager 2's Infrared Interferometer Spectrometer instrument (IRIS), radio occultation experiments, and stellar occultations to provide the thermal profile of Uranus. Ground-based measurements of microwave/infrared radiometry and the Ultraviolet Spectrometer, UVS, are also used. The UVS observations made by Voyager 2 measured the opacity of the atmosphere as a function of altitude and wavelength. The UVS measured the radiation in the wavelengths of 0.04 to 0.16 micrometers. Spectral absorption was used to identify absorbers and estimate the atmospheric thermal structure, the number density, and vertical mixing profiles. Using measured opacities, Herbert *et al.* (1987) was able to deduce the altitude profiles of molecular and atomic hydrogen, which derived the thermal profile for the pressure range of 10^{-6} to 500 μbar. Radio occultations were performed by tracking Voyager 2 with two unmodulated radio carrier frequencies transmitted from the spacecraft's microwave dish at 13 cm and 3.6 cm (Eshleman *et al.*, 1977; Edelson *et al.*, 1979). These signals passed through the equatorial atmosphere of the planet and the signal perturbation provided new information about the thermal structure and composition of the atmosphere of Uranus (Tyler *et al.*, 1986; Lindal *et al.*, 1987). The occultation provided information in the latitude range from 2° to 7° S. Figure 1.4 shows the atmospheric profile obtained from the ingress and egress occultation (Lindal *et al.*, 1987). The profiles were computed using the refractivity data for hydrogen and helium and assumed a hydrogen abundance of 85% and a helium abundance of 15%. This ratio was derived by comparing the radio occultation data to the IRIS data (Hanel *et al.*, 1986; Tyler *et al.*, 1986; Conrath *et al.*, 1987a; Lindal *et al.*, 1987). IRIS obtained vertical

temperature profiles for Uranus through an inversion of the spatially resolved spectra. Due to a limited signal-to-noise ratio, the complete temperature profile retrieval could only be computed by averaging the spectra. Profiles were derived in the north and south polar regions using this method, and resulted in temperatures between 60 and 900 mbar. The temperature was found to vary between 52 K and 80 K with an average temperature of approximately 60 K (Hanel *et al.*, 1986). The IRIS and radio occultations data are found in agreement, which is not surprising as they are both used to calculate the He abundance.

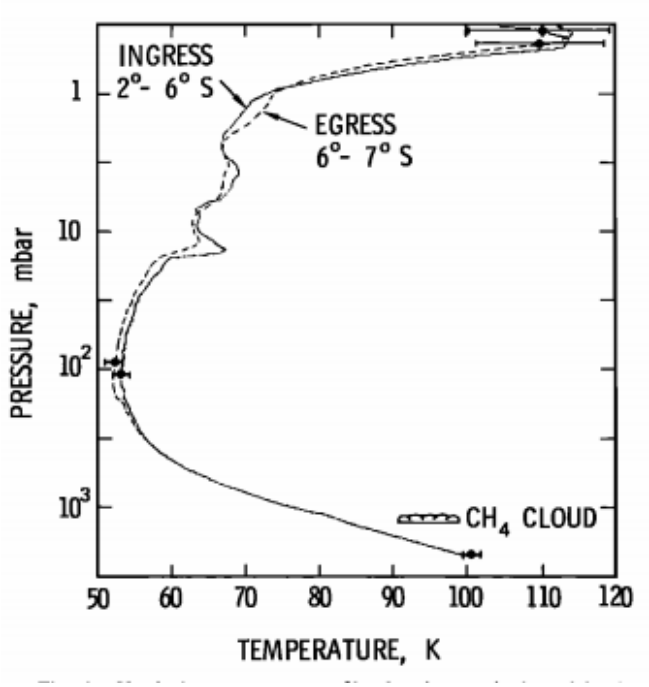

Figure 1.3 Temperature profiles of Uranus derived from Voyager 2 radio occultation by Lindal *et al.* (1987). The radio occultation was only able to reach the top of the troposphere. UV, Visible, and IR occultation do not probe as deep in the atmosphere.

The only in situ measurements of a giant planet were taken by the Galileo probe. The Galileo probe was able to obtain a temperature and pressure profile in the atmosphere. The atmosphere followed a dry adiabat between 0.41 and 24 bars (Seiff, 1996). The Voyager upper atmosphere measurements of temperatures greater than 1000 K at 0.01 microbar levels were confirmed as well.

1.4.4 Composition

1.4.4.1 Methane

Information on the composition of Uranus' atmosphere, in the pre-Voyager era, was derived from the analysis of ground-based observations of the infrared and ultraviolet spectrum. In the infrared, both Uranus and Neptune displayed an absence of an emission feature of methane, and ethane (Gillett and Rieke, 1977; Macy and Sinton, 1977; Orton *et al.*, 1983). Only the upper limit on the abundances could be defined. Orton *et al. (1983)* limited the methane mass mixing ratio, the abundance of specie relative to the atmosphere, to 3×10^{-5}, which was the value expected from cold-trapping at low temperatures. This value is lower than any other giant planet. The upper limit of ethane's mixing ratio was 3×10^{-8}. The abundance of helium was estimated by Orton (1986) using the infrared spectrum. Orton proposed a 40% mixing ratio for helium, which was a flawed conclusion since it ignored the effects of a stratospheric aerosol layer. After Voyager 2, the actual value was found to be only 15% (Conrath *et al.*, 1987a).

During the Voyager 2 fly-by, observations were executed using infrared and ultraviolet spectrometers. The UVS detected hydrocarbon concentrations that were lower

at comparable pressure levels to those found at Jupiter and Saturn (Baines *et al.*, 2002). Herbert *et al.* (1987) established a methane mass mixing ratio upper limit of about 10^{-7} in the 100 to 1 μbar region. The Infrared Space Observatory, ISO, conducted observations between 1995 and 1998 of the giant planets, and confirmed some of the Voyager 2 data. ISO detected several new species, including water vapor, in all four giant planets, carbon dioxide on Jupiter, Saturn, and Neptune, benzene on Jupiter and Saturn, and diacetylene on Saturn (deGraauw *et al.*, 1997; Feuchtgruber *et al.*, 1997; Lellouch *et al.*; Coustenis *et al.*, 1998; Lellouch *et al.*, 1998; Feuchtgruber *et al.*; Moses *et al.*, 2000; Lellouch *et al.*, 2002). Spectroscopic measurements and the Voyager 2 radio occultation experiment showed a mixing ratio of $CH_4/H_2 = 2\%$ in the troposphere, which is a 30 × enrichment over solar (Baines, 1982; Lindal *et al.*, 1987). Ground-based observation in the infrared, submm, mm, and radio wavelengths have resulted in complementary data, along with useful data on ammonia, H_3^+, and other disequilibrium species.

1.4.4.2 Ammonia

The microwave spectrum of Uranus indicates there is a sub solar abundance of ammonia in the troposphere (Gulkis *et al.*, 1978). A few theories attempt to explain this depletion. Ammonia may be tied up in a deeper cloud, either an ammonia hydrogen sulfide cloud or an aqueous solution with water (Prinn and Lewis, 1973; Weidenschilling and Lewis, 1973). Klein and Hofstadter (2006) found that over approximately 30 years the brightness temperature changed by 30 K at wavelengths near 3.5 cm, which cannot be due to geometric effects alone, and may be due to changes in the abundances of

ammonia. The authors hypothesize that there may be some temporal variations existing deep in the Uranian troposphere. The emissions observed are controlled by the temperature and composition. The changes in brightness appear to be seasonal. As Uranus approached equinox in 1989-1994, there was an increase in brightness temperature differences between the pole and equator (Hofstadter and Butler, 2003). Hofstadter and Muhleman (1989) suggested the meridianal variations in radio brightness were due to variations in the ammonia mixing ratio with latitude. Ammonia is thought to be depleted in the region of the atmosphere probed by observations at a wavelength of 2 cm (Hofstadter and Muhleman, 1989).

Hofstadter and Butler *(2003)* found that the upper atmosphere of Uranus is depleted in ammonia and other absorbers relative to solar. Deeper in the atmosphere, they found the abundances were more consistent with solar. At approximately 10 bar, the mixing ratio of ammonia was 9.0×10^{-7}, while near 50 bar the mixing ratio was 1.0×10^{-5}. The VLA observed meridianal changes in ammonia, hydrogen sulfide, and water. De Paters *et al. (1991)* also used the VLA observations and found depleted ammonia.

1.4.4.3 Gas Giants Composition

The first situ measurements of the composition of a giant planet were carried out by the Galileo Probe Mass Spectrometer (GPMS) at Jupiter in 1995 (Niemann *et al.*, 1998a; Atreya *et al.*, 2003; Young, 2003). The probe sampled the atmosphere with a quadrupole mass spectrometer in the 0.5 to 21 bar region of the atmosphere. Niemann *et al. (1998)* found that the helium and hydrogen mixing ratio were close to the solar values. The abundances of carbon, oxygen, argon, neon, and sulfur were also measured.

Krypton, xenon, carbon, and sulfur were observed and were found to be enriched when compared to solar. Neon and oxygen were found to be subsolar. It should be noted, however, that the Galileo probe entered Jupiter in an infrared 'hot spot,' which is a downwelling region in the troposphere where water, hence oxygen, was found to be depleted. The Juno mission, which launched in 2011, will attempt to obtain a global measurement of oxygen using its microwave radiometer to image deeper into Jupiter's atmosphere, and will further our knowledge of the amount of oxygen actually present on Jupiter. The measurements for carbon, nitrogen, and sulfur have since been updated (Wong *et al.*, 2004b), and the protosolar elemental abundance found can be seen in Table 1.2. Phosphorus's elemental abundance was further updated by Cassini CIRS measurements, which found a phosphorus abundance of 4.8 × solar. The values in Table 1.2 are used throughout this work and are referred to as 'solar' throughout this work.

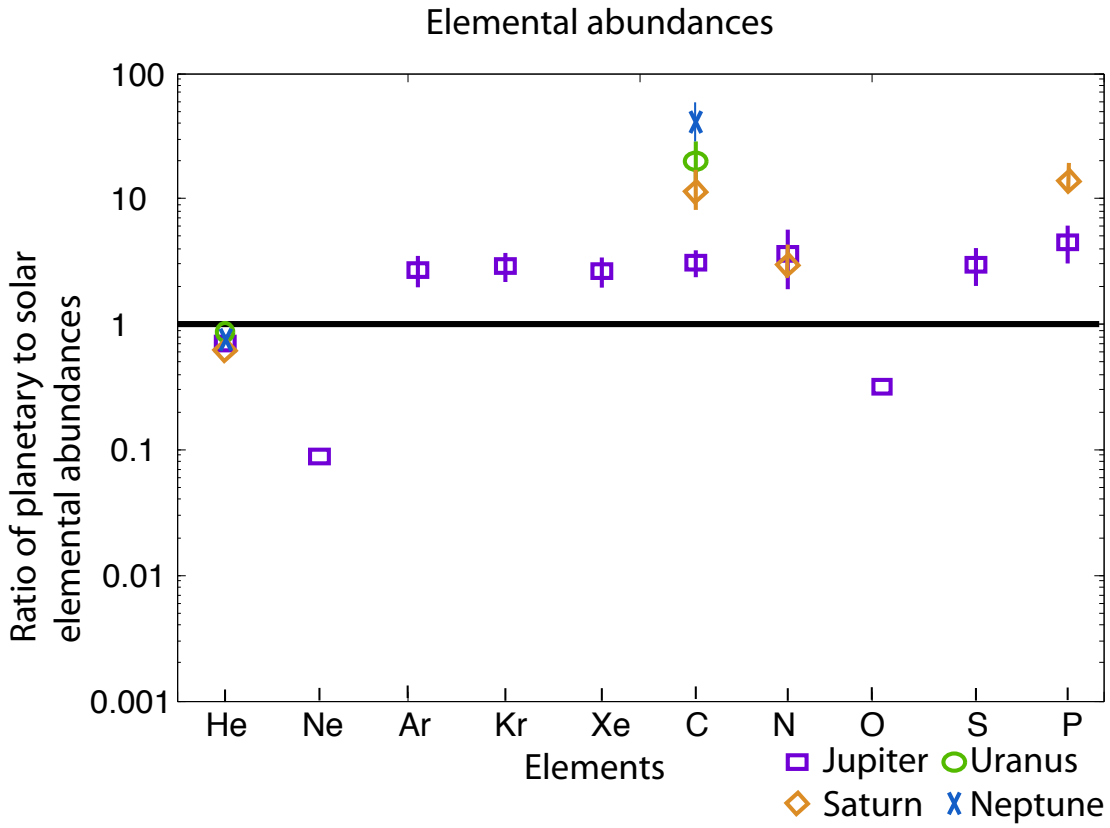

Figure 1.4 The ratio of planetary to solar elemental abundances found by measurements and inferred for the ice giants for species other than carbon. The carbon measurements at Uranus and Neptune are from Voyager 2 observations. The details of the measurements are shown in Table 1.2.

Fewer measurements are available for Saturn. The helium elemental abundance has been constrained by a reanalysis of Voyager 2 data to be between 0.57-0.82 × solar (Conrath and Gautier, 2000). Carbon's elemental abundance was found to be 9.3 × solar, which is greater than Jupiter (Flasar *et al.*, 2005). Similarly, phosphorus's elemental abundance, 15.9 × solar, was found to be greater than it is on Jupiter (Fletcher *et al.*, 2009a). The increasing enrichment of elemental abundances in planets that are further away from the Sun is expected by Solar System formation models. The ice giants, therefore, should have even higher enrichments of condensables than the gas giants. If

the ice giants are not found to be as enriched in their atmospheres, then there are implications for the interior structure, which will be investigated in Chapter 4.

1.4.4.4 Summary

A summary of the protosolar elemental abundances of the giant planets is seen in Table 1.2. It should be noted that the values quoted represent enrichment factors over the most recent protosolar abundances (Asplund, 2009). Measurements of the original solar partitioning in the nebula are not possible, as the Sun has undergone fusion and thus its elemental abundances have slightly changed (Michaud *et al.*, 1983). The effects of diffusion at the bottom of the Sun's convective zone can now be accounted for and indicate the chemical composition in the reservoir. Turcotte (1998) accomplish this by including the effects of both radiative acceleration and gravitational settling. Turcotte and Wimmer-Schweingruber (2002) calculated the relative change in the surface abundance of helium and other abundant elements during their lifetime. They performed this calculation through a detailed solar model that included additional mixing just below the convective zone. Using present day values in the Sun, the protosolar metal, where metal is defined as anything other then hydrogen and helium, abundance relative to hydrogen can be calculated by increasing the values by 0.05 dex, where a $\mathrm{dex}(x) = 10^{x}$. The effect of diffusion on helium was found to be slightly higher, which resulted in an increase of 0.057 dex. When these constraints are applied to current photospheric values, we are able to obtain the protosolar elemental abundances seen in Table 1.2.

Table 1.2 Elemental abundances in the giant planets as inferred from measurements, and using Asplund *et al* (2009) protosolar values.

Current protosolar elemental abundances from Asplund et al. 2009, with elemental enrichment factors at Jupiter and Saturn (Atreya 2010)

Elements	Asplund 2009	Jupiter/ Sun	Saturn/ Sun	Uranus/ Sun	Neptune/ Sun
He/H	0.09705 ±0.02	0.808 ± 0.019	0.70 ± 0.13[c]	0.92-1.0	0.92-1.0
Ne/H[b]	$9.55 \times 10^{-5} \pm 0.11$	0.130 ± 0.013		20-30 (?)	30-50 (?)
Ar/H[c]	$2.82 \times 10^{-6} \pm 0.14$	3.23 ± 0.64		20-30 (?)	30-50 (?)
Kr/H	$2.00 \times 10^{-9} \pm 0.07$	2.33 ± 0.43		20-30 (?)	30-50 (?)
Xe/H	$1.95 \times 10^{-10} \pm 0.07$	2.28 ± 0.44		20-30 (?)	30-50 (?)
C/H	$3.02 \times 10^{-4} \pm 0.06$	3.92 ± 0.94[h]	8.4 ± 1.65[f]	20-30 (?)	30-50 (?)
N/H	$7.59 \times 10^{-5} \pm 0.06$	4.38 ± 1.67[h]	4-6 (?)	20-30 (?)	30-50 (?)
O/H	$5.50 \times 10^{-4} \pm 0.06$	0.45± 0.15[dh]		20-30 (?)	30-50 (?)
S/H	$1.48 \times 10^{-5} \pm 0.04$	3.01 ± 0.71[h]		20-30 (?)	30-50 (?)
P/H	$2.88 \times 10^{-7} \pm 0.04$	3.75 ± 0.21[g]	12.7 ± 0.83[g]	20-30 (?)	30-50 (?)

[a.] The protosolar elemental abundances are calculated from the present-day solar photospheric value of Asplund et al. (2009), after taking into account the effect of diffusion at the bottom of the convective zone on the chemical composition of the photosphere, and the effects of gravitational settling and radiative acceleration.
[b.] Grevesse et al. (2005) derived neon using oxygen as a proxy. Using Chandra X-ray spectra Drake and Testa (2005) suggest a Ne/O = 0.4. However, solar wind and solar energetic particles match the lower Ne/O = 0.15, therefore that value is used here.
[c.] Argon also uses oxygen as a proxy and Ar/O = 0.0033
[d.] Hot spot data for oxygen at Jupiter.
[e.] Based on reanalysis of Voyager data by Conrath & Gautier (2000).
[f.] Cassini/CIRS measurments (Flaser et al. 2005).
[g.] Cassini/CIRS measurments (Fletcher et al. 2009).
[h.]. Wong 2004 values

Asplund, M., N. Grevesse, A. J. Sauval, and P. Scott (2009), The chemical composition of the sun, Annual Review of Astronomy and Astrophysics, Vol 47, 47, 481-522.
Conrath, B. J., and D. Gautier (2000), Saturn helium abundance: A reanalysis of voyager measurements, Icarus, 144(1), 124-134.
Drake, J. J., and P. Testa (2005), The 'solar model problem' solved by the abundance of neon in nearby stars, Nature, 436(7050), 525-528.
Flasar, F. M., et al. (2005), Temperatures, winds, and composition in the saturnian system, Science, 307(5713), 1247-1251.
Fletcher, L.N., et al. (2009), Phosphine on Jupiter and Saturn from Cassini/CIRS, Icarus, 202, 543-564.
Wong, M. H., et al. (2004), Updated Galileo Probe mass spectrometer measurements of carbon, oxygen, nitrogen, and sulfur on Jupiter, Icarus, 171, 153-170.

1.5 Condensable

Unlike Earth's tropospheric clouds, the giant planets' clouds consist of more constituents than water. For the clouds of Jupiter and Saturn, the condensable volatiles are ammonia, hydrogen sulfide, and water vapor. Ammonia condenses into an ammonia ice cloud, hydrogen sulfide reacts with ammonia to form an ammonium hydrosulfide or an ammonium sulfide cloud (Weidenschilling and Lewis, 1973), and water condenses to

form water ice/liquid or an aqueous ammonia solution. The water cloud is expected to form the deepest and be the most substantial cloud, assuming solar enrichment of all species. The ammonia hydrosulfide and ammonia-ice will form above the water cloud, as seen in Figure 1.5 at Jupiter for a 4 × solar case. The base of the clouds is determined by calculating the lifting condensation level, LCL. By comparing the partial pressure and the saturation vapor pressure of the condensable volatile when the relative humidity reaches 100%, the LCL is reached as well as the cloud base. This calculation is performed in the ECCM, and a more detailed description can be found in Chapter 2 and appendix A.

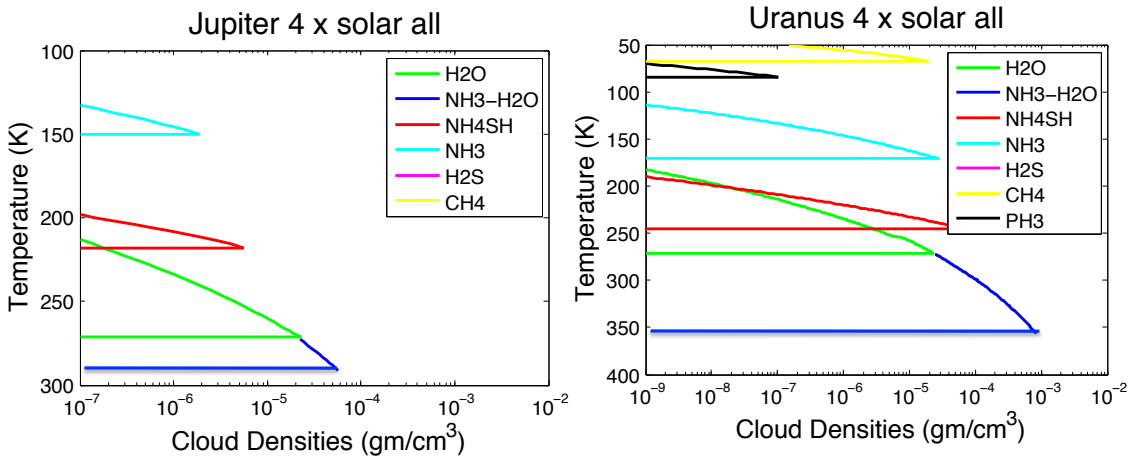

Figure 1.5 Jupiter and Uranus cloud densities in g cm^{-3}. All elemental abundances were 4 × solar. This case shows a representative case of the cloud present in the Jupiter and Uranus's atmosphere. These cloud represent an upper limit on cloud densities as precipitation is not included in the calculation. Uranus has the addition of the methane and phosphine cloud which are not seen on Jupiter.

As for the ice giants, all previously mention clouds can be present, along with some new ones. The methane cloud is the upper most cloud and is seen in the one-bar

region of the atmosphere. The location and presence of the rest of the cloud structure is more malleable. Without proper measurements of the concentrations of the other species in the atmosphere, it is hard to determine the proper cloud structure. If nitrogen, sulfur, oxygen, and phosphorus are all enhanced similar to carbon, 20 to 30 × solar for Uranus and 30 to 50 × solar for Neptune, these clouds will form similar to their counter-clouds on Jupiter and Saturn. However, the atmospheres of the ice giants are colder than the gas giants, thus clouds such as methane, and phosphine must be considered. Uranus' clouds can be seen in Figure 1.5 for 4 × solar of all species. This structure will be examined more extensively in Chapter 3 with the use of VLA data.

Chapter 2 : CLOUDS AND PRECIPITATION

The Equilibrium Cloud Condensation Model, or ECCM, is a thermochemical equilibrium model used to predict a multi-layer cloud structure on the giant planets (Lewis, 1969; Weidenschilling and Lewis, 1973; Atreya and Romani, 1985). The model calculates upper limits for the cloud concentrations, which are expected to be reduced by one to several orders of magnitude when precipitation is allowed (Rossow, 1978; Lunine and Hunten, 1987; Atreya *et al.*, 1999). In this chapter, we show the effect of precipitation on the concentration of water clouds at Jupiter, following the formulations of cloud microphysics (Rossow, 1978; Carlson *et al.*, 1988; Ackerman and Marley, 2001). The goal of this work is to better quantify and understand the cloud processes on the giant planets. Clouds can interfere with ground based and spacecraft mission making it difficult to make measurement in the deep atmosphere. Therefore, the clouds need to be properly understood to improve mission designs. Furthermore, examining the deep interior of the giant planets is difficult even without clouds due to the harsh pressure environment. Clouds can also be useful as they are tracers of atmospheric motions. The cloud base location and the elemental abundance below the cloud bases can, however, be used in the development of Solar System formation theories.

2.1 Cloud Formation

Clouds are seen on almost every planet in our Solar System, and can cover the entire globe. In general, cloud formation on Earth starts with a parcel of air on the surface of Earth. As the sun warms the surface, the parcel will warm causing it to rise. While the parcel rises, it will expand and cool adiabatically, a reversible process in which no heat is exchanged with the surroundings. From here, two scenarios can happen based on the state of the environment. If the environment is stable, i.e. the surrounding air is warmer than the parcel, the parcel will eventually stop rising and sink back down to the surface or to the level from which it started. If the environment is unstable, i.e. the surrounding air is colder than the parcel, the parcel will continue rising and may form a cloud.

On Earth, clouds form convectively, orographically, or as the result of a frontal system/Hadley cell circulation. A convective cloud forms when parcels are warmed and ascend into the atmosphere. Once the parcel is chilled to the dew point, the temperature at which the parcel becomes saturated, a cloud forms. Another method for cloud formation is orographic lifting, where a parcel of air moves from low elevation to high elevation due to terrain, such as a mountain. As the parcel is lifted, it cools with altitude and can reach saturation. This method of cloud formation is more relevant on Earth than on the giant planets. The giant planets do not have a surface, thus there is no terrain for parcels to orographically lift over. For a cloud to form due to a frontal system, one large mass of air interacts with another large mass of air of a different temperature. The warm air mass can move over the colder mass or the colder air mass can move under the warm mass. If the warm air is on bottom, the warm air will rise and expand. As it

expands, it cools and if it cools enough the moisture in the air will condense forming a cloud.

Clouds that result from Hadley Cell-like circulation form similar to the clouds that result from a frontal system. Hadley Cell circulation is present at Earth and a similar circulation is seen on the giant planets. At Earth, warm air rises at the equator and around 60° N/S, and sinks at 30° N/S and the poles. This results in low pressure centers being created at the equator and 60° N/S. The warm air will rise and if the air becomes saturated a cloud will form. At 30° N/S and the poles, the cold air subsides and high pressure centers are produced. At Jupiter, many more cells are present resulting in more high and low pressure centers and the banded structure of the clouds. The mechanism for cloud creation on the giant planets is likely Hadley Cell-like circulation pattern. The ECCM assumes that the atmosphere is in equilibrium, and estimates the cloud base by using saturated vapor pressure and thermodynamics, which will be discussed in Section 2.2.

To form precipitation, the air needs to be saturated or super saturated. Saturation occurs when the cloud is cooled further or when more of the condensable is added to the system. The chance of precipitation occurring is affected by the amount of condensable in the atmospheres, as well as, how quickly the cloud is cooling. Furthermore, sufficient cloud condensation nuclei, CCN, need to be present to provide the vapor a surface to condense onto. For Earth, there are a variety of CCN both anthropogenic and natural, such as sea salts, dust, and soot. For the giant planets, it is less clear what the CCN are composed of. Cloud droplets will grow on the CCN and if the air is saturated enough they will eventually grow to a size where they are too heavy to

balance forces, such as gravity and friction, and will fall as precipitation. Not all droplets will fall to the surface. Some will evaporate as they fall through the atmosphere.

2.2 Cloud Model

The clouds of the giant planets have fascinated scientists since the discovery of the Great Red Spot. Jupiter's atmosphere has been studied in detail for half a century by remote sensing from the ground, earth orbit, spacecraft, —Pioneer 10 and 11, Voyager 1 and 2, Galileo, and Cassini—and *in situ* by the Galileo probe. Infrared spectroscopy has enabled the identification of the cloud ice particles composed of ammonia (Brooke *et al.*, 1998; Baines *et al.*, 2002; Wong *et al.*, 2004a), ammonium hydrosulfide (Sromovsky and Fry, 2010b; Sromovsky and Fry, 2010a) and water (Simon-Miller *et al.*, 2000). The Galileo probe performed the only *in situ* measurement of Jupiter's atmosphere, in December 1995. However, the probe entered a five-micron hot spot, an exceptionally dry atmospheric region (Orton *et al.*, 1998). This was evident from the near-absence of clouds (Ragent *et al.*, 1996) and the depletion of condensable volatiles (Niemann *et al.*, 1996). The Galileo probe carried a nephelometer that measured Jupiter's cloud properties, such as particle size distribution, and indicated a multilayered cloud structure (Ragent *et al.*, 1998). The clouds were found to have very low concentrations and were at much higher altitudes than predicted, consistent with the condensable volatile depletions recorded by the mass spectrometer.

On the other hand, the mass spectrometer on the Galileo probe determined the ratios of C/H (from CH_4), N/H (from NH_3), S/H (from H_2S), Ar/H, Xe/H, and Kr/H

and found them to be enriched relative to the solar values by a factor of 4 ± 2 (Niemann *et al.*, 1998a; Mahaffy *et al.*, 2000; Wong *et al.*, 2004b; Atreya, 2011) below the cloud base. The O/H ratio from water in this dry region was found to be 0.4 ± 0.1 × solar (Wong *et al.*, 2004b), when using the Grevesse *et al.* (2005) values for the protosolar abundances in the Sun. Using the current protosolar elemental abundance of Asplund *et al.* (2009), the O/H value is 0.45 ± 0.15. However, the O/H ratio in the deep, well-mixed atmospheric region of the probe entry site could not be determined (Niemann *et al.*, 1998a; Atreya *et al.*, 2003; Wong *et al.*, 2004b). Thus, the global water abundance remains uncertain. Lightning is one of several indirect methods to infer the presence of water. The Voyager spacecraft observed lightning at Jupiter (Cook *et al.*, 1979; Smith *et al.*, 1979; Borucki *et al.*, 1982). The Galileo (Little *et al.*, 1999; Gierasch *et al.*, 2000; Dyudina *et al.*, 2001) and Cassini (Dyudina *et al.*, 2004) spacecraft confirmed this observation. The presence of lightning possibly points to the existence of a water cloud, as the ammonia cloud has a low mass loading, and may not be able to generate the charge separation necessary for lightning (Levin *et al.*, 1983). The above sets of lightning observations are limited to a few localized regions where the tops of the thunderheads could be imaged. Thus, it is not possible to determine either the base or the concentration of the water cloud. Nevertheless, in the region of the thunderstorms, spectral analysis of the imaging data led to the conclusion that water abundance was at least solar, consistent with the Galileo NIMS spectral analysis over much larger regions (Roos-Serote *et al.*, 2004). The Juno spacecraft will arrive at Jupiter in 2016 and will measure and map Jupiter's deep water abundance using microwave radiometers.

The ECCM predicts a multilayered cloud structure consisting of one or more of the following clouds: aqueous ammonia solution, water ice, solid ammonium

hydrosulfide, ammonia ice, methane ice, hydrogen sulfide ice, and phosphine ice. The model was first developed by Weidenschilling and Lewis (1973), and has undergone further development as described in Atreya and Romani (1985) and Atreya (1986). The ECCM can be run for all the gas planets. At each planet, there is a different composition, and a different temperature-pressure structure that must be stipulated. The composition is taken from measurements. When measurements are lacking, assumptions are made based on what is known about the planet.

The ECCM requires temperature and pressure values above the clouds. This is a known value and should come from measurement, and it is used for model convergence by matching the model calculated temperature and pressure with measurements. The code also requires that the user specifies an initial deep pressure to start the calculation, and the temperature at this point is calculated using the hypsometric equation. This initial value needs to be located below the clouds. The dry adiabatic lapse rate is used until a cloud condenses and then the wet adiabatic lapse rate is used. The dry adiabatic lapse rate expresses the adiabatic cooling of a gas parcel due to expansion. The wet adiabatic lapse rate is simply the dry adiabatic lapse rate modified by the latent heat release of condensation. It is desirable to avoid the moist lapse rate in the first few steps of the model, which is why the calculation starts deep in the atmosphere. In the case of the giant planets, the moist lapse rate may or may not appropriately represent the lapse rate as will be discussed in section 2.3.

With the measured temperature and pressure values at one point above the clouds, and the user specified deep atmospheric pressure, the profile of the atmosphere can be calculated. For each condensable species, the saturation vapor pressure is calculated from a Clausius Clapeyron equation that was obtained in a laboratory. At

each level the pressure is calculated along with the partial pressure for each condensable species. The partial pressure of a species is defined as the pressure that a specie would have if it was the only constituent of the atmosphere. By comparing these two pressures, the cloud base can be found when these two values are equal, as this implies that the atmosphere is saturated. Figure 2.1 shows the sequence of model operations in the ECCM and Appendix A details the numerical method.

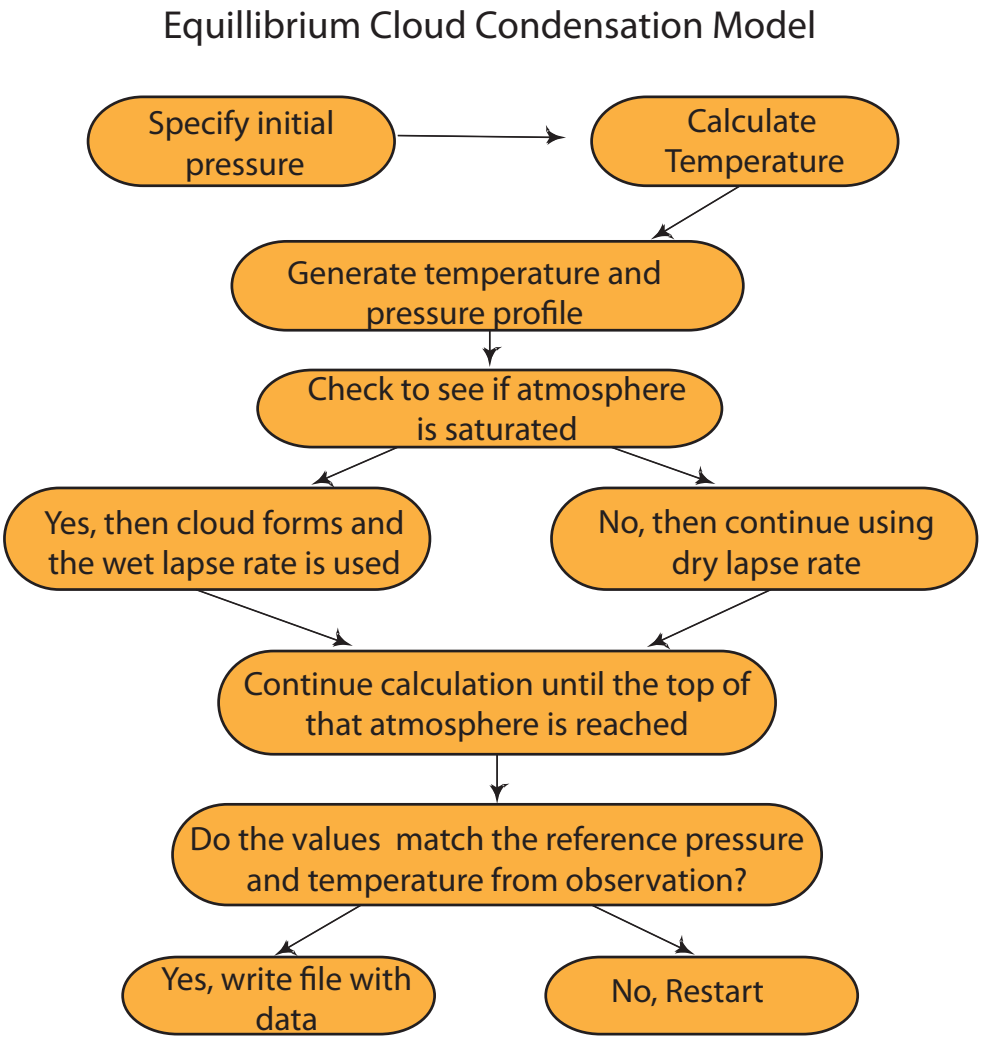

Figure 2.1 A flowchart of the numerical method in the ECCM. The numerical method is described in Appendix A.

2.3 Pressure effect: Van der Waals equation

The pressure in the interiors of the giant planets is high enough that it results in gases no longer behaving according to the ideal gas law. A new equation of state needs to

be derived that better represents the conditions in the giant planets. Consider a large closed container with only a few particles inside. The particles will move around but they will be too far apart to actually interact with each other. If the volume of the container is slowly decreased, the particles will get closer and closer to each other until they are close enough to have attraction or repulsion between them. This force is due to induced charge separation. When the pressure becomes high enough, the hydrogen atoms will repel each other. Collisions on the walls of the container will have an increased force and the real pressure will be greater than the pressure given by the ideal gas law. This is shown in Figure 2.4. The ideal gas law is modified using the Van der Waal equation:

$$P = \left[\frac{nRT}{(V - nb)}\right] - a\left(\frac{n}{V}\right)^2 \qquad 2.1$$

where V is the volume of the container, n is the number of moles, "a" is the measure of attraction between particles, and "b" is the volume per mole of particles. For hydrogen, a = 0.2453 bar L^2 mol^{-2} and b = .02661 L mol^{-1}.

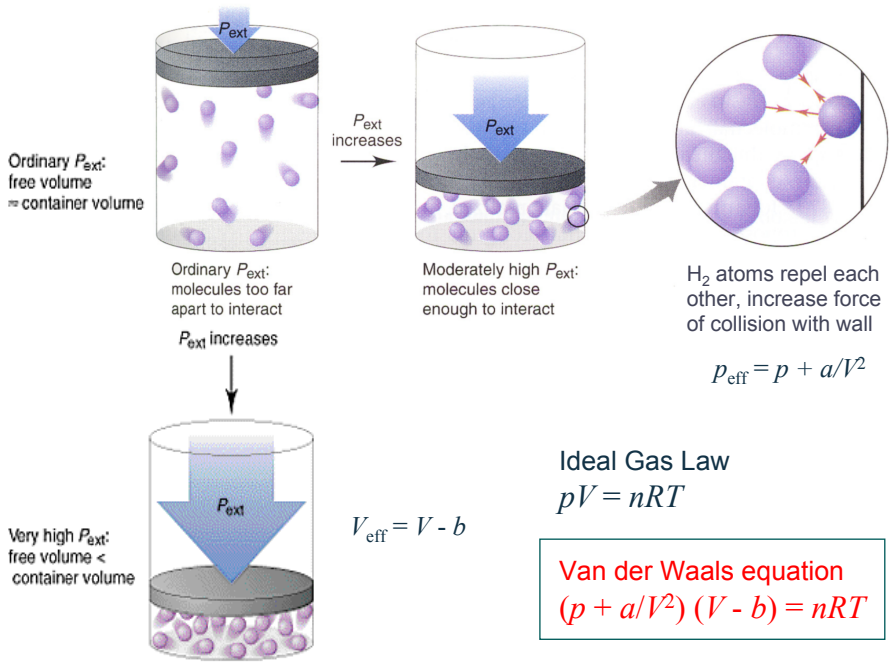

Figure 2.2 A flow chart explaining the processes of the Van der Waals pressure equation. Van der Waals equation is necessary in calculation of the cloud bases in the ice giants as the ideal gas law is no longer appropriate.

Figure 2.2 shows the effect of the Van der Waals equation. In the case of the clouds at Jupiter, this effect is not important as the cloud condense higher in the atmosphere where the ideal gas equation is still appropriate. On the ice giants, it effects are more important as the clouds, namely the liquid water/ammonia-water solution cloud, condense deeper. In Figure 2.3, the effects that the Van der Waals force has on hydrogen, helium, methane, and carbon dioxide is shown along with how they vary from the ideal gas equation at different pressures. Methane, helium, and carbon dioxide all result in the intermolecular attractions being predominate at lower pressure. At higher pressures, the molecule volume is affecting all of the species. Using the Van der Waal equation, where the ideal gas law predicts a pressure of 600 bar, the actual pressure is 860

bar. Similarly, 400 bar becomes 515 bar, and 200 bar becomes 226 bar. If water or ammonia is significantly enriched in the atmosphere, using the Van der Waals correction will significantly change where the cloud bases are located, and thus needs to be considered for our calculations.

The Van der Waals equation only accounts for the effects of hydrogen at high pressures, however other species may have an affect on the pressure. Karpowicz and Steffes (2011) have worked to develop a new equation of state for a H_2-He-H_2O-CH_4 mixture at pressures of 100 bar. This is the depth at which the NASA Juno microwave radiometer will be able to observe. They derived an equation based on published thermodynamic measurements and the pressure-volume-temperature measurements as well as using the mixture interactions between hydrogen and water (Lemmon and Jacobsen, 2004; Kunz *et al.*, 2006; Karpowicz and Steffes, 2011). Their equation is only stable to the 100 bar level, after that the quality of the fit for the temperature and pressure decrease. This will decrease the equation's accuracy, and make the equation invalid once the pressure exceeds 2500 bar. More work is needed to find the appropriate equation of state for the deep atmospheres of the giant planets. For the purpose of this work, the Van der Waals equation was used to account for the departure from the ideal gas equation.

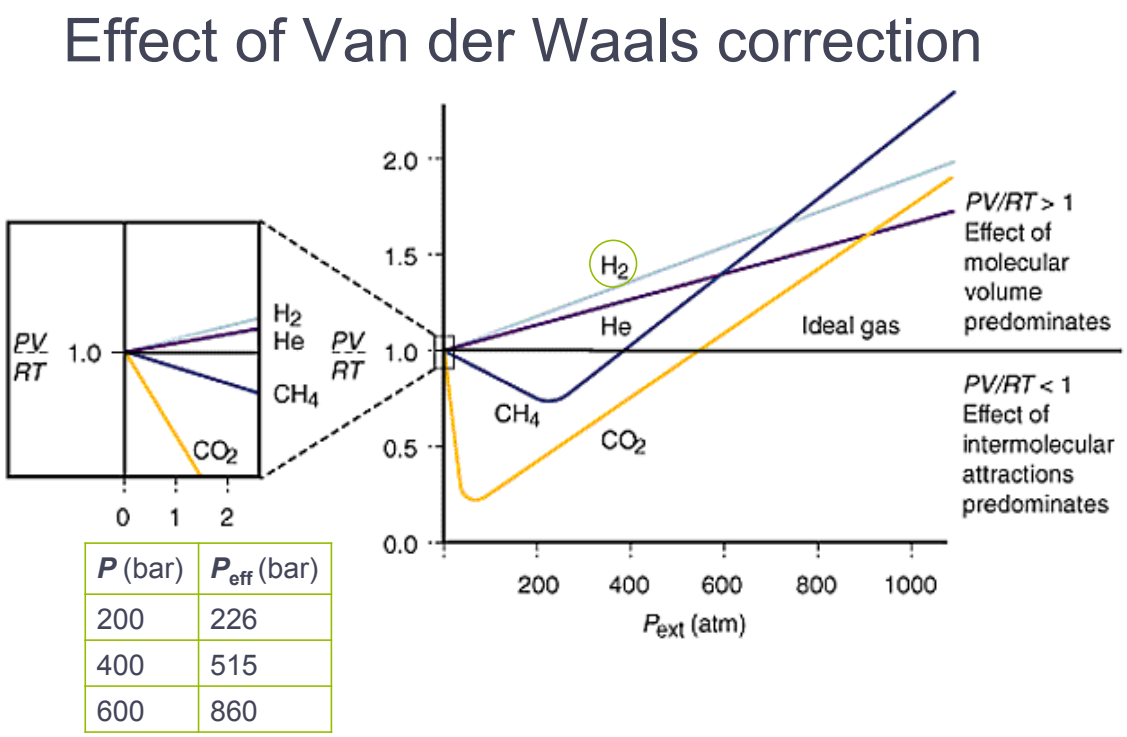

P (bar)	P_{eff} (bar)
200	226
400	515
600	860

Figure 2.3 A chart showing how the Van der Waals correction effects different species and the effect that Van der Waals has deep in the giant planets atmospheres. P is the pressure using ideal gas law, and P_{eff} is the pressure using the Van der Waals equation.

2.5 Cloud Microphysics

Cloud microphysics is a branch of cloud physics that concentrates on the scale from centimeters down to micrometers. It is primarily concerned with the processes surrounding droplet growth and their interactions with each other. The field of cloud microphysics is relatively new, with its official origins in the 1940's. Before that time, there were only a few studies performed, such as that by von Guericke in 1672 where he hypothesized that clouds were made up of water bubbles (Guericke, 1672). This theory

was supported until 1846 when Waller reported that fog particles do not burst on impact (Waller, 1847). It was not until the 18th century a naming scheme for clouds was created. Lamarck (1744-1829) realized that the forms of clouds that he was seeing were not by chance, and he created the first simple naming mechanism. During World War II, there was development of new observational techniques involving radar, and aircraft. After World War II, these techniques were used to collect data on the clouds and resulted in a surge of knowledge.

Clouds are full of particulate matter, which are extremely fine particles that may be solid or liquid. In Earth's atmosphere, the diameters of the particles ranges between 0.002 and 100 μm. The formation of particulate matter may occur by a number of mechanisms. In terrestrial atmospheres, they can be emitted directly into the atmosphere, such as ash from volcanoes or sea salt from the ocean. There is no surface on the giant planets, but particles can convect from the deep atmosphere to the cloud level to form particulate matter for clouds. These particles are referred to as primary particles. Secondary particles form due to chemical reactions, and are very important in the giant planets.

Secondary particulate matter formation is more complicated due to their forming from chemical reactions. Gas can form from low-vapor pressure products that then undergo nucleation to form new particles or condensation on already existing particles. Secondary particulate matter can also form due to coagulation between particles or due to a reaction on the surface of an existing particle creating condensed-phase products. Finally, they can form within the aqueous phase in a cloud. There are a variety of ways to form secondary particulate matter that are important for cloud formation.

Particle motions contribute to the observed size distribution and the number concentration of aerosols in the atmosphere. Particles in a planetary atmosphere are subject to gravitational forces. Particles will fall when the force of gravity is applied to them and will continue to accelerate until the frictional forces equals the applied force. The particles will fall at a constant velocity known as terminal velocity. The influence of gravity is felt more on bigger particles in the atmosphere than the smaller particles. Smaller particles undergo Brownian diffusion, which is the random movement of particles suspended in a fluid. A classic example of this diffusion is how smoke particles diffuse in the air. The motions of the particles in the atmosphere can change the size distribution of particles by changing the frequency of particles interactions, which will have an effect on droplet growth.

The microphysical parameters of interest are summarized in Figure 2.4. This figure shows the life span of an aerosol in the atmosphere of a planet. It starts at the creation of a particle, and shows the three possible growth mechanisms – condensation, coagulation, and coalescence. It then displays the loss mechanism, which is precipitation. Precipitation can be either in the form of rain, or in the form of dry deposition where the aerosols collect on a solid surface and decrease their concentration in the air. Precipitation will be further examined in Section 2.6.3.

The atmosphere starts with an initial distribution of molecular embryos that are the foundation for aerosols. Embryos can become cloud droplets. The first process that the embryos go through is nucleation. Nucleation is the creation of liquid droplets in a saturated vapor environment creating Cloud Condensation Nuclei, CCN. There are many forms of nucleation—homogenous, heterogeneous, chemical and ice nucleation.

Condensation is a process that occurs when that atmosphere reaches super saturation. At this point, the water vapor in the atmosphere can condense on to the CCN and form droplets. The amount of CCN present in the atmosphere along with the amount of water vapor controls the concentration and size of these droplets. If there are many CCNs, the droplets will not grow very large as the water vapor is spread among many CCNs. Conversely, the droplets will get larger with fewer CCN due to less competition among droplets. The rate of condensation starts out quickly, but will gradually decrease as the water vapor supply is used. This is when other growth mechanisms such as coagulation and coalescence become dominant.

Coagulation refers to the formation of a single particle via collision and the sticking together of two smaller particles. Smaller particles undergo rapid Brownian motion, which leads to enough particle-particle collisions to cause coagulation. Similar to condensation, coagulation leads to a decrease in small particles as they coagulate to each other. Larger particles only increase slightly from the addition of these smaller particles. When two particles of similar size interact with each other, it leads to a change in the size distribution. Coagulation depends on the diameter of a particle, how quickly the smaller particles are brought together, and the concentration of particles (Fuchs, 1964). Coalescence, which is similar to coagulation, will also result in droplet growth. However, coagulation is an irreversible process while coalescence is reversible as coalescence is a process by which two droplets stick together to form a single droplet.

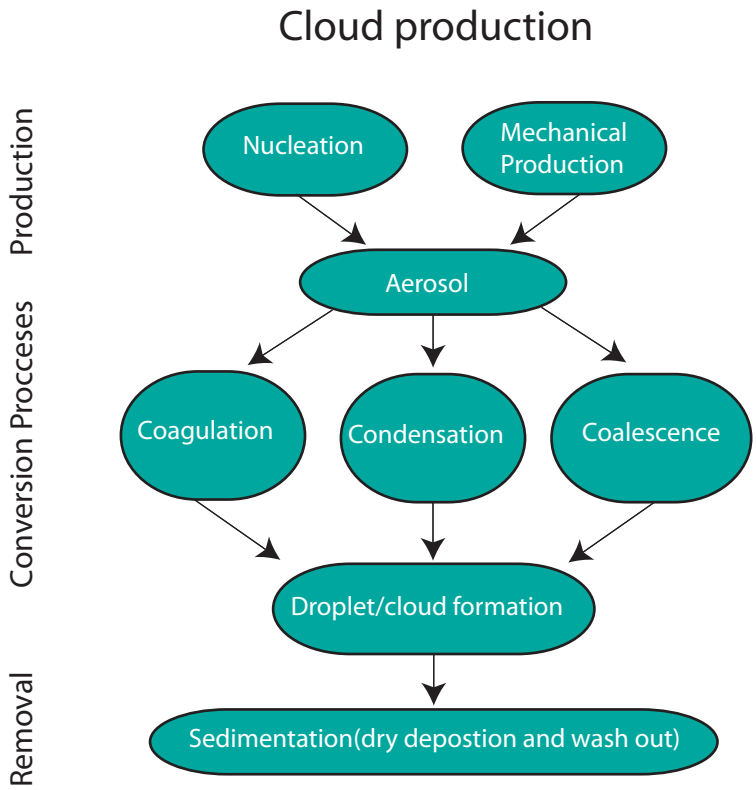

Figure 2.4 A flow chart showing the cloud production processes as well as the destruction. The creation of a cloud involves the production of aerosols followed by the conversion process to droplet/cloud formation. The removal process was not previously included in the ECCM but was added in this work.

2.6 Cloud Microphysics Models

Earth based cloud microphysics studies are far more advanced than those for other planetary atmospheres. What is learned at Earth can be applied to the other planets. All of the giant planets contain a large number of suspended particles that are either aerosols, CCN, or cloud droplets. While they are not responsible for much of the planet's mass, they are very important to the radiative energy budgets of these planets.

The radiation at a planet plays a significant role in determining the atmospheric dynamics.

Precipitation has long been studied on Earth and similar approaches can be applied to Jupiter. There are fewer unknown variables for Earth, such as eddy diffusion coefficient, convective velocity scale, and actual cloud measurements allowing for a more precise calculation than can currently be executed for Jupiter. Certain Earth cloud data will be used in this study to validate the model. It is not the focus of this study to calculate the effects of precipitation on all Earth clouds, but instead Earth is used to confirm that the model formulation reasonably represents terrestrial cloud processes. The Jupiter clouds are assumed to undergo similar atmospheric processes as Earth clouds. This assumption is based on known similarities between the clouds observed on both planets including the presence of lighting, and the likely presence of water clouds on Jupiter.

Rossow *(1978)* and Carlson *et al. (1988)* calculated cloud microphysics for Earth, Venus, and Jupiter. These papers added the calculation of time constants for each of the microphysical processes—condensation, coagulation, precipitation, and coalescence. The weakness of their approach is that they made no attempt to calculate the vertical profiles of the condensation. Instead, they only looked at the cloud base. The other shortcoming of their approach is that many of the values and/or constants used in this calculation are unknown due to lack of measurements. This includes, but is not limited to, the supersaturation values, and the use of gravitational coalescence collection efficiency. However, at this time no measurements and assumptions have to be made. This formulism will be further examined in section 2.6.1.

Previous researchers have also sought to solve this problem. Zuchowski (2009) modeled the effects of precipitation using the Stokes velocity, but did not allow for the

variation of particle sizes. Hueso and Sanchez-Lavega (2001) used a three dimensional cloud model and accounted for precipitation by multiplying the condensate by a fraction, 0 to 1, to represent the amount that remains in the cloud. Another approach to modeling microphysics in the giant planets is to use the method of Lunine *(1989)*, which models the atmosphere in brown dwarfs. This research is based on an investigation of iron clouds deep in the Jovian atmosphere by Prinn and Olaguer *(1981)*. The paper builds on the vertical transport of condensates by Weidenschilling and Lewis *(1973)*, which is the basic formulation for the ECCM. There are two types of clouds considered in the model. The first cloud is a dust-like cloud, which is probably located in the stratosphere. The second is a tropospheric cloud that allows for the downward transport by precipitation and upward transport by turbulent mixing. This category is further broken down into two subcategories. The first subcategory is the frozen-in cloud particles where the particles are so small that precipitation is overtaken by the turbulent mixing. The second subcategory is where the particles are allowed to grow large enough as in convective clouds. The turbulent transport and downward precipitation are compared in this situation.

Marley *et al.* (1999) also modeled water and silicate clouds in extrasolar giant planets. This paper was a variation on the Lewis *(1969)* model. To calculate the cloud particle sizes, they applied the method of Rossow *(1978)*. Marley *et al. (1999)* had two different atmospheric end members. In the first case, the atmosphere is quiescent and the precipitation rate matches the faster rate of coagulation and condensation determining the particle size. The second case is a turbulent atmosphere where mixing is compared to precipitation. This second case requires fewer assumptions. It is this case that is further

examined in Ackerman and Marley *(2001)*, and their calculation is detailed in section 2.6.3.

2.6.1 Rossow's Cloud Microphysics

Rossow (1978) and Carlson and Rossow (1988) estimated the time constants for different cloud microphysical processes at the cloud base—coagulation, condensation, coalescence, and precipitation. The microphysical timescale formulae depend on the flow regimes, which are based on Reynolds number, Re, a dimensionless number that relates the internal forces to the viscous forces, and Knudsen number, Kn, a dimensionless number that relates the molecular mean free path to a characteristic path length. These two dimensionless parameters dictate the atmospheric regime based on the particle size.

There are a few key assumptions that are used by Rossow *(1978)* and are elaborated on by Carlson *et al. (1988)*. The first assumption is that the cloud's mass density is approximately equal to the vapor density of condensable species at the cloud base. This assumption results in a lower limit of growth times in the atmosphere as it dictates the amount of the specie. The second assumption is that the cloud layer thickness is on the order of a scale height. This sets the upper limit on particle removal times as it limits the layer. The atmosphere is assumed to be well mixed, which puts a lower limit on growth times. Finally, they assume the size distribution of the particles and the process dependency on the particle sizes are adequately represented by a mass-weighted mean particle size. Using these assumptions, an order of magnitude estimate

for the time constants can be estimate. The values presented by Carlson *et al.* (1988) are based only on the upper limit of cloud particle sizes at the cloud base.

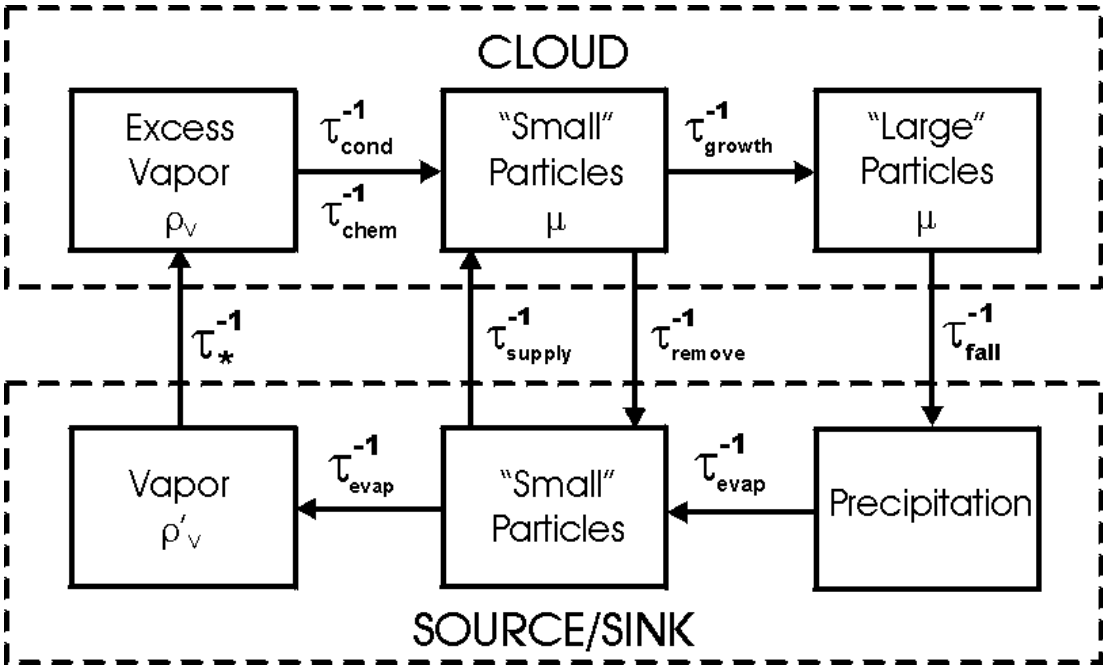

Figure 2.5 A flow chart from Rossow (1978) showing the relationship between clouds and their sources and sinks. For our study, only τ_{fall} is examined further.

Rossow's calculation of the microphysics time constants are based on the regime of the atmosphere. The regime is classified by knowing the Knudsen (Kn) and Reynolds (Re) number. The Knudsen number is a value that determines whether the interaction of an atmospheric gas with aerosols is best described by continuum mechanics (classical regime) or by statistical mechanics (gas kinetic regime). The Reynolds number determines the nature of the gas flow past a moving particle and is used to determine if the flow is 'rough,' i.e. turbulent, or 'smooth'. Using the Knudsen and Reynolds number, the regimes that are considered are the gas kinetic regime (Kn >> 1), the classical laminar flow regime (Kn << 1 and Re <<1), and the classical turbulent flow regime (Kn << 1 and Re >> 1). The gas kinetic regime is based on the theory that gasses consist of a large

number of small particles. These particles are all in constant and random motion. Laminar flow, which is also known as streamline flow, is characterized by high momentum diffusion and low momentum convection or, in other words, the flow is 'smooth'. Classic turbulent flow regime is characterized by chaotic, stochastic property changes, i.e. the flow is rough.

The Knudsen number is the ratio of gas molecular mean free path and the cloud particle radius, r. The mean free path, λ_m, is the average distance covered by a particle between successive impacts with other particles and is defined as:

$$\lambda_m = \frac{RT}{\sqrt{2}\pi Na(2r)^2 P} \qquad 2.2$$

where Na is the Avogadro's number. The Knudsen number, Kn, is defined as:

$$Kn = \frac{\lambda_m}{r} \qquad 2.3$$

The Reynolds number is defined as:

$$\mathrm{Re} = \frac{2r\rho_g v}{\eta} \qquad 2.4$$

where ρ_g is the gas density, η is the dynamic viscosity, and v is the particle velocity.

Viscosity is the measure of a fluids resistance and how it responds when an external stress is placed on it. Another way to describe viscosity is it is the thickness of a fluid. Air has a lower viscosity than water and both have a lower viscosity than honey. Hansen *(1979)* derived a relationship for the viscosity of hydrogen, $\eta_{H2,}$ in units of micropoise. This relationship can be used to calculate the viscosity in the giant planets, as

it not only includes hydrogen, but helium, as these two species are most prominent in the atmosphere. The relationship starts with viscosity of hydrogen, η_{H2}:

$$\eta_{H2} = 90.6 *(T/300)^{.6658} \qquad 2.5$$

and then:

$$\eta_{H2=}\eta_{H2}/(1+4/T) \qquad 2.6$$

The viscosity of helium, $\eta_{He,}$ in units of micropoise:

$$\eta_{He} = 191.6*(T/300)^{.7176} \qquad 2.7$$

and then:

$$\eta_{He} = \eta_{He}/(1-11.4/T) \qquad 2.8$$

The cross section, in cm^2, for hydrogen, Q_{H2}, helium, Q_{He}, and hydrogen-helium, $Q_{H2\text{-}He}$ are defined as:

$$Q_{H2} = 32.3*(1+4/T)*(300/T)^{.1658} \qquad 2.9$$

$$Q_{He} = 21.5*(1-11.4/T)*(300/T)^{.2176}$$

$$Q_{H2\text{-}He} =((Q_{H2}^{.5}+Q_{He}^{.5})/2)^2$$

The ratio of pure to mixture for hydrogen, L_{H2}, and helium, L_{He} are defined by Hansen 1979:

$$L_{H2} = 1+.7967*(X_{He}/X_{H2})*(Q_{H2\text{-}He}/Q_{H2}) \qquad 2.10$$

$$L_{He} = 1+.5634*(X_{H2}/X_{He})*(Q_{H2\text{-}He}/Q_{He})$$

The viscosity, η, of the atmosphere of a giant planet is then defined as:

$$\eta = \eta_{H2}/L_{H2}+\eta_{He}/L_{He} \qquad 2.11$$

Viscosity is used to calculate the terminal velocity, and thus is needed to calculate the precipitation time constants.

It is possible that there is stronger wind shear on the giant planets than on Earth, which would result in the cloud droplets being destroyed by small-scale winds, such as wind shear, before the droplets can precipitate. The only data on cloud lifetime at Jupiter comes from the New Horizon mission, which traced an ammonia cloud and found that the clouds lifetime was less than 40 hours (Reuter *et al.*, 2007). However, no data exists on the lifetime of the water clouds. Large-scale winds will have minimal effect on the lifetime of a cloud. Wind speeds will decrease as a result of the drag caused by the cloud droplets (Fuchs, 1964). Small-scale turbulence is also expected to decrease the lifetime of droplets in clouds especially when wind shear is considered. Therefore, the lifetime of cloud droplets can be further reduced below that of the precipitation time scale.

The precipitation time constant is calculated by dividing the scale height by the terminal velocity. For regimes where the Knudsen and Reynolds numbers are less than one, the well-known Stokes expression for the terminal velocity is appropriate and is defined as:

$$v_{fall} = \frac{2\rho_{cond} g r^2}{9\eta} \qquad 2.12$$

where v_{fall} is the terminal velocity, ρ_{cond} is the mass droplet density of a species, g is the local gravitation acceleration, r is the radius of the droplet and η is the dynamic viscosity. The viscosity for Jupiter is calculated following Hansen (1979) who derived a relationship based on laboratory experiments for viscosity that included hydrogen and helium, the two

most abundant species in the Jovian atmosphere. To describe how the terminal velocity varies with changes in the Knudsen number, the Cunningham factor, $1 + \beta Kn$, which is a correction factor to account for the drag force on a particle is used (Cunningham, 1910). For this work, β is equal to 4/3 for all Knudsen numbers (Berry and Reinhard, 1974). The terminal velocity varies with low and intermediate values of the Reynolds number where the Reynolds number is less than 70. This variation is described by the factor:

$$v_{fall} \propto 1 + \sqrt{\frac{C_D \mathrm{Re}}{24}} \qquad 2.13$$

where C_D is the drag coefficient (Abraham, 1970). This factor is also valid when the Reynolds number is greater than 70, but in this case the drag coefficient is roughly constant and is approximately equal to 0.2 (Prandtl, 1953). These factors result in the following terminal velocities, v_{fall}, for each flow regime:

$$v_{fall}(r) = \frac{r^2 2\rho_{cond} g}{9\eta}, \mathrm{Re} < 70, Kn < 1 \qquad 2.14$$

$$v_{fall}(r) = r\sqrt{\frac{40\rho_{cond} g}{3\rho}}, \mathrm{Re} > 70, Kn < 1$$

$$v_{fall}(r) = r\sqrt{\frac{\mu\pi}{2N_a k_B T}}\frac{8\rho_{cond} g}{27\rho}, Kn > 1$$

Where μ is the mean molecular mass of the atmosphere. ρ_{cond} represents the mass density of a particle itself.

Once the terminal velocity is obtained it is possible to calculate the gravitational fallout timescale, τ_{fall}, which is inversely proportional to the terminal velocity:

$$\tau_{fall} = \frac{H}{v_{fall}} \qquad 2.15$$

where H is the scale height, defined as:

$$H = \frac{RT}{\mu g} \qquad 2.16$$

Using the definition of the scale height and the terminal velocity the precipitation time, in seconds, constant for the three regimes become:

$$\tau_{fall} = \frac{9\eta k_B T}{2\rho_{cond}\mu g^2 r^2} (\mathrm{Re} << 70, Kn << 1) \qquad 2.17$$

$$\tau_{fall} = \left[\frac{3\rho(k_B T)^2}{40\rho_{cond}\mu^2 g^3 r}\right]^{0.5}, (\mathrm{Re} >> 70, Kn << 1)$$

$$\tau_{fall} = \frac{27\pi\rho\left(\frac{2k_B T}{\pi\mu}\right)^{3/2}}{16\rho_{cond} g^2 r}, (Kn >> 1)$$

where ρ is the density of the atmosphere.

The precipitation timescale depends on particle size, resulting in a range of velocities being found for a size distribution. The larger the droplet the shorter the amount of time it spends in the cloud. On Earth, a typical rain droplet is 2 mm in diameter. Sleet, which is a small ice particle, varies in size from .5 to 5 mm, while snow varies from 1 mm to 2 cm. Cloud mean particle radius on Earth is typically in the micron to a few micron range. The nephelometer on the Galileo Probe found that the cloud particles on Jupiter were in the sub-micron to a few micron range showing similar characteristics to non-precipitating clouds on Earth (Ragent *et al.*, 1998). We assume that

water droplets would have similar characteristics as in terrestrial clouds, extrapolating from similar cloud particle sizes.

In Figure 2.6, the precipitation time constant is shown for a range of particle sizes. It can be seen that once a liquid droplet ~2mm in radius reaches its terminal velocity, the precipitation lifetime is $\sim 10^4$ second, approximately 3 hours. Snow would have a slightly shorter precipitation lifetime than the liquid droplet, based only on its larger size, however due to drag on the particle it should have a longer lifetime. This time scale will later be compared to the values calculated for the eddy diffusion coefficient to determine if the precipitation lifetime is quicker.

Besides precipitation, the other sink for a cloud is the atmospheric dynamics and the motions that a cloud droplet experiences vary from less than a centimeter to a planetary scale. While large-scale winds will have minimal effect on the lifetime of a cloud, the wind cannot be simply added to the velocity of the wind. The wind will actually be slowed down as a result of the drag caused by the cloud droplets (Fuchs, 1964). Small-scale turbulence is also expected to decrease the lifetime of droplets in clouds especially when wind shear is considered. Therefore, the time scale of cloud droplets will be further reduced below that of the precipitation time scale.

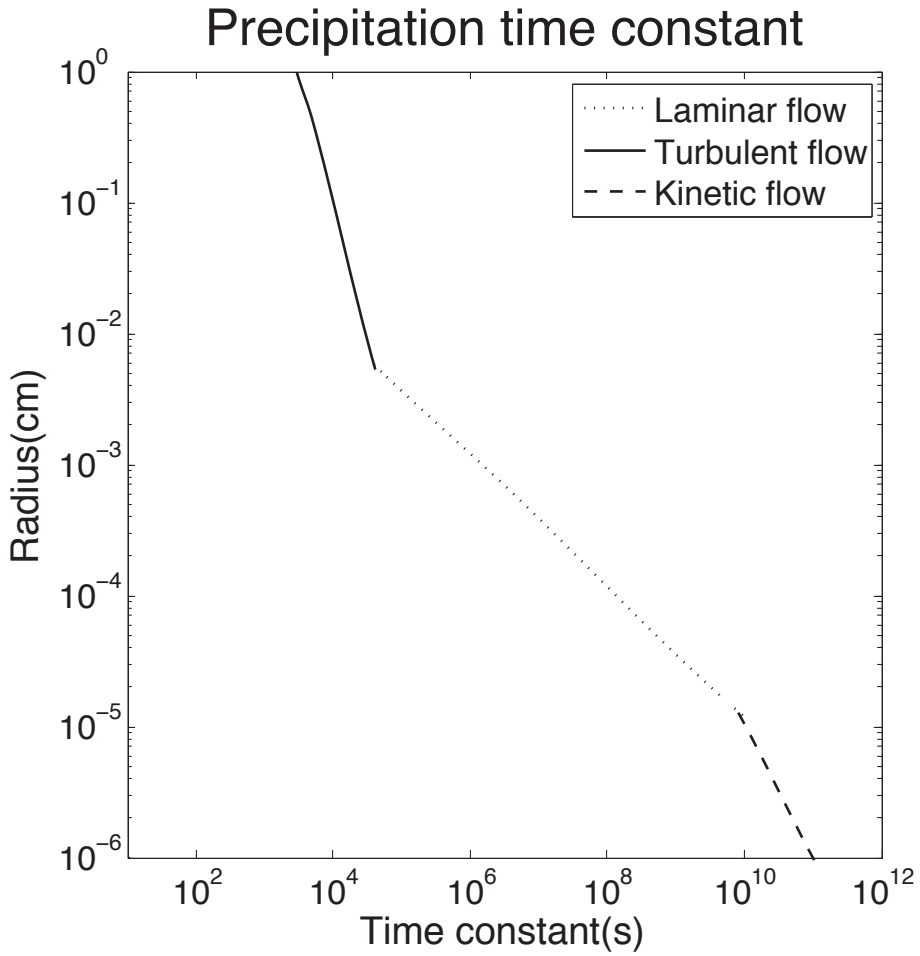

Figure 2.6 Three different flow regimes are shown above. The values are calculated at the cloud base with the radius of the cloud particles being varied. Once the droplets reach their critical size, they have a lifetime of approximately three hours. Aerosols can live in the atmosphere for more than three Earth years.

Information about the precipitation time constant can be used to better understand the lifetime of a cloud. Using this information and information on the dynamics in the atmosphere, the true lifetime of a cloud can be assessed in the different regimes thought to be present on Jupiter. Additionally, this would aid in understanding the cycling of the condensable species in the atmospheres from vapor to liquid/solid form.

When making measurements this becomes important as many wavelengths, such as radio wavelengths, are more sensitive to species in the vapor phase form than the liquid/solid form.

2.6.2 Maximum Precipitation Rate

Rossow (1978) calculated the lifetime of the droplets in the atmosphere depending on their size, and the maximum precipitation rate can be calculated as well. In order to calculate the maximum precipitation rate, we assume a unit mass of saturated air that rises at a speed, w. A range of the different vertical velocities will be used based off of the work of Stoker (1986), and Hueso and Sanchez-Lavega (2001). The first model developed to quantify moist convection and vertical velocity for Jupiter was Stoker (1986). This model was a 1-D thermodynamic model that involved parcels rising in the atmosphere and as they rose they could experience entrainment from the cold air they were rising through. Stoker modeled many different cases of temperature and relative humidity, as these are relatively unknown and may vary globally. For the ammonia cumulus cloud, a maximum vertical velocity of only 1.7×10^3 cm s^{-1} was found. This is due to only a small amount of energy being available from the condensation of ammonia to drive the moist convection. Water, on the other hand, releases more energy, which can result in energetic moist convection. The value for the vertical velocity of cumulus clouds on Earth is 5.0×10^3 cm s^{-1} (Browning, 1977). This value is greater on Jupiter as the water can accelerate over a larger vertical distance before the troposphere is reached. Stoker found a range of values for the water cloud's vertical velocity that varied from

three to several hundred meters per second. A 3-D model was developed by Huseo and Sanchez-Levega (2001) that calculated the moist stability using fully integrated Navier-Stokes equations. The expected vertical velocities from this model are of the order of 4.0 to 15.0 × 10^3 cm s^{-1}. Similar to the Stoker model, ammonia is shown to not display high updrafts as the cloud is in a more stable part of the atmosphere.

In order to calculate the maximum precipitation rate, a rising parcel of air below the cloud base is considered. As the parcel rises through the atmosphere, the vapor of the condensable species will condense. An approximation is then used to calculate the maximum precipitation rate by assuming that all the condensate will precipitate out as rain or snow and that there is no super saturation. Taking the entropy equation, applying reverse saturated adiabatic processes, and differentiating results in the entropy equation for a reversible saturation adiabat condition:

$$C_{pd}\,d(\ln T) - R_d\,d(\ln P) + \lambda_v d\left(\frac{X_w}{T}\right) = 0 \qquad 2.18$$

where C_{pd} is the heat capacity, λ_v is the latent heat of vaporization, X_w is the mass mixing ratio of water vapor, p is the atmospheric pressure, and R_d is the ideal gas constant for dry air. Expanding the last term in equation 2.18 results in the entropy equation for a reversible saturated adiabat:

$$d\left(\frac{X_w}{T}\right) = \frac{dX_w}{T} - \frac{X_w}{T^2}\,dT \qquad 2.19$$

Substituting equation 2.19 into 2.18 and writing dlnT = dT/T, and knowing the relationship between the hydrostatic equation and the ideal gas equation:

$$dp = -\rho g dz = -\frac{P}{R_d T}\,g dz \qquad 2.20$$
$$R_d T d\ln P = -g dz$$

where z is height. This results in:

$$C_{p_d} dT + g dz + \lambda_v dX_w - \frac{\lambda_v X_w}{T} dT = 0 \qquad 2.21$$

Since $\lambda_v X_w dT/T$ is about two orders of magnitude smaller than $\lambda_v X_w$ it can therefore be neglected. This leaves:

$$C_p \frac{dT}{dz} + g + \lambda_v \frac{dX_w}{dz} = 0 \qquad 2.22$$

dT/dz is simply the moist adiabatic lapse rate for air in the cloud, Γ_m, and g/C_{pd} is the dry adiabatic lapse rate, Γ_d. Making this substitution:

$$\frac{dX_w}{dz} = -\frac{g}{\lambda_v}\left(1 - \frac{\Gamma_m}{\Gamma_d}\right) \qquad 2.23$$

The change in the water vapor mixing ratio with height can be expanded, and recognizing that dt/dz is simply the inverse of the vertical wind speed results in:

$$\frac{dX_w}{dz} = \frac{dX_w}{dt}\frac{dt}{dz} = \frac{dX_w}{dt}\frac{1}{w} \qquad 2.24$$

Substituting 2.23 into 2.24 gives:

$$\frac{dX_w}{dt} = -\frac{g}{\lambda_v}\left(1 - \frac{\Gamma_m}{\Gamma_d}\right) w \qquad 2.25$$

Then multiplying by the specific volume of air, α, will give the amount of water (grams) formed per m^3 of air per second. Then multiplying through by Z, where Z is the height where the cloud density has fallen off by 1/e when compared to the cloud base density, gives the amount of rain per second in a column.

$$P_{rate} = -\frac{g\alpha}{\lambda_v}\left(1 - \frac{\Gamma_m}{\Gamma_d}\right) wZ \qquad 2.26$$

Using this equation, the maximum precipitation rate was estimated for 0.4, 1, 4, and 10 × solar oxygen enrichments on Jupiter. A range of vertical velocities was used with a maximum of 1.5×10^4 cm s^{-1}, from Hueso and Sanchez-Lavega (2001) and the minimum of 1×10^2 cm s^{-1} from Stoker (1986). The cloud bases for the 0.4, 1, 4, and 10 × solar cases correspond to 3.9, 4.6, 6.5, and 9.1 bar, respectively. This results in a range of precipitation rate with the lowest rainfall rate of 8.6×10^{-8} g cm^{-2} s^{-1} for the 0.4 × solar case and 1×10^2 cm s^{-1} wind to the greatest rainfall rate of 1.19×10^{-4} g cm^{-2} s^{-1} for the 10 × solar case with 1.5×10^4 cm s^{-1} winds. For Earth, using a wind speed of 1 m s^{-1}, the maximum precipitation rate was found to be 2.46×10^{-7} g cm^{-2} s^{-1}, which is on the lower range of the maximum precipitation rate on Jupiter. This is to be expected due to the lower gravity and wind speeds at Earth.

Similar to the lifetime of a cloud, understanding the precipitation rate can become important when designing an instrument to observe the cloud region. The phase, gas/liquid/solid, of a species affects what wavelengths it is visible in, and the presence of precipitation can change this phase. Namely, will the specie be condensed in the cloud as a solid/liquid, will it be precipitating out of the cloud, or will it have re-evaporated below the cloud. Where re-evaporation occurs can be important when determining the deep elemental abundance of a specie. Therefore, more work needs to be done to examine the distance precipitation falls before returning to the vapor phase as well as the rate at which the rain is falling.

Table 2.1 This table represents the maximum water precipitation rates for 1 ×, 4 ×, and 10 × solar water abundances on Jupiter.

Maximum Precipitation

	$U = 1.5x10^4 cms^{-1}$	$U = 40x10^3 cms^{-1}$	$U = 1x10^2 cms^{-1}$
10 x solar	$1.19 \times 10^{-4}\ gcm^{-2}s^{-1}$	$3.18 \times 10^{-5}\ gcm^{-2}s^{-1}$	$7.96 \times 10^{-7}\ gcm^{-2}s^{-1}$
4 x solar	$6.77 \times 10^{-5}\ gcm^{-2}s^{-1}$	$1.08 \times 10^{-5}\ gcm^{-2}s^{-1}$	$4.51 \times 10^{-7}\ gcm^{-2}s^{-1}$
1 x solar	$3.51 \times 10^{-5}\ gcm^{-2}s^{-1}$	$9.65 \times 10^{-6}\ gcm^{-2}s^{-1}$	$2.34 \times 10^{-7}\ gcm^{-2}s^{-1}$
0.4 x solar	$1.29 \times 10^{-5}\ gcm^{-2}s^{-1}$	$3.44 \times 10^{-6}\ gcm^{-2}s^{-1}$	$8.60 \times 10^{-8} gcm^{-2}s^{-1}$

2.6.3 Ackerman and Marley Precipitation Formulation

The lack of a sink for the clouds in the ECCM results in modeling the upper limits of the cloud's concentrations. Ackerman and Marley (2001), solved the over estimation of cloud concentrations by allowing the clouds to rain. Previous cloud models have sought to solve this issue such as Lunine (1989), which expanded on Weidenschilling and Lewis and was used to model the atmospheres of brown dwarfs by including different cloud types. Zuchowski (2009) modeled the effects of precipitation using the Stokes velocity, but did not allow for the variation of the particle sizes. Hueso and Sanchez-Lavega (2001) used a three dimensional cloud model and accounted for precipitation by multiplying the condensate by a fraction to represent the amount that remains in the cloud.

Marley (1999) used Rossow (1978) microphysical time constants for his calculation of cloud droplet size and examined two different cases. In the first case, the atmosphere was quiescent and the precipitation rate was faster than all other microphysical process, namely coagulation and condensation. The second case was a turbulent mixing atmosphere where mixing and precipitation were both present. Ackerman and Marley

sought to further examine the turbulent mixing model and expand upon the model to allow for precipitation. They used Lewis (1969) to find the cloud bases and cloud concentrations. They then assumed that the clouds were horizontal, homogeneous structures. Rather than calculating the time constants for precipitation, they calculated the change in the cloud concentration by assuming both turbulent diffusion and precipitation in the horizontally uniform cloud deck. Or, in other words, Ackerman and Marley compared the upward turbulent motion of condensate and vapor to the downward transport of condensate caused by precipitation to calculate the change in cloud concentration. They derived the following equation:

$$-K\frac{\partial q_t}{\partial z} - f_{rain} w_* q_c = 0 \qquad 2.27$$

where K is the vertical eddy diffusion coefficient, q_t is the total mixing ratio ($q_t = q_c + q_v$), q_c is the mixing ratio of the condensate, q_v is the mixing ratio of the vapor, f_{rain} is the mass-weighted droplet precipitation to the convective velocity scale, w_*. Rearranging the equation for q_c allows us to solve for the change in each constituent individually.

We follow a similar approach to Ackerman and Marley, and expand upon their work by examining the case of a water cloud on Jupiter and Earth. This allows for validation of the Jovian model by applying the ECCM and microphysics schemes to Earth. As discussed earlier, the water cloud has the highest concentration and is the most extensive Jovian cloud, assuming similar enrichment for each condensables. The liquid water cloud has been inferred due to the presence of lightning and is the only liquid cloud predicted in the atmosphere of Jupiter. Thus, the water cloud is the only cloud where

rain is the precipitation instead of snow. The values for q_c, q_v, and q_t are calculated outputs from the ECCM.

For Jovian ammonia clouds, the value of f_{rain} was found to be between one and three. There was no f_{rain} prescribed for the water cloud on Jupiter, therefore it was calculated using the expression derived by Ackerman and Marley:

$$f_{rain} = -\frac{q_t}{q_c}\frac{L}{z}10^{\left(\frac{q_t(z)}{q_{below}}\right)} \qquad 2.28$$

and was found to be 3.38. We rounded f_{rain} to 3, and this value is within the ammonia cloud range on Jupiter, as well as, within the water cloud range on Earth, f_{rain} between 2 and 6. The convective velocity scale from mixing-length theory is defined as the eddy diffusion divided by the mixing length. The value for convective velocity prescribed by Ackerman and Marley is 100 cm s^{-1}. This value is the same as the value that has been calculated on Earth, and is approximately equal to the updraft speed in convective thermals, though the max updraft speed on Earth is 50 times greater as shown by Browning (1977). The actual value for Jupiter may vary from this as the convective velocity is calculated using the buoyancy force and thermal size. The buoyancy force is dependent on the gravity and the vertical turbulent heat flux. The gravity is greater on Jupiter at the 1 bar level than it is at Earth surface, and the height a thermal has to travel through before it reaches the tropopause is greater. Therefore, there is some uncertainty in the value for the convective velocity scale. The eddy diffusion coefficient remains uncertain for Jupiter's atmosphere, and the different ways it is inferred –lyman alpha, and helium, ammonia, carbon monoxide, and methane measurements—are detailed in the next section.

2.6.3.1 Eddy Diffusion Coefficient

The eddy diffusion coefficient remains uncertain for Jupiter's atmosphere. One approach to estimating it is to use the radiative transfer equation to analyze the height distribution of a tracer gas, or invert airglow data as its behavior depends on vertical mixing. The results are highly model dependent, however. Monitoring the vertical distribution of heavier gases, such as hydrocarbons, can be used to estimate the eddy diffusion coefficient. At the homopause, the eddy diffusion coefficient is equal to the molecular diffusion coefficient. This however, cannot be used to obtain the eddy diffusion coefficient of hydrocarbons as they experience photochemical depletions. The eddy diffusion coefficient is then obtained from photochemical models and measurements. Ideally, a species that does not experience photochemistry, such as argon, will be used to calculate the eddy diffusion coefficient in the future.

The distribution of methane and other hydrocarbons, employed in Atreya et *al.* (1981) provides a tighter constraint on the value of the eddy diffusion coefficient. These authors derived an equatorial value of eddy diffusion coefficient of 1×10^6 cm^2 s^{-1} at the homopause where the pressure is 10^{-6} bar. Drossart (1999) used ISO's Short Wavelength Spectrometer to measure methane emissions at Jupiter and calculated a homopause value of eddy diffusion coefficient as 6-8 $\times$ 10^6 cm^{-2} s^{-1} at high latitudes. Deeper in the troposphere, the eddy diffusion is calculated to vary from 4×10^7 to 4×10^9 cm^2 s^{-1}, based on considerations of primordial CO in Jupiter's interior (Fegley and Lodders, 1994; Griffith and Yelle, 1999). Bezard *et al.* (2002) calculated the carbon monoxide mixing

ratio using a spectra of lines near 4.7 μm. They estimated the eddy diffusion coefficient with these measurements to be several hundred $cm^2\ s^{-1}$ at the tropopause and to be $6 \times 10^8\ cm^2\ s^{-1}$ at 10 bar.

Unfortunately, other than the inference from carbon monoxide spectra, the values calculated for the eddy diffusion coefficient are high in the atmosphere, leading us to rely mainly on an analog with Earth's eddy diffusion coefficient that decreases from the upper atmosphere to the troposphere and then increases once in the troposphere (Hunten, 1975). This change may be signaling a switch from a stable environment to an unstable environment. As the atmospheric pressure increases below the homopause, the value for eddy diffusion coefficient decreases proportional to $n^{-0.5}$ in Jupiter (Atreya and Donahue, 1981), where n is the number density. Based on the ammonia distributions in the lower stratosphere of Jupiter derived from the Hubble Space Telescope Faint Object spectra, Edgington *et al.* (1999) found that an $n^{-0.6}$ variation gives a better fit to the stratospheric vertical mixing. This results in the eddy diffusion at the tropopause of Jupiter to be approximately $10^3\ cm^2\ s^{-1}$ at 0.1 mbar level, which matches the results of Bezard *et al.* (2002). In troposphere of Jupiter, the value increases based on the terrestrial analog due to downward motions (Hunten, 1975). For our study, we take a range of eddy diffusion coefficients from $1 \times 10^5\ cm^2\ s^{-1}$ to $1 \times 10^8\ cm^2\ s^{-1}$. This range of eddy diffusion coefficients allows for a full range of possible values for precipitation. A summary of the eddy diffusion measurements is found in Table 2.2.

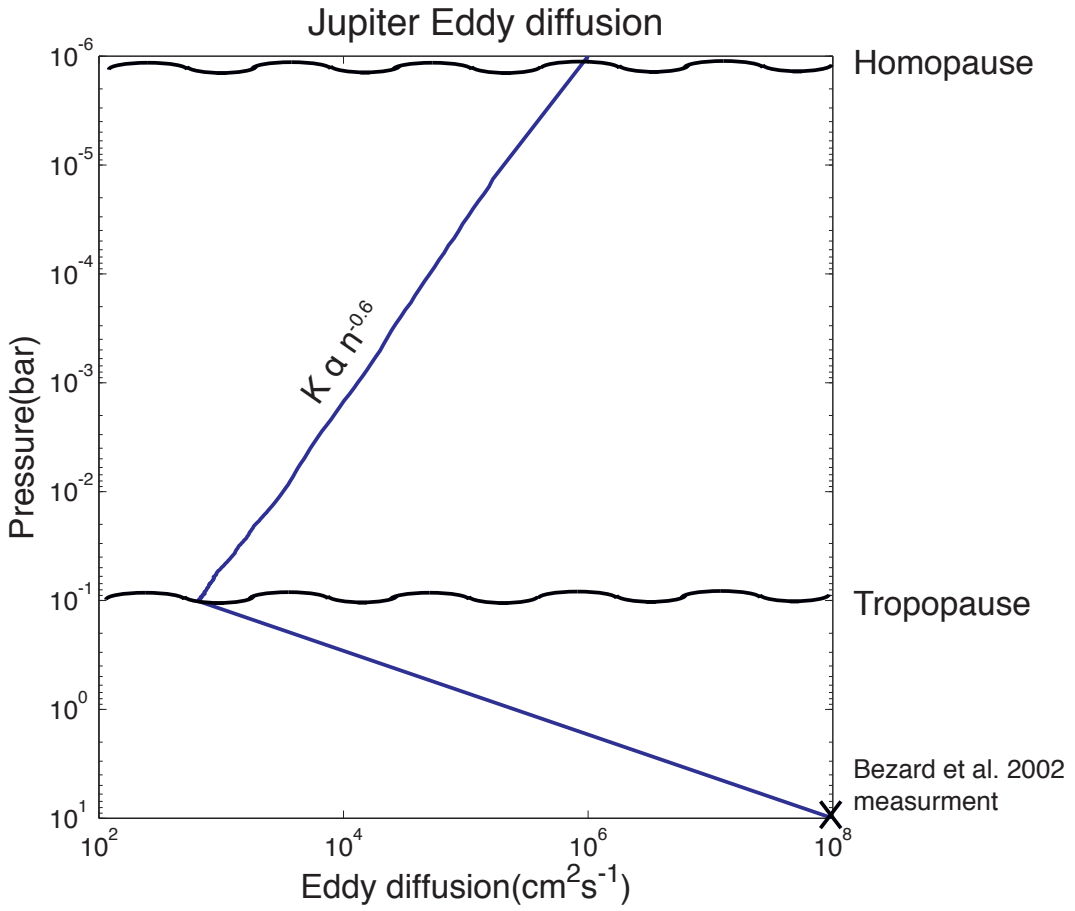

Figure 2.7 A summary plot of the eddy diffusion in Jupiter's atmosphere based on measurements and assumptions. Table 2.2 displays the measurements used for this study. From the homopause to the tropopause the eddy diffusion is proportional to the number density to the -0.6 as seen in (Edgington, 1999).

Table 2.2 Summary of eddy diffusion coefficient measurements from hydrocarbon and carbon monoxide measurements.

Eddy Diffusion Coefficient measurements

Height	Eddy Diffusion	Method	Source
homopause	1 x 10^6 cm^2s^{-1}	Hydrocarbon mixing ratio	Atreya et al. 1981
homopause	6-8 x 10^6 cm^2s^{-1}	Methane emissions	Drossart 1999
tropopause	100's cm^2s^{-1}	Carbon Monoxide Mixing ratio	Bezard et al. 2002
troposphere	4 x 10^7 to 4 x 10^9 cm^2s^{-1}	Primodial carbon monoxide	Fegley and Lodder 1994 Griffith and Yelle 1991
10 bars	6 x 10^8 cm^2s^{-1}	Carbon Monoxide Mixing ratio	Bezard et al. 2002

AM assumed that the eddy diffusion coefficient is the same as the heat diffusion derived for free convection from Gierasch & Conrath *(1985)*:

$$K = \frac{H}{3}\left(\frac{L_m}{H}\right)^{4/3}\left(\frac{RF}{\mu\rho_a c_p}\right)^{1/3} \qquad 2.29$$

where L_m is the turbulent mixing length, and ρ_a is the atmosphere's density, and c_p is the specific heat of the atmosphere at constant pressure. F is the heat flux, and σ_s is the Stefan-Boltzmann constant. AM assumes the interior heat to be transported completely through the convective heat flux: $F = \sigma_s T^4_{eff}$. The mixing length:

$$L_m = H\max(\Lambda, \Gamma/\Gamma_d) \qquad 2.30$$

where Λ is the minimum scaling applied to L_m, and Γ is the local adiabatic lapse rate. The convective velocity is defined as:

$$w_* = K/L_m \qquad 2.31$$

For equation 2.29, AM do have certain constraints on the variables. The minimum scaling variable Λ is assumed to be .1. Due to the fact that convective heat fluxes are diminished in radiative regions, AM assume K_{min} to be 10^5 cm^2s^{-1}. Baseline for the variables below the ammonia cloud on Jupiter are $H=L_m=2 \times 10^6$ cm, $K = 2 \times 10^8$ cm^2s^{-1}, and $w_* = 100$ cm s^{-1}.

2.6.3.2 Ackerman and Marley Results

Applying Ackerman and Marley's formulation and using a range of values for the eddy diffusion coefficients, we calculated the water cloud results shown in Figure 2.8. The four panels are the water cloud concentrations at Jupiter with varying enrichments of

water. Each panel shows the cloud concentrations with and without precipitation. The top left panel is for the 0.45 × solar enrichment of oxygen, which is the enrichment factor of oxygen found by the Galileo probe where the maximum cloud density is 1.8×10^{-7} g cm^{-3}. The top right panel is for the solar enrichment of oxygen where the maximum cloud density is 3.7×10^{-7} g cm^{-3}. The next panel is for 4 × solar enrichment. This is in the range of the same enrichment factor that the Galileo probe found for sulfur and nitrogen. It is thought that if the Galileo probe had not gone through an anomalous spot, then this could be the enrichment factor for oxygen also (Wong *et al.*, 2008). The right bottom panel is for 10 × solar O/H. The pre-precipitation cloud concentrations are found to be 3.1×10^{-6} g cm^{-3}. When the lower eddy diffusion is used, $K = 10^5$ cm^2 s^{-1}, for all cases the amount of cloud density was decreased by two orders of magnitude. On the opposite end of the spectrum, when $K > 10^8$ cm^2 s^{-1}, the cloud density only decreases slightly. Table 2.3 summarizes the changes in cloud concentrations associated with each eddy diffusion coefficient and each enrichment factor.

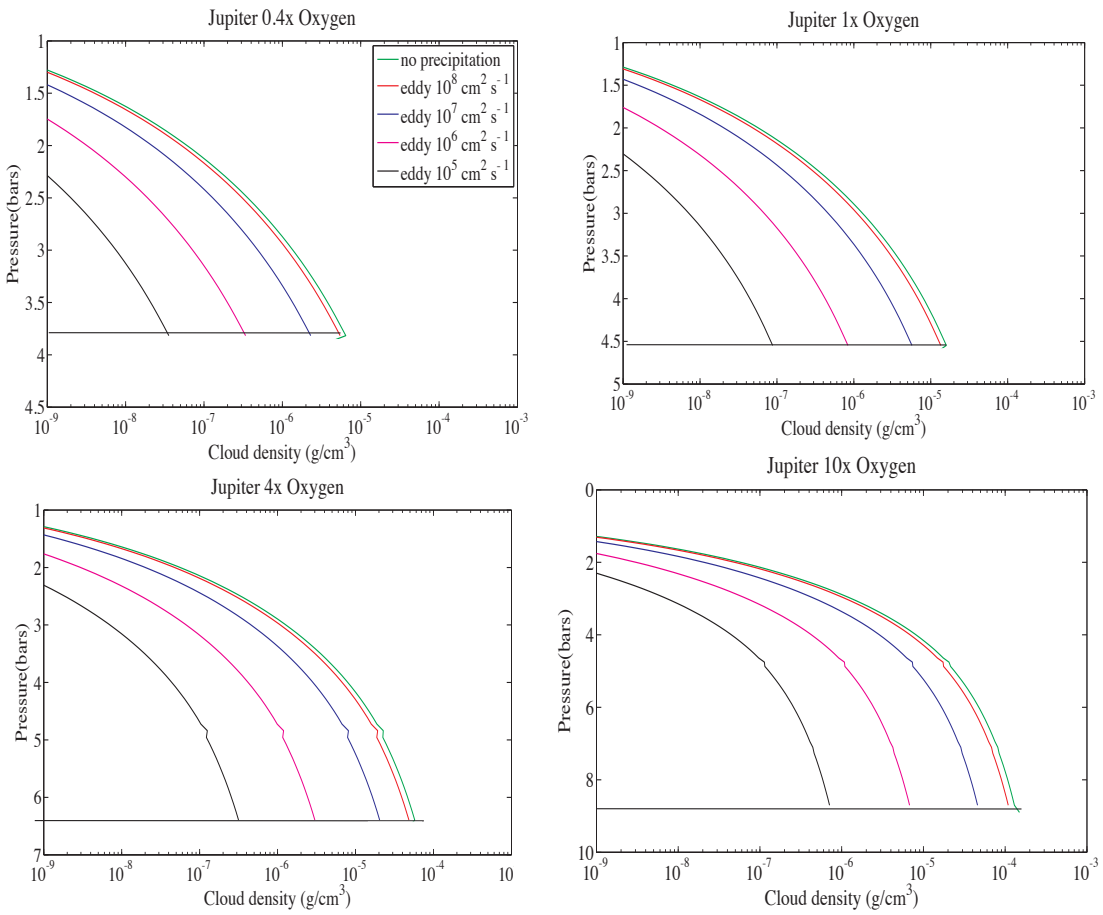

Figure 2.8 The four panels show the effect of precipitation on the ECCM calculated upper limit to cloud concentration (no precipitation curves), assuming four different values of tropospheric eddy diffusion coefficient. Three different cases for the water cloud concentration on Jupiter. The kink seen in the 4 × solar case, and the 10 × solar case on Jupiter, is due to the switch over from liquid water cloud to an ice water cloud. Using Ackerman and Marley (2001), and varying the eddy diffusion coefficient 10^5 to 10^8 cm^2s^{-1}, the cloud densities are found to decrease by a fact of 1.5 to 250.

Table 2.3 The data from figure 2.10 is summarized in this table. It shows how by including precipitation in each of the three enrichment cases the cloud density can be reduced 10-1000 times its original value.

Precipitation results

eddy diffusion (cm^2s^{-1})	10x (gcm^{-3})	4x (gcm^{-3})	1x (gcm^{-3})	0.4x (gcm^{-3})
no rain	1.5×10^{-4}	4.6×10^{-5}	1.1×10^{-5}	3.0×10^{-6}
10^8 cm^2s^{-1}	1.1×10^{-4}	4.8×10^{-5}	1.3×10^{-5}	5.5×10^{-6}
10^7 cm^2s^{-1}	4.6×10^{-5}	2.0×10^{-5}	5.7×10^{-6}	2.3×10^{-6}
10^6 cm^2s^{-1}	6.8×10^{-6}	3.0×10^{-6}	8.4×10^{-7}	3.4×10^{-7}
10^5 cm^2s^{-1}	7.1×10^{-7}	3.2×10^{-7}	8.8×10^{-8}	3.6×10^{-8}

The reduction of the cloud density is found to be highly dependent on the value of the eddy diffusion coefficient, and work needs to be performed to better quantify this value, and thus better understand the effect of cloud precipitation on Jupiter's clouds density. The higher the eddy diffusion the less of an affect the precipitation has on the cloud density as higher eddy diffusion leads to more mixing. Thus, the species would quickly cycle through the atmosphere and back into the clouds. When the eddy diffusion is lower, the species take longer to cycle through the atmosphere. Therefore, if the eddy diffusion is lower than that examined for our study, 10^5 cm^2s^{-1} to 10^8 cm^2s^{-1}, cloud densities will decrease even more. In our calculations, we held the convective velocity constant while Ackerman and Marley calculated this value based off of the eddy diffusion coefficient and the mixing length as seen in equation 2.31. However, this results in eddy diffusion coefficient in equation 2.27 canceling out and the mixing in the atmosphere is not accounted for in their model. To prevent this, we held the convective velocity constant instead and allowed the eddy diffusion coefficient to vary. We chose to keep convective velocity constant as the eddy diffusion coefficient range is better understood

then the mixing length needed to calculate the convective velocity. The other uncertainty in this formulation is the parameter f_{rain}. Changes to this parameter would change the cloud density by less than an order of magnitude as seen in Figure 2.9 while changes to the eddy diffusion coefficient can change the cloud densities by a few orders of magnitude, Figure 2.8. Therefore, changes to the eddy diffusion coefficient have a greater affect on the precipitation and needs to be better understood to accurately quantify precipitation's effect on cloud density. The range given for f_{rain} varies based off of which specie and planet we are on, but the range is smaller than that seen in Figure 2.8. To keep the affect of changing f_{rain} at a minimum the median value in a range was always used to get a better approximation.

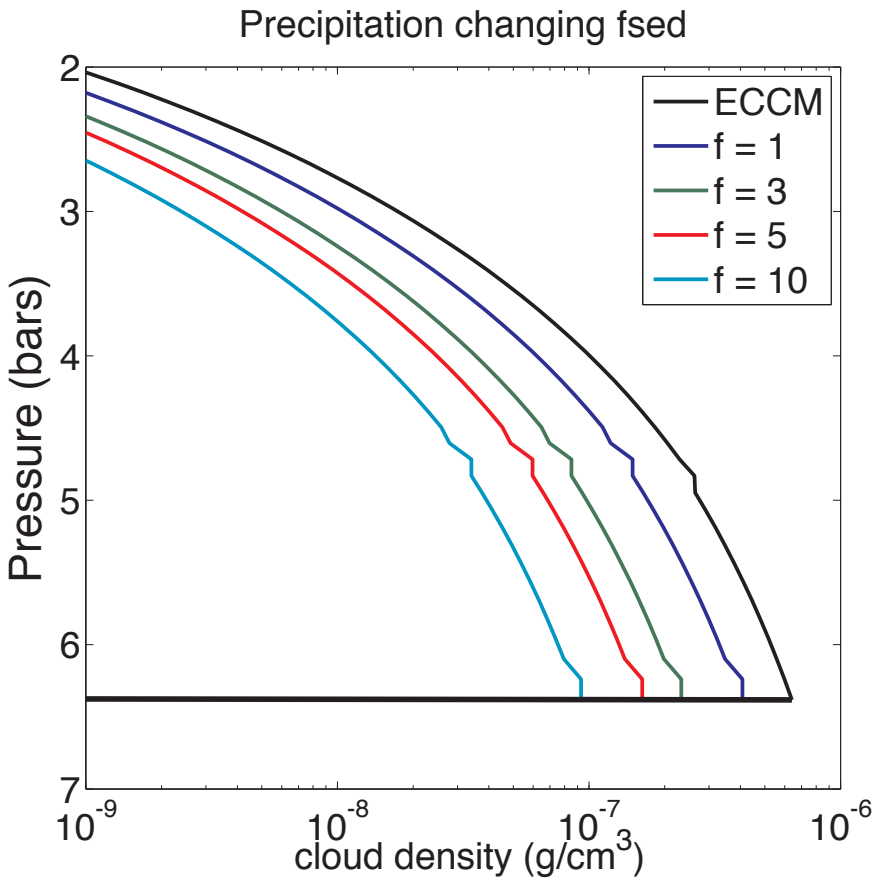

Figure 2.9 The effect of varying the f_{rain} parameter is examined for a case of 4 × solar oxygen at Jupiter with an eddy diffusion coefficient of 10^7 cm^2s^{-1}. The result of changing this parameter is less than an order of magnitude. Therefore, the eddy diffusion coefficient is found to have a more dominate influence on the cloud densities after precipitation.

2.6.3.1 Validation of Cloud Precipitation

To verify that Ackerman and Marley's formulation is correct, the precipitation formulation was applied to an average case for Earth. Earth's atmosphere's composition differs greatly from that of Jupiter. The Earth's atmosphere is 78% nitrogen by volume while Jupiter is mostly hydrogen. Jupiter's clouds are composed of multiple constituents such as water, ammonia, and methane, while on Earth only water clouds are present.

Water vapor can vary on Earth from being as little as tenths of a percent to four percent of the atmosphere near the surface. For our case, we assumed that water vapor was a constant 1% mass of the atmosphere before it is allowed to condense. As the water vapor condenses, it is converted into a cloud. Table 2.4 summarizes the composition of the atmosphere used in our model. These values and the reference temperature and pressure structure values are found in the U.S. Standard atmosphere (United States Committee on Extension to the Standard Atmosphere, 1976).

Table 2.4 The standard Earth Composition used for the Earth simulation, with only 1% water vapor present.

Earth's Composition

	Nitrogen	Oxygen	Argon	Carbon Dioxide	Neon	Helium	Methane	Water vapor
Precentage	.78084	.20946	.00934	.000314	.00001818	00000524	.000002	.01

The terrestrial atmosphere has *in situ* measurements and many simulations that aid in accurately calculating parameters unknown on Jupiter. Many of the variables present in the Ackerman and Marley formulation are already known and measured in the Earth's atmosphere. The convective velocity scale on an average day will vary between 0 and 300 cm s^{-1}. The changes in mixing ratio, q_t, q_c, and q_v, are calculated by the ECCM. Ackerman and Marley found that the value for f_{rain} for cumulus clouds varies between two and six. The higher the value of f_{rain} used the lower the cloud concentration. For our case, we used the median of this range with f_{rain} equaling four as we are only using Earth to validate the methodology not to hypothesize about Earth clouds. The eddy diffusion coefficient remains as the only non-defined value. This value has been calculated in the Earth's troposphere to be on the order of 10^5-10^6 cm^2 s^{-1} (Sutton, 1932; Hunten, 1975).

For our calculations, we used 1×10^5 cm^2 s^{-1} as we are simply trying to approximate the Earth cloud.

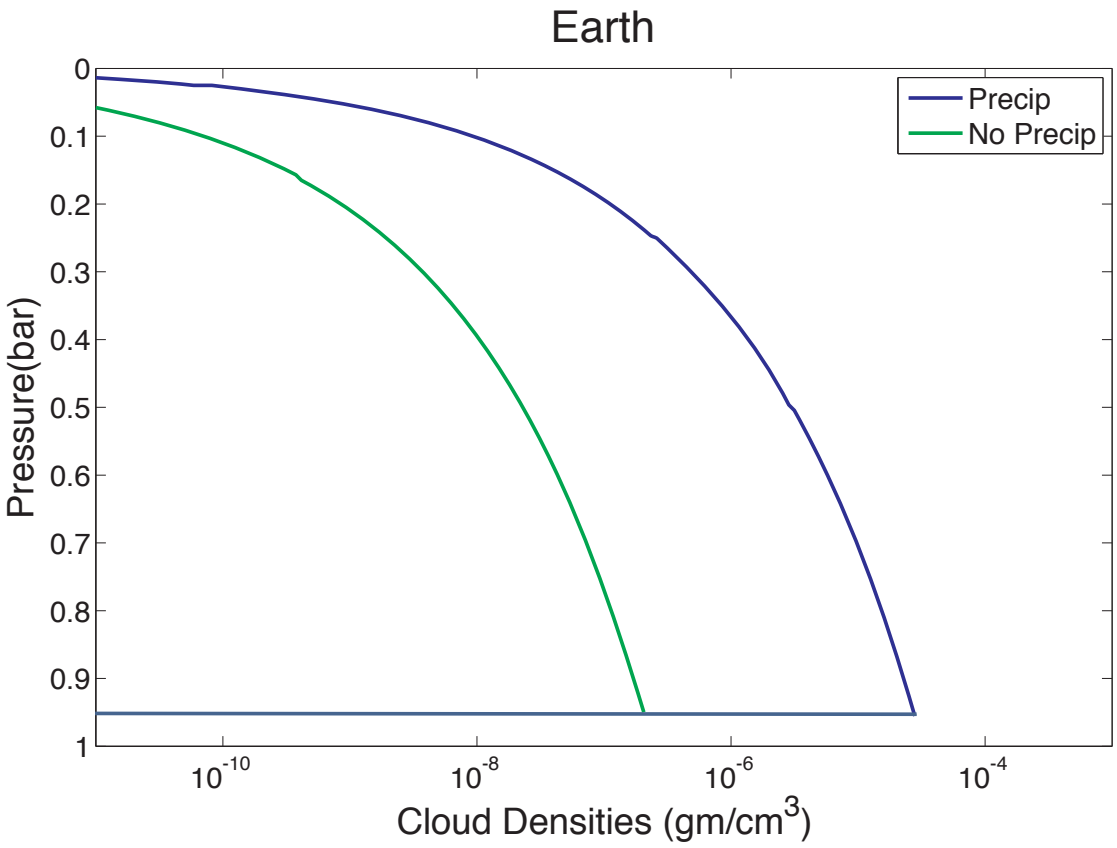

Figure 2.10 The cloud density is displayed before and after applying Ackerman and Marley (2001) precipitation to the ECCM cloud model on Earth.

The cloud density can now be calculated using the ECCM and the Ackerman and Marley formulation. In Figure 2.10, the cloud density without precipitation is compared to the value with precipitation. The cloud density reduction is more than an order of magnitude. This result can be compared to observational data of Earth clouds. Using Earth observing missions such as AIRS, CALIPSO, and CloudSat, the column

abundance of water can be obtained. In our analysis, we used the observations made on October 15, 2006, taken over the Pacific and the South Atlantic oceans. CloudSat 1B CPR standard product (radar backscatter profiles) is combined with a subset of ancillary MODIS radiance and cloud mask data, which overlaps and surrounds each CPR footprint, to produce the 2B GEOPROF CPR data. The particulars of the data products are summarized in Table 2.5. The cloud liquid water content and ice water content profiles are retrieved with associated uncertainties. We selected four main cases for Earth to compare with the Jupiter water cloud. CASE 1 is representative of a cumulus cloud with overlying cirrus cloud layers, while CASE 2 is representative of a cumulonimbus clouds for the dry cold atmosphere at high latitudes. Case 3 and 4 represent stratus clouds in a moist environment. Using these four different observations, the column abundances were estimated to vary between 6.7×10^{-3} to 1.4×10^{-2} g cm^{-2} for mid-latitude clouds.

Table 2.5 CloudSat and Modis data for 2006-10-15. The total precipitation implies total water content, i.e. vapor + liquid + ice. The measured column abundance for ice and liquid are also included.

	Case 1	Case 2	Case 3	Case 4
Latitude/Longitude	52.2°S/161.9°W	67.6°S/151.2°W	1.7°N/8.3°W	2.6°N/176.8°W
Total Precipitable Column (cm)	0.84	0.51	4.56	4.33
Surface Temperature(K)	276.6	261.6	296.3	299.5
Liquid column abundance (gcm^{-2})	2.5×10^{-3}	7.0×10^{-3}	6.8×10^{-2}	1.6×10^{-2}
Ice column abundance (gcm^{-2})	4.2×10^{-3}	7.0×10^{-3}	0.0	0.0

The results from our model can then be used to calculate the column abundance by integrating the cloud model output over the cloud layer. The ECCM results in a

column abundance of 1.3×10^{-1} g cm^{-2}, while the precipitation case has a column abundance of 7.8×10^{-3} g cm^{-2}. The values found using Earth observations along with the values found in our code are summarized in Table 2.6. Table 2.6 shows that when the precipitation of Ackerman and Marley is used on Earth, the ECCM generated column abundances are of the same order of magnitude as observed abundances on Earth for an average cloud. This, therefore, justifies the use of this equation to approximate the effect precipitation will have on the clouds at the giant planets as the Ackerman and Marley modeled value fell within the 6.7×10^{-3} to 6.8×10^{-2} g cm^{-2} range found from observation for an Earth cloud. With the change in cloud density validated, we can now say that precipitation will likely deplete the water cloud density on Jupiter by 1.5 to 300 the original value depending on the eddy diffusion coefficient.

Table 2.6 The comparison of the column abundance for an Earth cloud versus model simulation. By applying the Ackerman and Marley precipitation, the cloud densities are reduced to be within the range of observations

Comparison of Column Abudance

Observations	ECCM	ECCM Precipitation
6.7×10^{-3}-6.8×10^{-2} gcm^{-2}	7.06×10^{0} gcm^{-2}	5.3×10^{-2} gcm^{-2}

2.7 Conclusion

By calculating both the precipitation time scale, the maximum precipitation rate, and the effect that precipitation has on the cloud concentrations, a better estimate of the cloud properties on Jupiter was obtained. The raindrops were found to have a lifetime of approximately 3 hours, 10^4 s, with maximum precipitation rates between 1.19×10^{-4} g cm^{-2} s^{-1} to 8.60×10^{-8} g cm^{-2} s^{-1}. The lifetime of a rain droplet can be compared to the eddy diffusion range of 10^5 cm^2 s^{-1} to 10^8 cm^2 s^{-1} as the eddy diffusion represents mixing in the atmosphere. The precipitation rate was derived to be faster and thus the more dominant of the two processes, which points to the atmosphere having ample time for precipitation to occur.

For the first time, the solution was applied to a water cloud at Jupiter. The overall characterization of precipitation was performed using Ackerman and Marley (2001). Applying the same process to an average atmosphere of Earth, and for the first time comparing the model's column abundances to that of satellite observations to validate the model. The results show that the model's reduction of cloud column density agrees well with the observations. When the solution was applied to Jupiter's water cloud, it reduced the cloud concentration from 1 to 3 orders of magnitude. The range was found by varying the eddy diffusion coefficient, and shows that understanding the turbulence regime is important to understanding how precipitation affects the cloud densities. In order to obtain a more accurate measurement of the decrease in cloud density due to precipitation, measurements of the eddy diffusion values are needed or better measurements in the clouds themselves. In the future, the atmospheric dynamics will need to be considered to obtain a more realistic estimate of cloud properties in Jupiter.

The more turbulence in the atmosphere the shorter the lifespan of a cloud may be. This could also affect the Juno mission search for water, as dynamics are a key player in determining the location of the water in the atmosphere. Precipitation on the giant planets is important when making measurements both *in situ* and remotely. This however, is an evolving field with many unknowns, and even on Earth models have a hard time capturing clouds. Using a combination of precipitation time scale, the maximum precipitation rate, and the effect precipitation has on the cloud concentrations we are able to start to better understand the true nature of the cloud system at the giant planets. In the future, this information can be used to aid in mission planning, and further understanding the amount of each specie present in the atmosphere.

Chapter 3 : THE VLA DATA AND THE PRESENCE OF PHOSPHINE

The presence of phosphine in the ice giants results in the possibility of a type of cloud that is not present in the gas giants. The colder temperatures at similar pressures on the ice giants allow this disequilibrium species to condense. Therefore, phosphine needed to be added to the ECCM calculation of the cloud profile. Phosphine vapor can have an effect on the microwave opacity in the upper troposphere, and needs to be considered when matching the VLA data. Few measurements of the microwave and millimeter-wavelength opacity of phosphine exist for jovian conditions. Pickett *et al.* (1981) measured phosphine's first rotational line at 266.9 GHz. At Saturn, the J = 1-0 rotational transition of phosphine was detected at 11.2 GHz (Weisstein, 2002). The opacity of phosphine was added to the radiative transfer code and the results of this addition are discussed in this Chapter. Understanding the likely hood of a phosphine cloud and the opacity of phosphine gas is important as it may be responsible for some of the observed opacity in the 0.14 to 0.7 cm wavelength range. This could result in less ammonia or hydrogen sulfide being needed in the upper troposphere of the ice giants to

match the radio data. The VLA data can also be used to better constrain the elemental abundance of sulfur, oxygen, nitrogen, and phosphorous.

3.1 Phosphine

Originally, many different types of clouds were hypothesized to exist on the giant planets--NH_4Br, NH_4Cl, NH_4I, and NH_4F (Lewis, 1969). Many of these cloud types are no longer thought to be present. As more was learned about the composition of these atmospheres, a better understanding of the cloud types present was formed. Using observation, it is generally accepted that the likely cloud types at the ice giants are composed of water, ammonia, water-ammonia solution, hydrogen sulfide, ammonia hydrogen sulfide, and methane. Recently, the possibility of another cloud type, phosphine, has been explored further as more vapor pressure measurements in the temperature-pressure regimes located on these planets have been performed. The phosphine vapor pressure measurements, which will be discussed further in Section 3.1.1, show that it can condense in the ice giants.

Phosphine has been detected in the upper troposphere of Jupiter and Saturn for more than 30 years (Bregman *et al.*, 1975; Ridgway *et al.*, 1976; Courtin, 1984; Niemann *et al.*, 1998b; Fletcher *et al.*, 2009a; Fletcher *et al.*, 2009b). This detection points to significant convection in the atmosphere, since phosphine is a short-lived disequilibrium species in the upper troposphere where it is detected. Oxidation of phosphine to produce P_4O_6 is the fastest phosphine-destroying reaction. The observation of phosphine in the upper atmosphere thus indicates that the vertical mixing timescale is shorter than the chemical timescale. Therefore, phosphine is predicted to be well-mixed in the

troposphere. When the Galileo probe entered Jupiter, it found an upper limit of the phosphine abundance of approximately 8 times the solar value at pressures greater than 16 bars (Niemann *et al.*, 1998b). The Jupiter value was refined by Fletcher et al. (2009b) to be 4.8 ± 0.3 × solar using CIRS on Cassini. For Saturn, phosphine was found to be enriched by 5 to 10 × solar (Weisstein and Serabyn, 1994; Weisstein and Serabyn; Atreya *et al.*, 2005), however using CIRS observations Fletcher e*t al.* (2009a) found the deep phosphine to be 14.7 ± 0.3 × solar using recent protosolar values (Asplund *et al.*, 2009). There are no direct measurements of phosphorus in the ice giants, but if the enrichment factors for carbon are applied to phosphorus, then on Uranus it is expected to be enriched between 20-30 × solar (Lindal, 1987).

The presence of phosphine in the atmosphere can have an interesting result in Uranus and Neptune that it does not have in the gas giants. Uranus and Neptune's atmospheres are cold enough for phosphine to condense and form a cloud. If such a cloud exists, it would condense below the methane cloud, which will make it harder to detect. The presence of a phosphine cloud would not significantly change the temperature and pressure profile. On the ice giants, there are no reported tropospheric measurements of phosphine. The VLA data of brightness temperatures can be used to obtain a better approximation of the concentration of phosphine as will be seen later in this Chapter.

3.1.1 Phosphine Vapor Pressure

For a new cloud to be included in the ECCM, knowledge is required of the saturation vapor pressure equation and the concentration of the relevant specie. Then

using the ECCM calculation, the cloud base is found where the species saturation vapor pressure is equal to its partial pressure. While a variety of vapor pressure equations have been derived for PH_3, none encompass the temperature and pressure conditions of the upper tropospheres of the ice giants.

The phosphine cloud on the ice giants forms between 70 K to 100 K based on the concentration of the phosphine. The lowest temperature vapor pressure data that exists is for 91.15 K, which corresponds to a pressure of 1 Pascal (CRC, 1987). The other low temperature data, below ~120 K, comes from two sources, the Handbook of Chemistry and Physics, and the TRCVP Vapor pressure database. The TRCVP database states that while some temperatures are quoted to the tenths place the actual temperatures may be off by a few degrees. The error associated with the Handbook of Chemistry and Physics is less than 25% for low temperatures, and for temperatures above 120 K the error is smaller, between 5-10%. At higher temperatures and pressures other sources provided measurements of the vapor pressure, such as Stephenson & Giauque (1937), and the TRC handbook through Texas A&M. The vapor pressure data available at low temperatures is summarized in Table 3.1 along with the source of the data and the errors associated with each measurement.

Table 3.1 Available phosphine vapor pressure data, source, and uncertainty associated with each point.

Phosphine Vapor Pressure Data

T (°K)	P (Pa)	Error	Reference
91.15	1.00	< 25%	CRC
100.15	10.00	< 25%	CRC
112.15	100.00	< 25%	CRC
115	200.00	< 25%	CRC
120	400.00	< 25%	CRC
125	700.00	< 25%	CRC
128.15	1000.00	< 25%	CRC
130	1300.00	< 25%	CRC
130.51	1333.20	10%	TRC, Texas A&M Univ
135	2300.00	< 25%	CRC
136.48	2666.40	10%	TRC, Texas A&M Univ
140	3900.00	< 25%	CRC
140.15	3906.35	< 25%	ICT
140.25	3999.70	10%	TRC, Texas A&M Univ
140.31	3999.70	3%	TRC, Texas A&M Univ
143.06	5332.90	10%	TRC, Texas A&M Univ
143.75	5332.90	5%	Stull 1947
144.15	5732.86	< 25%	ICT
145	6200.00	< 25%	CRC
145.76	6666.10	3%	TRC, Texas A&M Univ
147.82	7999.30	3%	TRC, Texas A&M Univ
148.15	7999.30	5%	Stull 1947
148.15	8172.66	< 25%	ICT
150	9600.00	< 25%	CRC
150.45	10000.00	< 25%	CRC
151.22	10666.00	3%	TRC, Texas A&M Univ
152.15	11425.73	< 25%	ICT
153.97	13332.00	3%	TRC, Texas A&M Univ

The temperature at which phosphine condensation occurs is 100 K and below, and there is only one measurement below 100 K. To derive the saturation vapor pressure equation appropriate for Uranus, the measurements are extrapolated down to the desired temperatures, 70 K to 100 K, using a Clausius Clapeyron equation to keep the equation physical. One such equation is used by Encrenaz *et al.* (1996), who obtained the saturation vapor pressure of PH_3 from laboratory measurements preformed at temperatures greater than 150 K. Their equation is a first order Clausius Clapeyron equation for the vapor pressure, e_s:

$$\text{Log } e_s = A - B/T \qquad 3.1$$

where a = 4.52 ± 0.14 and b = 834 ± 20 K, and pressure is given in Pascal.

We sought to derive an equation more applicable to the ice giants than that derived by Encrenaz *et al., (1996)*. Additional low temperature data from the Thermodynamic Research Center Vapor Pressure Database and the Handbook of Chemistry and Physics were used along with higher temperature measurements as discussed previously. The order of accuracy was also improved by adding two additional terms to the Clausius Clapeyron equation. This resulted in the third order Clausius Clapeyron equation:

$$Log(e_s) = A + \frac{B}{T} + C * \log(T) + D * T \qquad 3.2$$

where the coefficients are A = 11.35, B = -968.35 K, C = -0.00175, and D = -0.00604 K^{-1}, where T is in Kelvin and pressure is given in units of Pascal. The results of this equation are compared to that of the Encrenaz *et al.* equation in Figure 3.1. This figure also contains the data, red dots, for comparison to the green line, which is our fit, and the blue line, which is the fit from the Encrenaz equation. The two fits are very similar at higher pressures, but start to deviate from one another at lower pressures.

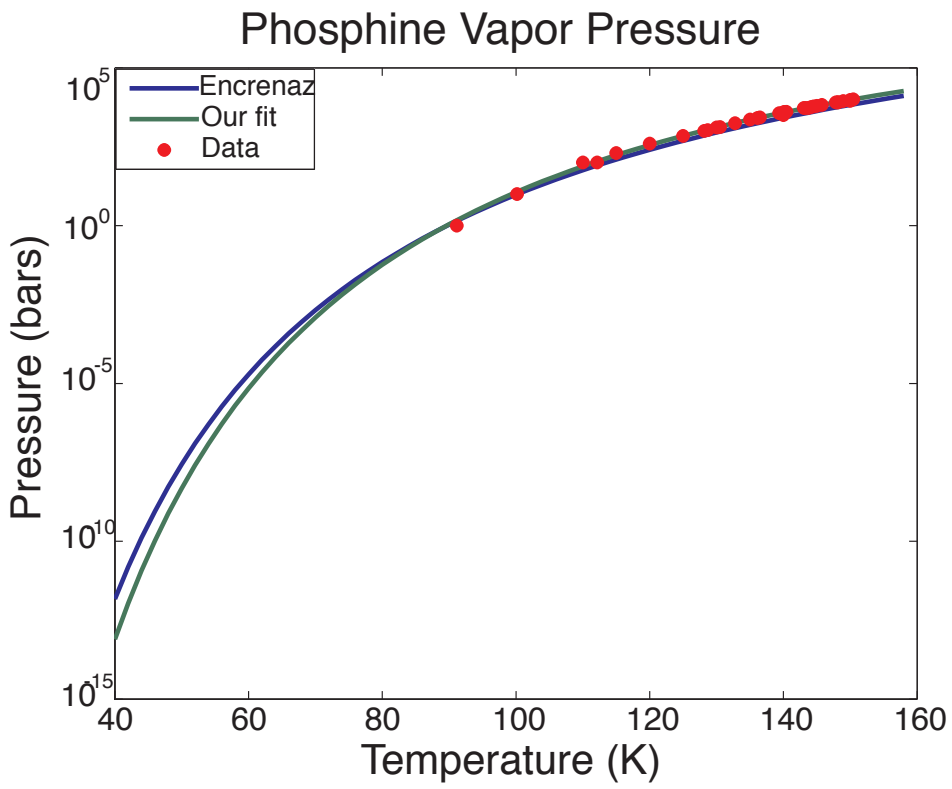

Figure 3.1 A comparison between the data, the Encrenaz vapor pressure equation, and our new vapor pressure equation for phosphine. The Encrenaz equation was derived with data from only 150 K above while our fit was derived using lower temperature/pressure data.

To perform further analysis of how these two equations compare to the data, the chi-square distribution error was used, and is calculated using:

$$\sum_{i=1}^{k}\left(\frac{X_i-\mu_i}{\sigma_i}\right)^2 \qquad 3.3$$

where X is the data, μ is the model vapor pressure, and σ is the measurement error. The number of data points is k. The degree of freedom is equal to k-1. At each point the chi-square error is calculated and then summed; these values can be seen in Table 3.2. The total chi-square error of our new equation is 11.4. The chi-square value for the previous equation is 116.9. The p-value for our equation is .025, which makes our equation

statistically significant. For the case of the previous equation, the p value was found to be 1, and thus is not statistically significant. There is one data point with a particularly bad fit for the previous equation that results in a chi square error for that one point of 78.4. If this point is ignored, the previous equation chi-square error drops to 38.5. The resulting p value is found to be 0.99, resulting in the previous equation still not being statistically significant. Therefore, our fit is an improvement over that of the previous equation, and will be used to calculate the phosphine cloud on Uranus and Neptune.

Table 3.2 Chi-square error for our vapor pressure equation, and the Encrenaz equation. The first column contains the actual pressure values from measurements; the second column is the error range, which was used to calculate the chi-square error.

Error associated with the our equation and Encrenaz's equation

Pressure (Pa)	Error (Pa)	Encrenaz	chi square	Our fit	chi square
1	2	1.4152	0.0431	1.4871	0.0593
10	4	9.8354	0.0017	11.8194	0.2069
100	25	57.0642	2.9496	75.6564	0.9482
100	25	80.3893	0.6153	108.2951	0.1101
200	50	124.1404	2.3019	170.3566	0.3515
400	100	253.1240	2.1573	356.4332	0.1898
700	24	487.5285	78.3752	699.0857	0.0015
1000	100	717.6860	7.9701	1037.3045	0.1392
1300	65	1272.3758	0.1806	1294.9543	0.0060
1333.2	133.32	1347.9851	0.0123	1374.9258	0.0980
2300	115	2198.9848	0.7716	2279.8641	0.0307
2666.4	266.64	2565.7512	0.1425	2671.4414	0.0004
3900	195	3654.7455	1.5818	3835.8230	0.1083
3489.3	174.465	3654.7455	0.8993	3835.8230	3.9450
3999.7	399.97	3745.2079	0.4048	3932.5712	0.0282
3999.7	119.991	3767.2012	3.7544	3956.0920	0.1321
5332.9	159.987	5021.7378	3.7827	5296.8163	0.0509
5332.9	533.29	4900.9267	0.6561	5167.8178	0.0958
5332.9	106.658	5227.1007	0.9840	5516.0267	2.9479
6200	310	5865.1060	1.1671	6196.4328	0.0001
6666.1	199.983	6284.4264	3.6425	6643.0610	0.0133
7999.3	239.979	7550.9740	3.4901	7989.0931	0.0018
9600	480	9120.1084	0.9995	9649.9525	0.0108
9018.3	450.915	9120.1084	0.0510	9649.9525	1.9623

3.1.2 Phosphine Cloud

Using the vapor pressure equation formulated above, as well as the previous equation, the phosphine cloud can now be calculated. The two fits appear to be very similar at the higher temperatures, but start to deviate from one another at lower temperatures. Our fit results in higher temperatures at lower pressures than the previous equation. The cloud base of the phosphine cloud was calculated, and it was found that our equation results in only a 0.1 bar deeper cloud than a cloud base calculated with the previous equation. The densities at the cloud base were also found to be comparable. For these clouds, the concentration varies from 10^{-6} to 10^{-8} gcm^{-3}. This shows that even with depleted amounts of phosphine a cloud is possible. The new equation does not show a significant change over the previous equation. However, it was calculated using lower temperature measurements than previous equations, and therefore will be used for this study. Figure 3.2 displays the cloud profiles in each case. The presence of the phosphine cloud and how its opacity contributes to the VLA data will be further discussed in Section 3.7.

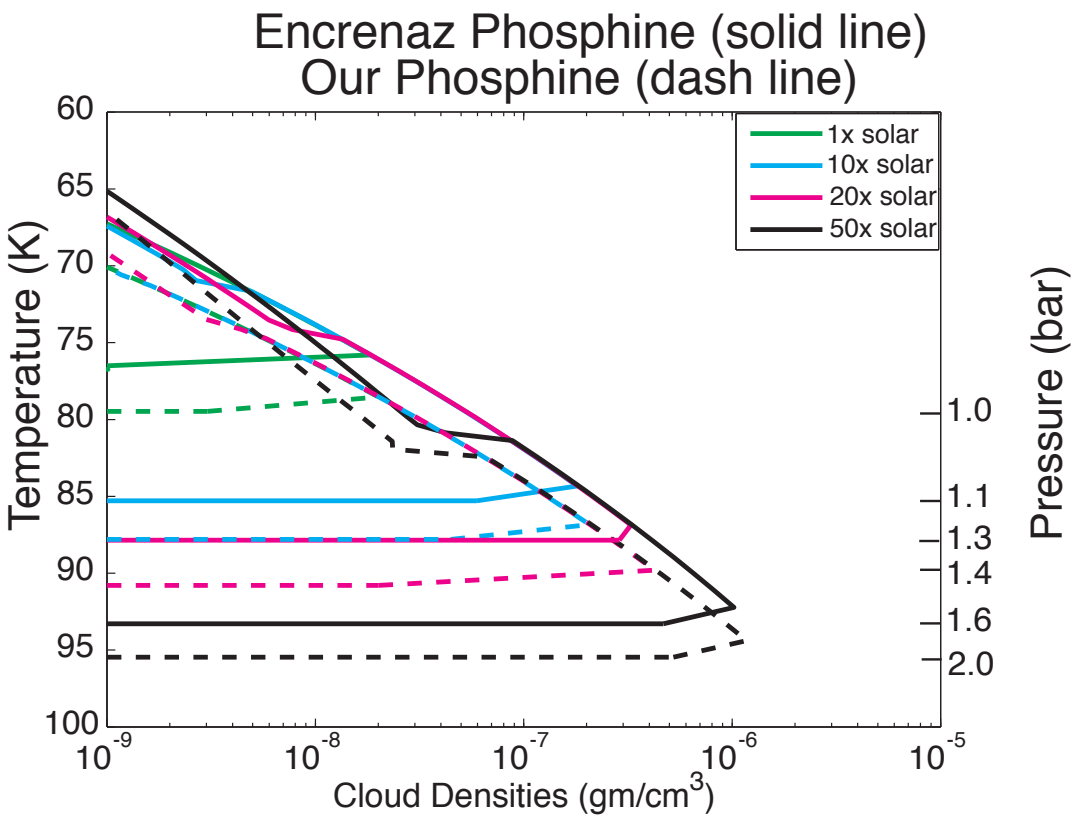

Figure 3.2 Phosphine cloud at different enrichment factors using our vapor pressure equation and the Encrenaz's vapor pressure equation for the 1x, 10x, 20x, and 50x solar cases. These cases represent an upper limit, as the addition of precipitation, as seen in chapter 2, will reduce the cloud concentrations. The phosphine cloud densities are significantly less than the other cloud densities, such as methane and hydrogen sulfide, and the aerosols are not expected to have an effect on the atmospheric structure.

3.2 Basic Radiative Transfer Definitions

The brightness temperature at radio wavelengths is measured by the VLA will be used to examine the upper troposphere of Uranus and examine the possibility of a phosphine cloud. To understand the brightness temperatures, it is first necessary to discuss other radiative transfer principles. Uranus is studied on Earth by measuring the light that it emits. The light that is transmitted from Uranus to Earth is not the same light that was emitted directly from Uranus. The clouds and the atmosphere can scatter the

light. The only way to see the light non-scattered is to look directly at the source. Scattering occurs at all wavelengths and describes how light interacts with the matter it is traveling through. In scattering, a particle that is in the pathway of a wave extracts energy from the incident wave and then reradiates the energy in all directions. The size range of particles in the atmosphere that are responsible for the scattering of light varies from small gas particles and aerosols, to larger water droplets and hail. Scattering directions differ based on the size of the scattering particle. Smaller particles scatter light equally in the forward and backward direction, with backwards being back towards the light source. As the particle increases in size, the energy starts scattering more in the forward direction. Scattering often happens more than once during a photon's journey.

Absorption and scattering are related as they both remove energy from a wave traveling through a medium. Often times, both processes are needed to explain an observed light phenomenon. For example, the grass is green because it scatters green light while it absorbs red and blue light. The combination of scattering and absorption is called extinction, which is defined as how a beam of light is attenuated. Transmittance is equal to one minus the absorption, a_s, as what is not absorbed is transmitted. The absorption and transmittance, t, in a layer of the atmosphere between two levels, z_1 and z_2, are related by:

$$a_s(z_1,z_2) = [1 - t(z_1)] - [1 - t(z_2)] = t(z_2) - t(z_1) \qquad 3.4$$

The absorption per unit altitude, W(z), also known as the weighting function, is defined:

$$W(z) = \lim_{\Delta z \to 0}\left[\frac{a_s(z,z+\Delta z)}{\Delta z} = \frac{t(z+\Delta z) - t(z)}{\Delta z}\right] = \frac{dt(z)}{dz} \qquad 3.5$$

where $\Delta z = z_2 - z_1$. The weighting function defines how a wavelength is absorbed over an altitude range. Each atmospheric species absorption can be examined at each wavelength

using the weighting function. The weighting function of these species will be used in section 3.6. to aid in the matching of the VLA data to a radiative transfer model.

The presence of clouds complicates radiative transfer calculations. On Earth, 50% of the sky is covered with clouds. These clouds can keep radiation out as well as keep radiation in, which results in them being a lead player in the calculation of Earth's radiation budget. For Uranus, they are also important in the calculation of the radiation budget. Optical depth is defined as a measure of the transparency of the atmosphere and expresses the quantity of light left after the light has been removed by scattering and absorption when traveling through a medium, such as a cloud. Taking I_0 to be the intensity radiated from the source, and I as the observed radiation after it has passed through a medium, the optical depth, τ, can be represented with the following equation as a function of wavelength:

$$\frac{I}{I_0} = e^{-\tau} \qquad 3.6$$

Optical depth also relates to the transmissivity as it is used to describe the amount of light that passes through a medium, $t = e^{-\tau}$.

To derive the brightness temperature, it is necessary to build off of other radiative transfer principals, such as flux density, monochromatic intensity, black bodies, and the Planck function. The flux density is defined as the rate at which energy passes through a unit area. In order to derive this quantity, the monochromatic intensity first needs to be defined. The monochromatic intensity, I_ν, is the energy transferred by electromagnetic radiation in a specific direction passing through a unit area per unit time at a specific wavelength. This intensity is easier to understand in terms of its units of watts per square

meter per unit arc of solid angle, Ω, per unit wavelength, or frequency, in the electromagnetic spectrum, θ is the zenith angle, and is defined as:

$$I_v = \frac{dE_v}{\cos\theta d\Omega dt dA dv} \qquad 3.7$$

The monochromatic flux, F_v, is the radiant energy per unit time per unit frequency per unit area along the direction perpendicular to the given area. In other words, the flux is described in units of $Wm^{-2}cm^{-1}$ and is defined as:

$$F_v = \frac{dE_v}{dt dA dv} = \int_{\Omega} I_v \cos\theta d\Omega \qquad 3.8$$

Letting $\mu = \cos\theta$, and given that the change in the solid angle is defined as:

$$d\Omega = \sin\theta d\theta d\phi \qquad 3.9$$

The flux density is then defined as:

$$F_v = \int_0^{2\pi} d\phi \int_0^{\pi} I_v(\theta,\phi)\sin\theta\cos\theta d\theta = \int_0^{2\pi} d\phi \int_{-1}^{1} I_v(\mu,\phi)\mu d\mu \qquad 3.10$$

This quantity is essential to understanding both radio telescope data and radiative transfer models. Flux and intensity measurements are used to categorize the strength of an electromagnetic radiation field; however, the flux does not indicate in what direction the radiation originated.

A black body is an idealized body that absorbs all of the incident electromagnetic radiation. A black body is the best emitter of thermal radiation as it is a perfect absorber. A number of different equations can approximate black bodies such as the Wien's displacement law which shows that by knowing the shape of a spectrum at one temperature allows the calculation of the spectrum at any temperature:

$$\lambda_{max} = \frac{b_W}{T} \qquad 3.11$$

where λ_{max} is the wavelength at which the intensity is at a maximum, b_w is the Wien's displacement constant, 2.898 × 10^{-3} Km. This hold true as long as $h\nu >> KT$. This intensity decreases exponentially at high frequencies. The Planck's function describes the blackbody radiation at a temperature. The Planck's blackbody radiation or Planck's function is calculated using:

$$B_\upsilon(T) = \frac{2h\upsilon^3}{c^2}\frac{1}{e^{\frac{h\upsilon}{kT}} - 1} \qquad 3.12$$

where B_v is the amount of energy emitted in a given frequency v, and h is the Planck constant. The Planck function can also be defined in terms of wavelength.

The Planck function describes the amount of radiation that is being emitted, and is used to calculate the brightness temperature. The brightness temperature, T_B, is the inverse of the Planck function and is found using the Rayleigh-Jeans limit of equation 3.12 and solving for T:

$$T_B = \frac{c^2 I_v}{2v^2 k} = \frac{\lambda^2 I_v}{2k} \qquad 3.13$$

Brightness temperature is commonly used at radio wavelengths, but it basically is just a brightness measurement. In cases when the emissivity is close to one, such as it is with water and land on Earth, the brightness temperature will be close to the physical temperature. When the emissivity is less than one, the brightness temperature can be significantly different than the physical temperature. The brightness temperature a common unit for VLA data and will be further discussed in section 3.4.2.

3.3 Why Radio Telescopes?

There are advantages to using radio waves to study Uranus. One such advantage is that radio waves reach the Earth's surface. This allows ground-based telescopes to be used. The opacity of Earth's atmosphere creates a spectrum as seen in Figure 3.3. The atmosphere readily absorbs certain wavelengths while other wavelengths penetrate through the atmosphere, called atmospheric windows. The radio wavelength region is one such window. Gamma rays, x-rays, and ultraviolet radiation are blocked by Earth's atmosphere; therefore, any measurement in these wavelength regions needs to be performed from space. In the visible spectrum, some observations can be performed from the surface, but the atmosphere often times distorts the signal. Long-wavelength radio waves are also blocked due to the ionosphere reflecting their radiation. Therefore, shorter wavelength radio waves are ideal for ground-based observations.

Another advantage of using radio telescopes is that radio waves can probe deep in the atmosphere of Uranus. Due to the absorption properties of different species in the atmosphere, different radio wavelengths can penetrate to different depths in the atmosphere allowing data from deeper in the troposphere to be observed. The visible wavelength, on the other hand, probes only the stratosphere. The energy that radio waves produce is in the form of low-energy photons, which are easy to produce and are sensitive to many emission parameters. Spectral parameters such as peak brightness and frequency can help determine the emission mechanism, and more information about the body being observed.

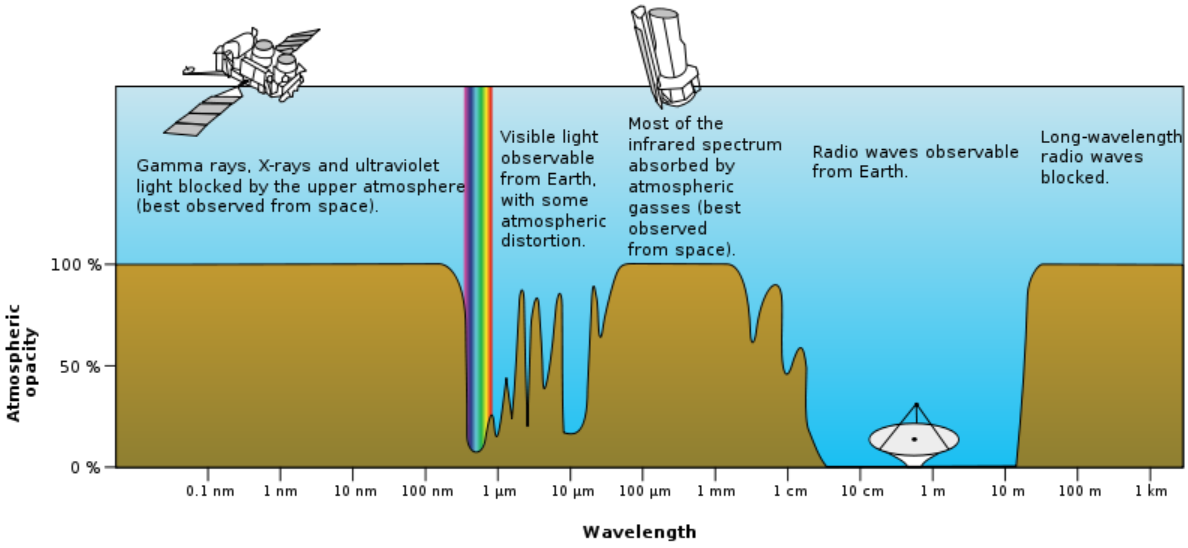

Figure 3.3 Earth's atmosphere opacity, and windows from http://jersey.uoregon.edu. The radio wavelength band an atmospheric window, which allows for ground base observation of radio waves from celestial bodies.

3.4 VLA

In Chapter 1, the history of the radio telescope was discussed along with a brief description of the VLA. The VLA is a radio telescope and works by receiving electromagnetic waves emitted from a body. Just as is true at visible wavelength, the bigger the telescope, the higher the spatial resolution of the data. The VLA is not a single telescope; it is an interferometer, which simply stated is a series of radio telescopes. Each radio antenna in an interferometer works in a pair with every other antenna in the interferometer. Every pair will observe the same body. The distance between two telescopes is known as the baseline. The baseline determines the resolution of the data. When two telescopes are close to each other, the part of the sky they observe is similar, and thus they output large swaths of low-resolution data. However, when the telescopes

are farther apart they only see a small part of the same sky but at a higher resolution. The location of a body in the sky with respect to the telescopes needs to be considered. When the body is directly overhead of the telescopes, the signal will reach both antennas at the same moment in time. However, when the body deviates from the zenith angle, the signal will arrive at each telescope at different times. In this case, the signals can arrive in or out of phase with each other. This can lead to constructive or destructive interference. Using the baseline, it is possible to determine the additional time it takes for the signal to reach an antenna. Basic geometry is used to determine the difference in path lengths and is illustrated in Figure 3.4.

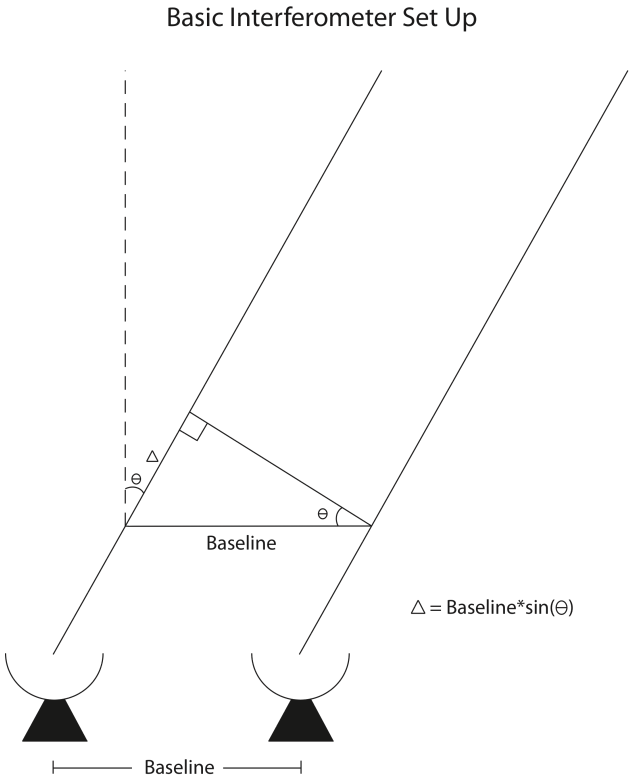

Figure 3.4 The basic set up of an interferometer. The distance between two antennas is the baseline. The geometry for calculating the baseline is shown. When the baseline is small, the resolution is poor as the two antennas are seeing the same sky. When the baseline is larger, the resolution is higher as the two antennas are seeing little of the same sky.

The VLA is located on the plains of San Agustin in Southwestern New Mexico. The location was chosen because of its high elevation, which results in a thinner atmosphere to distort the signal, and its remote location, which reduces ground-based contaminators. The antennas can be arranged in four basic arrangements, A, B, C, and D. The A configuration has the highest spatial resolution (antennas farthest apart), making it ideal for small objects, while the D configuration has the lowest resolution (antennas close together) making it ideal for observing close objects large objects.

3.4.1 VLA Performance Constraints

The performance of the VLA depends on many different parameters including aliasing, time lag, and antenna cross talk. Certain radio bands are reserved for the study of radio astronomy; therefore, human-caused contamination should not be an issue. Based on the size of the structure being observed, data can be lost due to aliasing, when the structures are larger then what is viewable. Therefore, the proper alignment of the telescopes is needed to correspond to the size of the object. Time resolution needs to be considered you are viewing an object in multiple wavelength bands, as there is a time lag between when the data is obtained in each band. During that time, the Earth rotates and moves, as does the object being observed. In the case of Uranus, not only will it move in the night sky, thus changing the baseline, but Uranus also rotates on its axis changing what part of the planet is being observed. Therefore, in many cases a disk average value is taken as opposed to resolving the disk at multiple points. Another important concept to be considered is how the antennas talk to each other. Cross-talk occurs when one signal is picked up by an adjacent antenna and can cause erroneous correlations in data. This

affects all data observed in the 400 cm wavelength-band and data observed in the 20 cm in the D-configuration. Conditions at the VLA, therefore, need to be considered.

The Earth's atmosphere also leads to complications in understanding the data, especially the clouds, wind, and atmospheric stability. The density of the air changes, which can distort the signal. The clouds in Earth's atmosphere can increase the noise in the system, especially if they are composed of large suspended droplets. Moderate winds also have an affect on the ability to orient the antennas precisely. Some bands can only make observations when winds are below 15 mph while others can conduct measurements with winds up to 45 mph. Finally, the accuracy at which an object position can be determined is limited by the atmospheric stability. Therefore, a understanding of the meteorological conditions at the time of observation is desirable.

3.4.2 VLA Observations

The VLA antennas measure the incoming signal from a body. As the VLA is an interferometer, it cross-correlates the signals from two antennas observing the same source. By using the two antennas, the data provided is more complicated than that from a single antenna. Not only do we obtain the intensity of all sources in the beam of an antenna, but we also obtain the position in the sky. The parameters measured by VLA are the visibilities (u,v) and the baselines (u,v) and are obtained by knowing the locations of the antennas with respect to each other. The baselines, which were explained in section 3.4, are characterized by their east-west (u) and north-south (v). If all 27 VLA antennas are in use, 351 baselines are obtained, and the u-v coverage is made up of 351 points at any given point in time.

The visibilities are a measure of the amplitude and phase on each baseline. The antennas that intercept the signals serve two main purposes. They intercept the radiation, and they restrict the field of view. The radiation collected is expressed in terms of the effective area of the telescope. Associated with this is the beam pattern, which is the Fourier transformation of the aperture. By taking the Fourier transformation, we are converting something that is in time to frequency. A Fourier transformation is performed using the following equation:

$$F(l,m) = \iint f(u,v)e^{2\pi(ul+vm)}dudv \qquad 3.14$$

where u, and v are in units of wavelength, f(u,v) is the brightness distribution in the aperture, and F is the complex far-field brightness pattern with l and m being the angular distance on the sky. A Fourier transformation can be used to demonstrate the relationship between the sky brightness distribution and a complex visibility. By using the inverse Fourier transformation on a visibility, the sky's brightness can be obtained.

After applying a Fourier transformation, the data is fit to a Bessel function, which is then used to calculate the intensity from the Planck's function, as seen Section 3.2. A Bessel function is defined as:

$$x^2\frac{d^2y}{dx^2} + x\frac{dy}{dx} + (x^2 - \alpha^2)y = 0 \qquad 3.15$$

where α is the order of the Bessel function. It is necessary to use a Bessel function when working in cylindrical or spherical coordinates, as it eliminates the problem of separate solutions to the Laplace and Helmholtz equation. In our case, the Bessel function represents the power pattern of the beam of each antenna.

To make sure the data is accurate, a calibrator is also used. A calibrator is an object that has a known emitted flux. Knowing the calibrator's flux density is important

as the information that is being extracted from the planet's flux density is directly related to the physical temperature and materials being observed in the planet. The ideal calibrator is an unresolved point source, whose visibility amplitude will be the same for all baselines (Figure 3.5). The flux from Uranus, which was resolved in each of our data sets, will be a Bessel function. The shortest baselines are observing most of the flux, but do not resolve the planets. The longer baselines, obtain less flux as they are observing only part of the flux. As the baselines get longer, eventually baselines with zero flux are found, and this is due to the interferometer having both a positive and negative response functions on the sky (Figure 3.6). Fitting a Bessel function to the visibilities allows one to estimate the flux emitted from Uranus. In Figure 3.5 the calibrator quasar 2246-121 is displayed, as well as, the Uranus data, which was multiplied by 10 to make it more visible in the figure. The Bessel function and the flat line of the calibrator can be seen as expected. Figure 3.6 shows the dependency of a baseline on flux density and resolution.

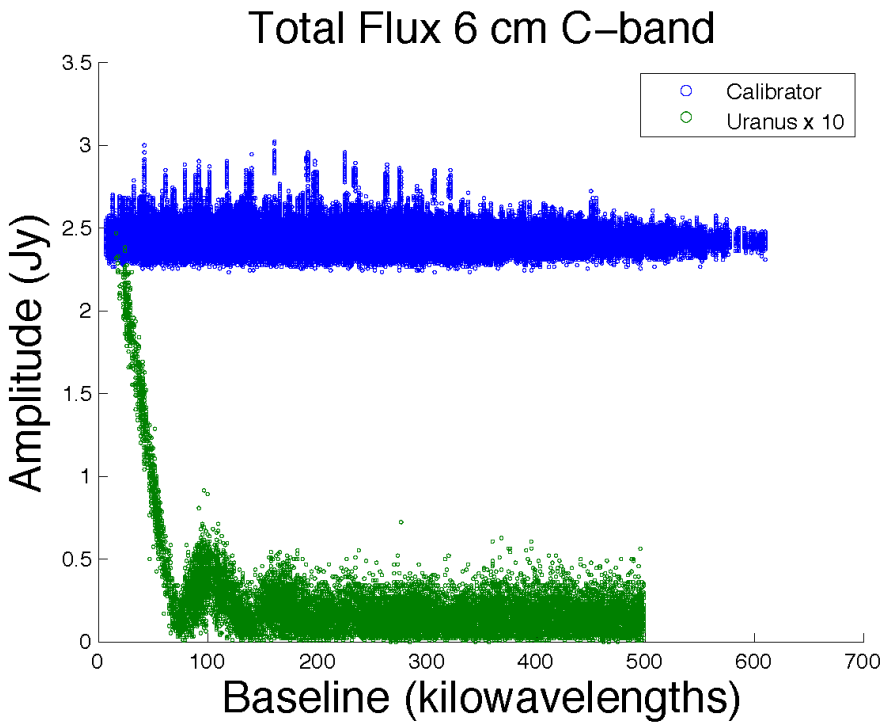

Figure 3.5 The total flux in the 6 cm wavelength. The calibrator used was quasar 2246-121. The Uranus 6 cm data is from 2006, and was multiplied by 10 to show the features. Note the calibrator is a flat line while the Uranus flux is a Bessel function, which signifies a resolved disk.

The total flux density of the planet is constructed using the visibilities. To form these images, the data is self-calibrated as well as calibrated using a calibrator as was just discussed. In order to self-calibrate the body needs to have sufficient flux densities, which most major and minor planets contain. The images are then obtained using a four part process. First, an initial model is obtained. The complexity of this initial model is based on the sensitivity in the data. Next, deconvolution is performed using the initial model to produce an image. The image is then self-calibrated to account for short timescale

variations in the atmosphere. Finally, the process is repeated until a convergence is reached.

From the flux density the disk temperature is calculated using the Rayleigh-Jeans function. This temperature has a number of adjustments and corrections including an adjustment for the cosmic microwave background emission. The flux density per beam is converted to the average brightness temperature per beam using:

$$T_B(l,m) = F(l,m)\frac{\lambda^2}{2k_b}\frac{4\ln 2}{\pi B} + T_{cmb} \qquad 3.16$$

where l and m indicate position in sky, B is the diameter of the Gaussian convolving kernel, and T_{cmb} is the cosmic microwave background temperature, approximately 2.7K (Butler and Bastian, 1999). The results of the brightness temperatures calculations used for this study are in Table 3.3 and will be used for fitting the VLA data in Section 3.9.

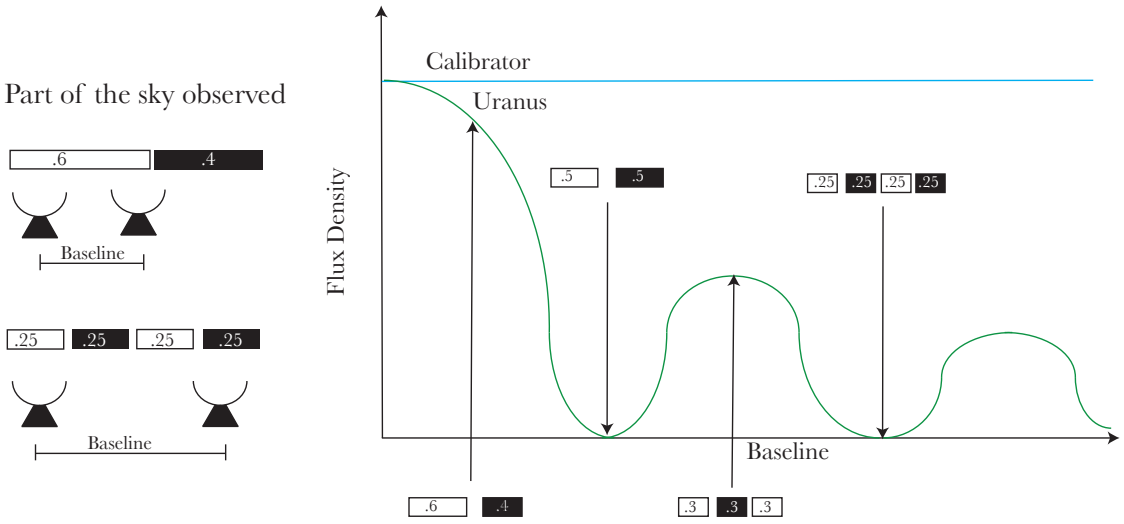

Figure 3.6 The shorter the baseline, the more flux density reaches the antennas, but the poorer the resolution. As the baselines get larger the flux density is less, but there is higher resolution.

3.5 VLA Data

Disk-averaged microwave measurements of Uranus have been taken since 1965. The earliest measurements pre-date the VLA (Kellermann, 1966; Klein and Seling, 1966) and were taken with single–dish telescopes. These data were disk integrated and had no spatial resolution. When measurements were taken in the mid 1970's, it was seen that the average microwave brightness was increasing with time (Klein and Turegano, 1978; Gulkis *et al.*, 1983). Due to the lack of spatial resolution, it was difficult to determine if these changes were true temporal variations, perhaps driven by seasonal effects, or if they were related to the changing viewing geometry, which caused the latitudes observed to change over time.

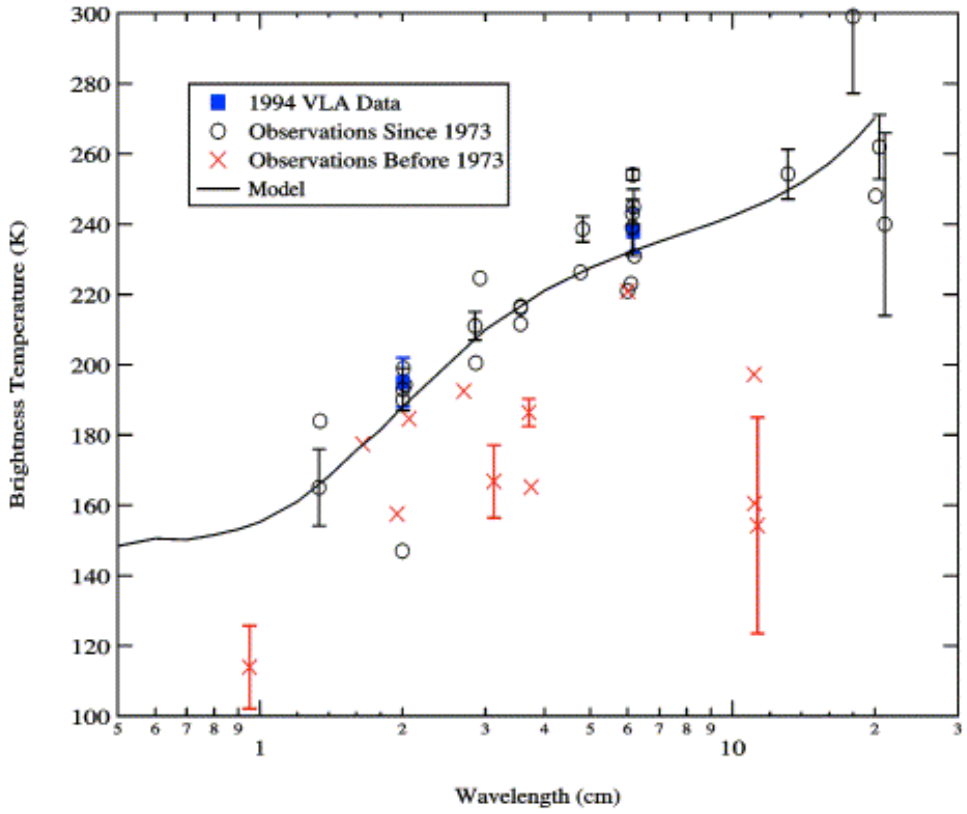

Figure 3.7 Brightness temperature measurements performed at Uranus from Hofstadter and Butler 2003. The model fit show here was preformed prior to the addition of phosphine in the radiative transfer model.

In the early 1980's the VLA was being constructed, and the first maps of Uranus were made (Briggs and Andrew, 1980). These measurements were executed with a partially completed VLA and were only able to obtain measurements in the 6 cm band. Further measurements were made (Jaffe *et al.*, 1984; Berge *et al.*, 1988; de Pater and Gulkis) and all of them showed the south pole was brighter than lower latitudes. Over the time period of 1989 to 1994, the VLA showed an increase in the equator-to-pole brightness contrast suggesting seasonal changes (Hofstadter and Butler, 2003). Figure 3.7, summarizes the brightness temperature observations made.

The VLA measurements analyzed in this study were acquired at 4 wavelengths – 0.7, 2.0, 6.0, and 21.2 cm - during Uranus' transition from winter to spring in the Northern Hemisphere, 2005-2009, as summarized in Table 3.3. All the observations were analyzed in a similar fashion using the AIPS data reduction package (http://www.cv.nrao.edu/aips/). After discarding measurements, which obviously suffered from instrumental effects or radio-frequency interference, the absolute flux scale was set relative to 3C286, one of the flux standards for the VLA. To maximize sensitivity, upper and lower sidebands of the continuum signal were calibrated separately, but then averaged together. Table 3.3 indicates the average wavelength and flux for the two passbands. Observations of an unresolved secondary calibrator (quasar 2323-032 for the 21 cm data, 2246-121 for all others) were used to remove long timescale (10's of minutes) atmospheric and system fluctuations in the data. The total flux from Uranus was determined in each data set both by fitting a limb-darkened disk to the raw visibility data, and by creating an image of the sky brightness pattern as described in Hofstadter and Butler (2003). Differences between the two techniques are negligible. We also used one measurement from the SMA observatory at a wavelength of 0.14 cm, which was made in 2006. The SMA is an eight element mm/submm interferometer located near the summit of Mauna Kea, Hawaii. The primary flux calibration was determined by referencing to simultaneous observations of Neptune, for which a Planck disk average temperature of 93.9 K was assumed (Griffin & Orton, 1993). The SMA data were analyzed in a fashion similar to the VLA data.

The radio data can be used to image the planet, but we do not report those results in this paper. Here we will make use of the disk-averaged brightness as given in Table 3.3. Figure 3.8 shows the weighting functions at each of our wavelengths, indicating the

region of the atmosphere to which each measurement is sensitive. The errors bars at all wavelengths, except for 21.2 cm, are predominantly due to uncertainties in the absolute calibration of the instrument, which results in roughly a 5% error. For the 21.2 cm data point, the error bar also includes uncertainty due to possible contamination from background sources, which is why the uncertainties associated with this point are the greatest. (The thermal emission from Uranus, described by Planck's Law, decreases as one moves to longer wavelengths, while the non-thermal emission from background galaxies grows larger.)

Table 3.3 Data from the VLA used in simulations. This data comes from 2005-2009. The wavelength, brightness temperature, error and observatory used for the measurement are included (Mihalka *et al.* in prep).

Observing Date	Wavelength (cm)	Flux Calibrator and Flux (Jy)	Uranus Planck Brightness (K)	Error (K)	Observatory
11 July 2006	0.14	Neptune / 13.2*	94.5	4.5	SMA
21 June 2005	0.69	3C286 / 1.455	147.1	7	VLA
21 April 2006	2.01	3C286 / 3.456	175.4	9	VLA
7 May 2006	6.17	3C286 / 7.486	221.0	11	VLA
5 January 2009	21.22	3C286 / 14.768	260.6	26	VLA

*Corresponding to a Planck brightness temperature of 93.9 K for a distance of 29.17 AU and polar/equatorial radii of 24766.0 / 24342.0 km.

3.6 Phosphine Opacity

Hofstadter and Butler (2003) radiative transfer model contains the opacity calculations for many of the condensable species in the Uranian atmosphere including water, methane, hydrogen sulfide, and ammonia. However, with the current clouds it is difficult for the model to match the observations. A possible solution to this problem is the presence of a 'new' condensable cloud species or for there to be multiple layers of clouds. The ice giants are colder than the gas giants in their upper troposphere allowing for the condensation of phosphine. Phosphine has previously been suggested to have a significant contribution to the microwave opacity of Neptune (Hoffman *et al.*, 1999). This led Hoffman *et al.* (2001) to conduct laboratory measurements of the absorption properties of phosphine in a hydrogen-helium atmosphere at frequencies of 1.5 GHz, 2.2 GHz, 8.3 GHz, 13.3 GHz, 21.6 GHz, and 27 GHz. To represent conditions in the outer planet's tropospheres, the temperature was varied from 175 K to 298 K and the pressure was varied from 1 to 6 bars. Their measurements provided an accuracy improvement by an order of magnitude when compared to previous measurements, and resulted in a significant increase in phosphine opacity. Phosphine was thus determined to be a dominant microwave absorber in the upper tropospheres of the outer planets.

Phosphine has a rich microwave and millimeter-wave spectrum. To develop a formalism that was usable in a vast number of different solutions, Hoffman *et al.* tried to keep their formalism consistent with data. In their calculation, they used the JPL catalog (Pickett *et al.*, 1981), which is a compilation of line strengths and frequency that have been measured or computed. The absorption from a collision-broadened gas can be calculated using the following:

$$\alpha_j = \sum A_j \pi \Delta \upsilon_j F_j(\upsilon, \upsilon_j ..) cm^{-1} \qquad 3.17$$

where, A_j is the absorption at the line center, $\Delta\upsilon_j$ is the line width, and F_j is the line shape function for line j. The absorption at the line center may be calculated from:

$$A_j = \frac{n_d S_j(T)}{\pi \Delta \upsilon_j} cm^{-1} \qquad 3.18$$

where n is the number density, S_j (Abraham, 1970) is the intensity of line j, which is scaled from the intensity calculated at a reference temperature:

$$S(T) = S(T_0)\left(\frac{T_0}{T}\right)^{\eta} \frac{e^{-hcE_l/kT} - e^{-hcE_h/kT}}{e^{-hcE_l/kT_0} - e^{-hcE_h/kT_0}} \qquad 3.19$$

$$\cong S(T_0)\left(\frac{T_0}{T}\right)^{\eta+1} e^{-(hc/k)E_l(1/T - 1/T_0)}$$

where the temperature dependence term η is approximately 1.5 for symmetric-top molecules, a molecule which has two moment of inertia that are the same, such as phosphine. E_l and E_h are the lower and upper state energies, in the unit of inverse centimeters. Using the equation for the intensity of line, the line center absorption becomes:

$$A_j = \frac{10^6 P_{(bar)}}{\pi k_B T \Delta v_j (cm^{-1})}\left(\frac{T_0}{T}\right)^{\eta+1} x S_j(T_0) e^{-(hc/k_B)E_{ij}(1/T - 1/T_0)} cm^{-1} \qquad 3.20$$

where $\Delta\upsilon_j$ is the line width, which is described by:

$$\Delta \upsilon_j = \sum_i \Delta \upsilon_{ij}^0 P_i \left(\frac{T_0}{T}\right)^{\xi ij} GHz \qquad 3.21$$

where Δv_{ij} is the line broadening parameter and ξ_{ij} is the temperature dependence for gas i and line j in units of GHz/bar. P_i is the partial pressure of gas i in bars.

The emissions from a planet are almost never monochromatic emissions. As the energy transitions to different levels, external influences result in a loss of energy in the

emission. The spectral lines will be broadened by differences in thermal velocities of atoms and molecules, damping of vibrations due to the loss of energy, and collisions between absorbing and non-absorbing molecules. This pressure broadening can be given by a variety of line shapes, Lorentz, Ben-Reuven, and Van Vleck-Weisskopf among others. While Lorentz is a simpler line shape than Ben-Reuven and Van Vleck Weisskopf, these line shapes differ in the far wings. For the case of our data, the Van Vleck Weisskopf line shape is used and is defined as:

$$F_{vvw}(v,v_0,\Delta v) = \frac{1}{\pi}\frac{v^2}{(v_0)^2}\left[\frac{\Delta v}{(v_0 - v)^2 - \Delta v^2} + \frac{\Delta v}{(v_0 + v)^2 + \Delta v^2}\right] \qquad 3.22$$

When the new opacity model was compared to the old model, it was found that at low GHz there is an order of magnitude discrepancy (Hoffman *et al.*, 1999). The new formalism corrects the discrepancy. This formulation for phosphine's opacity was added to the radiative transfer code used in this work.

3.7 Radiative Transfer Calculation

We modeled the data shown in Table 3.3 with a radiative transfer code based on the one described in Hofstadter and Butler (2003). That software was modified to include phosphine absorption as specified in the laboratory formulation of Hoffman *et al.* (2001), and to use the temperature, pressure, and cloud profiles generated by the ECCM.

To fit the data, the atmospheric composition of absorbing gases-principally phosphine, hydrogen sulfide, and ammonia- was varied to obtain a satisfactory fit. In our analysis, the bulk of the absorption of the relevant species occur underneath their

respective condensation altitudes, as determined by the Clausius Clapeyron relations noted earlier. Each species in the atmosphere has its own effect on the brightness temperature calculation. Here, we included phosphine absorption in the radiative transfer analysis as specified in the laboratory formulation of Hoffman *et al.* (2001), which will be further described in Section 3.7. By using the outputs of the ECCM as the inputs to the radiative transfer codes, the effect of each species is accurately taken into account.

Radio data is also sensitive to the temperature profile. The temperature profile being used is the output from the ECCM, and is regenerated for each fit based on the composition of the atmosphere. The temperature profile is generated using both the moist and dry adiabatic lapse rates, as appropriate for various regions of the atmosphere, as well as a known temperature and pressure value at the top of the atmosphere for convergence. With the newly coupled model, a more complete picture of Uranus' upper troposphere can be found.

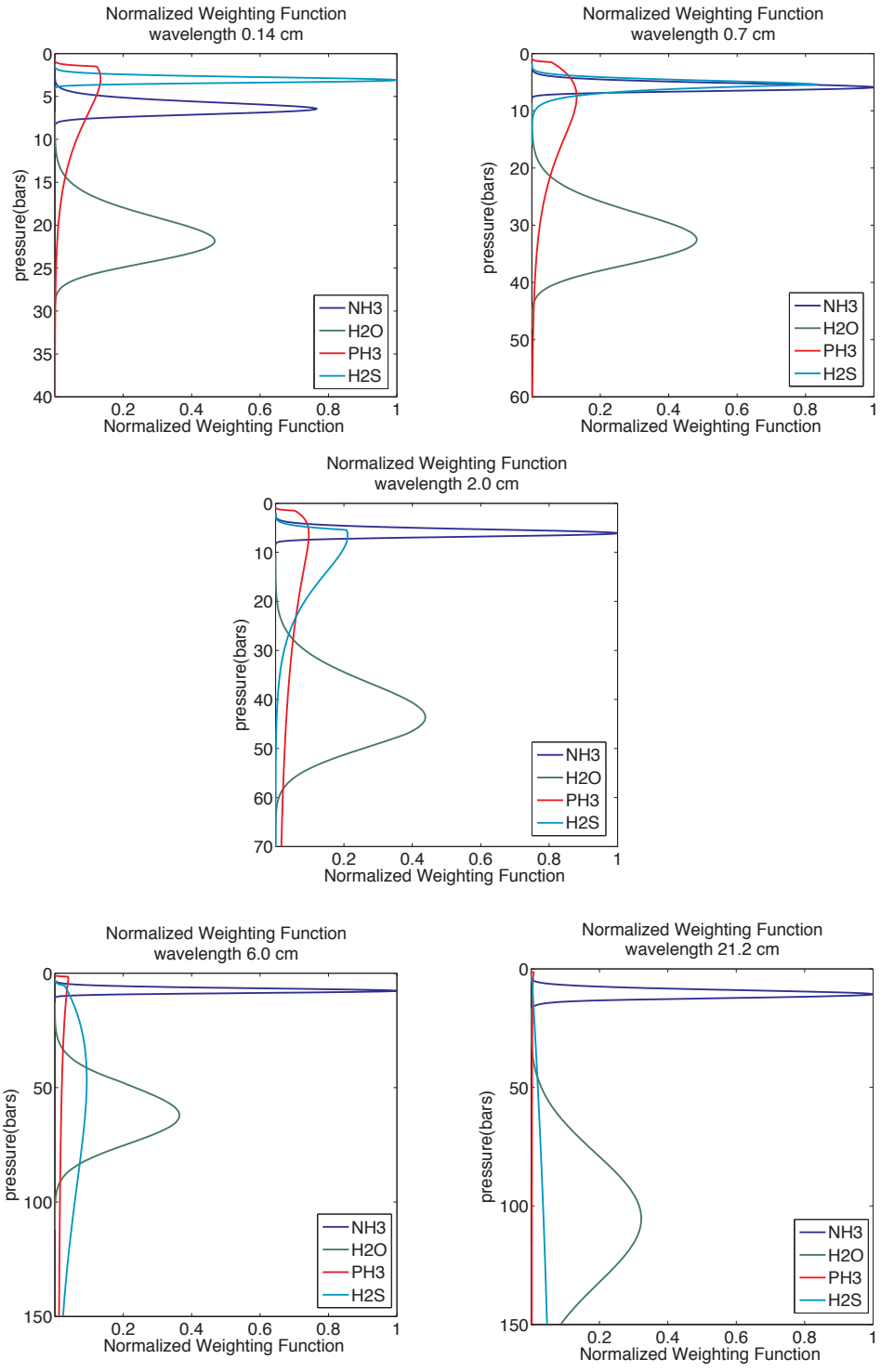

Figure 3.8 The weighting functions for each observing wavelengths is shown. In each plot, colored lines represent a single atmospheric species enriched to be 10 × solar. This gives the influence each different species has on each of the wavelengths. The weighting functions for our best-fit composition are shown later (Figure 3.11). In the shorter three wavelengths—0.14, 0.7, and 2.0—phosphine and hydrogen sulfide have an affect. Ammonia has an affect in all

wavelengths. Water has an affect in all wavelengths as well, but in the shorter three wavelengths other species are dominant.

In order to understand the influence that each species has at each wavelength, especially the newly added PH_3, weighting functions were calculated for atmospheres consistent of only one specie at each wavelength assuming a 10 × solar mixing ratio. As shown in Fig. 3.8, each wavelength has a specific set of species that controls what is emitted to space. The 0.14 cm region is controlled by H_2S with other species having significant influence. The 0.7 cm region is controlled by NH_3 or H_2S, with H_2O and PH_3 potentially having some effect as well. The 2.0 cm region is dominated by either NH_3 and/or H_2O. If NH_3 is depleted as predicted by de Pater *et al.* (1991), then H_2S will play a role. The 6.0 cm and 21.2 cm regions are controlled by NH_3 and H_2O with H_2S and PH_3 having almost no effect. Note that the weighting functions will change as the atmospheric composition is altered in the model; Fig. 3.8 is intended as an aid to help understand the controlling species at each wavelength and pressure region.

With the ECCM cloud code outputs being used as the inputs to the radiative transfer code and the addition of PH_3 to both the ECCM and the radiative transfer code, runs were executed to match the observed brightness temperatures from Table 3.3. For all of the model cases, the carbon enrichment was held constant at 20 × solar (Herbert *et al.*, 1987; Gautier *et al.*, 1995; Baines et al., 1995). Helium was held constant at 15% of the atmosphere (Conrath *et al.*, 1987). Changing the composition of the atmosphere, a variety of different brightness temperatures were calculated. We explored nitrogen abundances between 0.003 and 2 × solar with S/N ratios between 1 and 1000. Sulfur was allowed to vary from 0 to 30 × solar. With subsolar nitrogen, sulfur needs to be

enriched to approximately 30 × solar for a H_2S cloud to condense in the 6 bar region. PH_3 and H_2O were varied from 0 to 15 × solar.

As was seen in Figure 3.8, different compounds have an influence at different radio wavelengths. There are certain trade offs to consider when fitting the upper troposphere. The S/N ratio determines whether an NH_3 or H_2S cloud is present in the upper troposphere, and the H_2S cloud is found to be the most likely. This results in the PH_3 and H_2S working together to produce the opacity in the upper troposphere. H_2S's effects are strongest for the 0.14, 0.7, and 2.0 cm radio data points, while PH_3 is only influential for the shortest two wavelengths. Therefore, H_2S was used to fit the 2.0 cm radio data point and the PH_3 value was adjusted to match the shortest two wavelengths. Similarly, deeper in the troposphere a balance between NH_3 and H_2O vapor is needed as they both contribute to the opacity. Too much NH_3 resulted in the shorter wavelengths having too much opacity, while too little NH_3 resulted in the longer wavelength not having enough opacity. Similarly, the amount of H_2O vapor was varied to reflect the NH_3 abundance, as water vapor and NH_3 can supply the opacity at the longer wavelengths.

Keeping these relationships in mind, cases were tried for a variety of compositions and chi-square errors of the fits were calculated. Cases whose fits resulted in significant intervals greater than 70% were kept for further analysis, with the exception of the case without PH_3. That case was less significant, but was carried forward for discussion purposes. The 7 model cases are found in Table 3.4. The model cases represent a variety of solutions including: no PH_3 (Case 7), no H_2O (Case 5), 10 x solar H_2O (Case 3), 10 x solar PH_3 (Case2), and depleted H_2O (Case 4). Cases 8, the best fitting case with a cloud near 6 bars, and Case 9, the 20 x solar case for all species, are also shown for illustrative

purposes. The cases were further examined and those whose fits resulted in significance intervals less than 70% were discarded. The results of this study will be discussed in section 3.9.

3.8 Constraints from Visible and Near-IR Data

Additional constraints can be brought to bear on our analysis by incorporating the cloud structure results derived from visible-near-IR observations. Due perhaps to the latitudinal and/or temporal variability of Uranus's troposphere, two different two-cloud structure solutions have been published, based on data acquired about two decades apart. Each could plausibly be consistent with the presence of PH_3 vapor in the 3-5 bar region. In the Baines *et al.* (1995) solution, there is a single optically-thick layer of clouds at pressures greater than ~ 2 bar, with another upper-level layer at the CH_4 condensation level near 1.3 bar, while in the Sromovsky *et al.* (2006) model there are two clouds in the > 2-bar region. As shown by the weighting functions in Fig. 3.8, vapor from a variety of trace species (e.g. PH_3, NH_3, H_2S) can likely produce the observed microwave atmospheric opacity. The ice clouds formed at the condensation levels of these species serve to deplete the microwave-absorbing vapors above them, thus marking the maximum altitude (lowest pressure) where these absorbers are effective. We thus compared the microwave-based cloud levels derived over a variety of trace gas abundances with the cloud levels derived from visible-Near-IR data to determine whether any solutions exist that are consistent with both data sets.

The Baines *et al.* (1995) solution also requires a cloud at 3 bar, consistent with H_2S as was previously proposed by dePater *et al.* (1991). Baines *et al.* (1995) used broadband spectra and both the hydrogen quadrupole lines and the 6818.9 *Å* methane feature to constrain the methane cloud opacity, the CH_4 mixing ratio below the CH_4 cloud, the cloud top pressure level of the deep cloud, and the ortho-to-para hydrogen ratio. Their observations were acquired in 1980-1981, when the bright, relatively cloudy south polar region - as imaged by Voyager during its 1981 flyby - dominated the view from Earth. Despite the visual brightness of the Voyager-imaged clouds, they concluded that the methane cloud was optically thinner than expected given the relatively large abundance of CH_4 vapor – comprising more than 15% of the atmosphere by weight -- producing opacities averaging less than unity. From a global perspective, we note that such an optically-thin cloud layer should actually be termed a haze. To be sure, given the global nature of the observations, individual CH_4 clouds could be optically thick but with large clear regions separating them, thus mimicking a global haze. This would then imply some degree of active dynamics producing cloudy and non-cloudy regions.

The main source of microwave opacity is deeper in the atmosphere than the CH_4 haze layer. Baines *et al.* (1995) found that there is an optically thick cloud top at 3.1 bar (+1.1, -0.2) for Uranus. Due to the likely depletion of NH_3, this cloud is likely the H_2S cloud, which can condense near 3 bar. PH_3 is a possible but a less likely candidate for this cloud, as it condenses higher in the troposphere. As will be discussed later, the abundance of phosphorus in the atmosphere of Uranus is likely to be in the 4 to 10 × solar range, with a cloud base forming in the 1.3 to 1.4 bar pressure region, which is in the region of the methane haze. Thus the CH_4 haze in this model could plausibly be a mixture of PH_3 and CH_4 condensates.

Sromovsky *et al.* (2007) used the near-IR, 2000-9500 cm^{-1} band CH_4 absorption and improvements in the low-temperature CH_4 absorption reported by Irwin *et al.* (2006), to model Uranus' upper tropospheric cloud structure using Keck grism spectral images obtained with the NIRC2 instrument. These images were acquired for nearly the entire globe in 2006 – i.e., during the 2005-2009 epoch of the radio observations we have reported. Their analysis started by assuming two deep clouds in which the lower cloud was opaque and uniform across the planet while the upper cloud was a spatially non-uniform cloud deck. The best fit found was for cloud layers at both 2 and 6 bar. The upper cloud coverage was only 2.5%, which is approximately equal to a globally averaged cloud optical depth of 0.09, thus actually making it a globally averaged haze layer. This upper haze/cloud could potentially be explained by a PH_3 haze/cloud, as solutions with 50 × solar abundances can condense near the 2 bar level and lower cloud densities are expected for this cloud than the other clouds in the atmosphere.

Sromovsky *et al.* (2006) proposed another model where clouds are placed at six different pressures from 0.15 to 6 bar. All of the clouds are assumed to be broken and of unit albedo. This multi-layer model had a better fit to their near-IR data than any two-cloud-model. Modeling the Keck measurements with their radiative transfer model, the H-band spectral variability was found to fit the data with clouds near 2 to 3 and 6 to 8 bars. The lower cloud reflectivity appears to vary latitudinally. The authors propose both the upper and lower clouds are H_2S.

The differences between Sromovsky *et al.* (2006, 2007) and Baines *et al.* (1995) are the wavelengths of observation and the sensitivity of each of those wavelengths to aerosols. With differing sensitivity, different potential morphologies are possible. Baines *et al.* (1995) measurements are more sensitive to smaller particles than the near inferred

data and the increased sensitivity to smaller particles may explain why Baines *et al.* solution results in a cloud higher in the atmosphere than Sromovsky *et al.* solutions. The Sromovsky *et al.* solution is more sensitive to larger particles. This increased sensitivity to large particle may be responsible for the deeper cloud base locations predicted by their model.

Encrenaz *et al.* (1996) suggested an upper limit on the mixing ratio of PH_3 of 2.6 × 10^{-6} (4 × solar abundance) in the 90-100 K region (0.5-1.5 bar) of Uranus' troposphere, a region probed by our millimeter-wavelength data. If PH_3 were enriched beyond 10 × solar, the cloud base would be at pressures greater than the 1.5 bar level, and the PH_3 abundance in the region probed by Encrenaz *et al.* would be controlled by the saturation vapor pressure. Therefore, the 4 × solar maximum PH_3 abundance they report is not relevant to the deeper abundances used in our modeling, so we allow solutions that contain more or less than 4 × solar. When PH_3 is enriched 1, 2, and 4 × solar the PH_3 cloud is present at 1.1, 1.2, and 1.3 bar respectively, and this is plausible with the uppermost haze levels derived by both Baines and Sromovsky. As mentioned previously, this is also a region where a (higher opacity) CH_4 ice cloud is expected to form, and that the actual opacity would most likely be due a combination of PH_3 and CH_4 opacities.

3.9 Radiative Transfer Results

Prior to this study there have been no analyses that suggest the presence of a PH_3 cloud in Uranus. Here we demonstrate that cloud-model constraints previously derived from visible-Near-IR measurements are consistent with the presently available PH_3-

sensitive radio data that incorporate PH_3 vapor abundances of sufficient magnitude to produce an optically-thin yet detectable PH_3 haze layer.

We explore several morphologies for Uranus' cloud and vapor structure. Case 7 represents the only case without PH_3. The significance interval of the fit for this case is 58% and is the worst found in our study. For this poor solution, the H_2S cloud near 4.7 bar is the only plausible cloud save for the CH_4 cloud near 1.3 bar. At the H_2S cloud base, the H_2S cloud density is 1.8×10^{-5} g cm^{-3}. At the 3 bar layer where Baines *et al.* (1995) derive the top of their optically-thick cloud, the cloud density falls to 4.34×10^{-7} g cm^{-3}, sufficient over a few km (~ 0.3 bar) of depth to provide the requisite 3-bar cloud opacity The poor quality of Case 7 indicates that PH_3 is present in the upper troposphere of Uranus.

Table 3.4 The nine categories of fit found for which the radiative transfer code matched the VLA/SMA data. Case 8 represent the best fit case from the cloud base at 6 bars, and is not statistically significant. Similarly, case 9 represent the case of 20 × solar for all species and is found to be poor fitting as well.

Nine model cases for radio data at Uranus

Case	C	N	O	P	S	0.14cm	0.7cm	2.0cm	6.0cm	Significance interval	PH_3 cloud	H_2S cloud
1	20	0.05-0.1	2-4	7-10	1-2	96.9K	148K	177K	217K	92%	1.3 bars	3.8 bars
2	20	0.008-0.04	10	7-10	0.5-1.5	96.9K	150K	178K	227K	85%	1.4 bars	3.7 bars
3	20	0.1	2-3	4	3-4	97.5K	145K	180K	224K	83%	1.3 bars	4.2 bars
4	20	0.3	0.4-0.5	6	1-2	97.0K	145K	178K	212K	76%	1.3 bars	4.1 bars
5	20	0.6	0	6	4	96.9K	147K	178K	210K	72%	1.4 bars	4.0 bars
6	20	0.4	1	6	4	97.5K	144K	182K	216K	71%	1.3 bars	4.2 bars
7	20	0.3	3	0	7	98.4K	142K	182K	225K	58%	0 bars	4.7 bars
8	20	0	2	0	20	94.9K	134K	156K	215K	6%	0 bars	6.2 bars
9	20	20	20	20	20	92.8K	122K	126K	141K	0%	1.6 bars	0 bars*

* There is no H_2S cloud because there is an NH_3 cloud at 13 bars

The rest of the cases all represent cloud solutions, which include PH_3 vapor. For all of these solutions, the PH_3 condensate haze/cloud was found to be between 1.3 to 1.4 bar – that is near the methane haze layer of Baines et al (1995) - and the H_2S cloud was between 3.7 to 4.7 bar. All of the H_2S clouds have densities near 10^{-6} g cm^{-3} at the cloud base, and at 3 bar the cloud densities are approximately 10^{-7} g cm^{-3} without precipitation again sufficient to produce significant opacity over a few km of altitude. Note that Cases 1 through 4 in Table 3.4 quote a range of values for some species. This is because there were multiple solutions with similar compositions. Model results for the best solution within in each Case are indicated in Table 3.4. Figure 3.9 shows how the cases match the data and the error bars associated with each point. Note that all of the cases are found within the one-sigma error bars.

No statistically significant cases were found for a cloud base near 6 to 8 bar as is required by the Sromovsky (2006; 2007) models. Figure 3.10 shows the cloud density and locations for the cases. In order for a H_2S cloud to exist in the 6 bar region, the required sulfur enrichment is 20-30 × solar in the upper troposphere, assuming no deeper NH_4SH cloud, and resulting in a statistical significance of less than 6%. Case 8 in Figure 3.9 shows the poor fit of this case. This would result in too much vapor opacity for the 0.7 cm and 2.0 cm data points. Barring an extremely dynamic deep atmosphere populated by large, powerful upwellings – contrary to the quiescent behavior of the visible atmosphere - the base of the NH_4SH cloud - located near the 25 bar region for plausible N and S abundances found in this study -is too deep in the atmosphere to be responsible for this cloud. The H_2O, similarly, is likely too deep in the troposphere – that is, with a cloud base near the 42.5 bar level or deeper for this study's abundances - to provide this opacity. The Sromovsky cloud models do not seem consistent with our data and model

assumptions. It should be noted that the Sromovsky and Fry (2006; 2007) measurements were taken in 2006, near equinox, contemporaneous with our radio data, while the *Baines et al.* (1995) measurements were acquired in 1980-1981 when Uranus was close to southern solstice with the sub-Earth latitude greater than 80 degrees S. Therefore, it is surprising that the Baines *et al.* (1995) model is a better fit than the Sromovsky and Fry (2006; 2007) model.

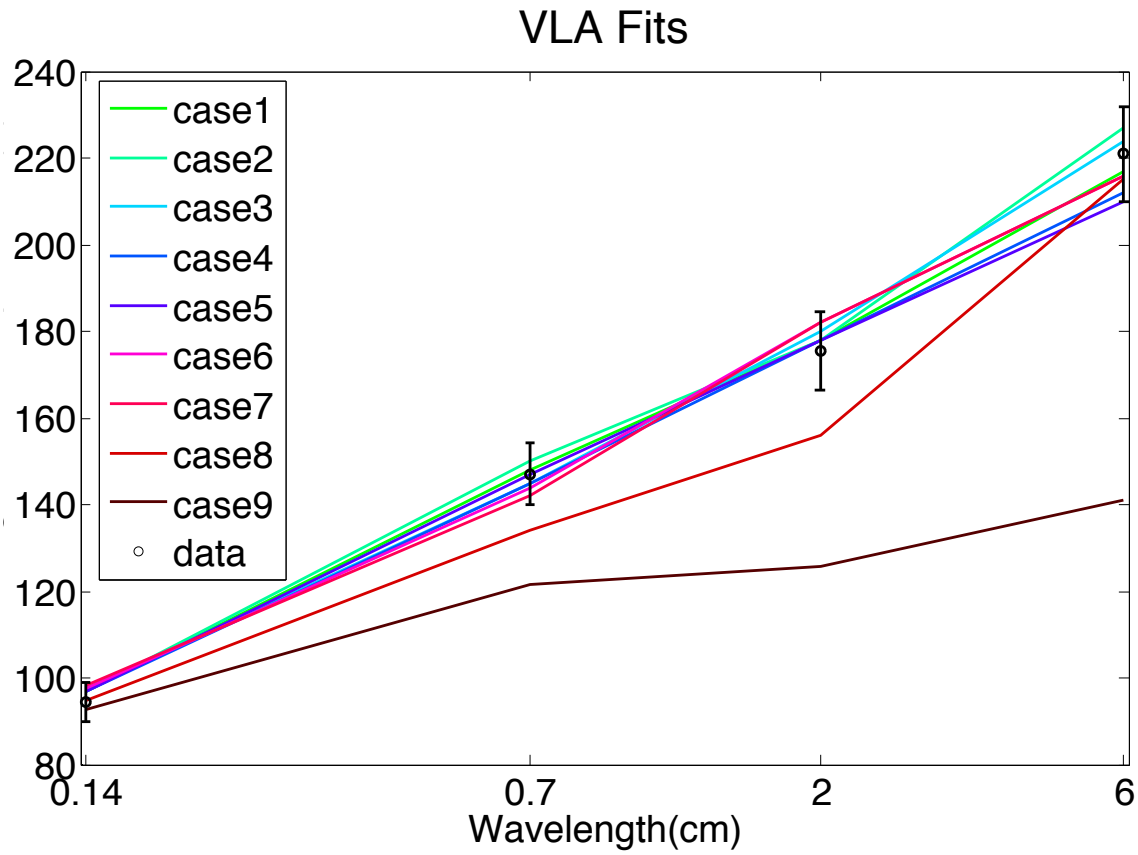

Figure 3.9 The model brightness temperatures from Table 3.4 compared to the radio data. Note that case 1 through case 6 show fits with a significance interval better than 70%. Case 7 show the best fitting case without phosphine present. Case 8 is the best fitting case for a cloud at 6 bar, however the significance interval is only 5%. Case 9

shows the match for 20 × solar for all species. Cases 1 through 6 all represent plausible model fits.

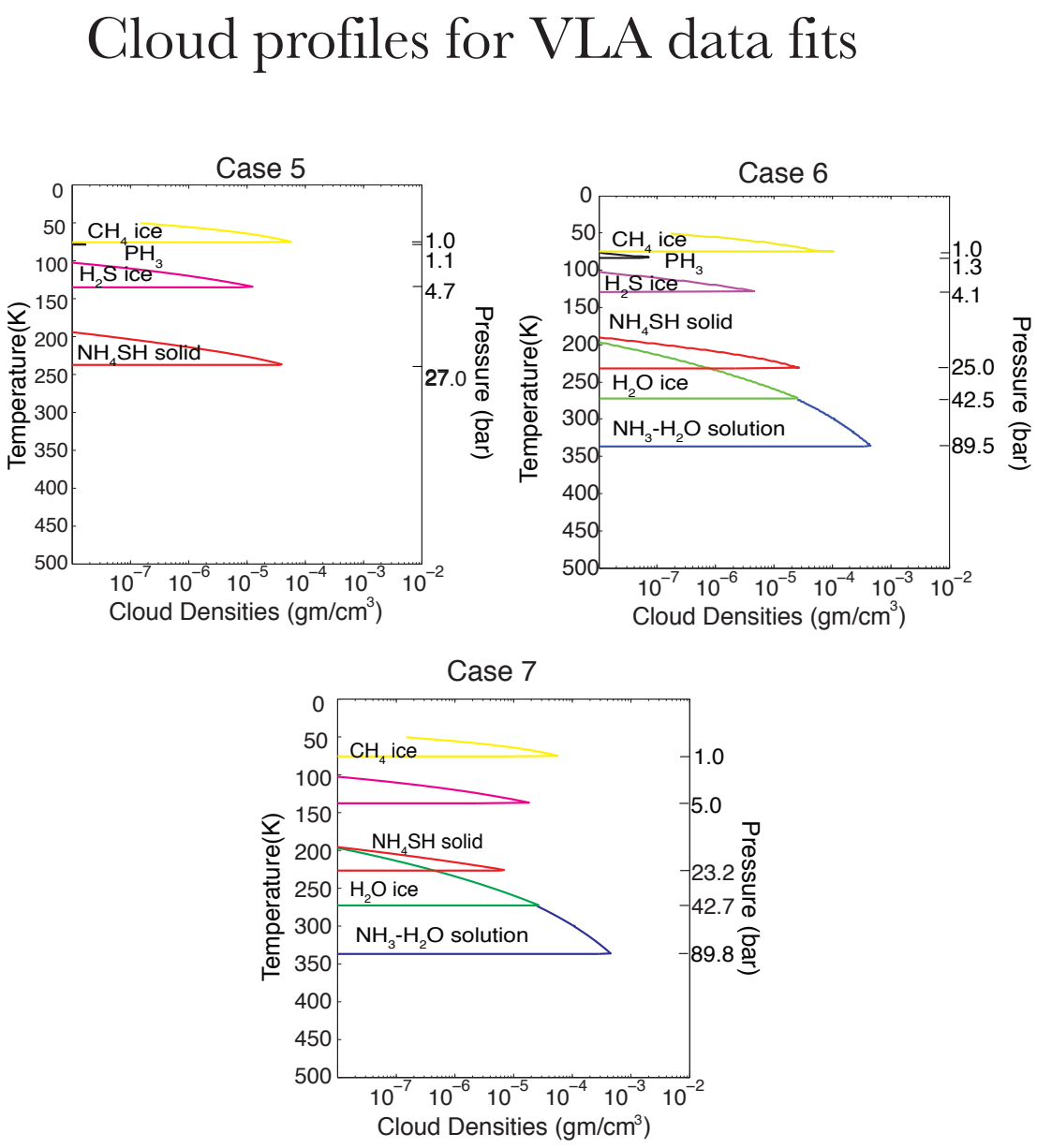

Figure 3.10 The cloud solutions for cases 5, 6, and 7. These cases represent the 3 different solutions that were obtained with the VLA data. The ECCM runs represent an upper limit, and the actual cloud concentrations could be reduced by a factor of up to 1000 due to precipitation. The microwave absorptions (VLA/SMA) are for the most part affected by vapor concentrations alone.

For most of our radio data points, all of the cases are found within the uncertainties. The exception to this is that the 21.2 cm data point is only satisfactorily matched by case 6. With the 21.2 cm data point, case 6 had a 78% significance interval, while the rest of the cases were below this value. The lack of a good fit to the 21.2 cm data point could be the result of our model not accounting for an opacity source present in the deep troposphere. A preliminary analysis of the VLA's 21.2 cm image reported in Hofstadter *et al.* (2011) supports this as yet unidentified source. Since the 21.2 cm data point has little influence on the upper part of the troposphere which is the focus of the present study (Fig. 3.8) we removed it from consideration. All of the cases presented in Table 3.4 are with respect to the 0.14, 0.7, 2.0, and 6.0 cm radio measurements. The missing deep opacity will be examined in Chapter 4.

To identify the viable solutions among our 7 cases, a chi-squared analysis is used. Cases that have a higher chi-square error are less significant than those with lower values. Table 3.4 contains the significance interval for all cases, which indicates the likelihood that the model actually fits the data instead of it being by chance. Cases with significance intervals higher than 70% were kept as possible solution. The only solution eliminated was the case that did not contain PH_3. All of the model cases can be seen in table 3.4 as is the range of elemental abundances: nitrogen, 0.008-0.6 x solar, oxygen, 0-10 x solar, phosphorus, 4-10 x solar, and sulfur, 0.5-4 x solar. The best model case had a significance interval of 92%. The normalized weighting functions and the vapor mixing ratios for this case can be seen in Fig. 3.11 showing how each specie affects the mixing ratio. The relationships seen are similar to those shown in Fig. 3.8 with H_2O controlling the longer wavelengths, and PH_3 and H_2S controlling the shorter wavelengths.

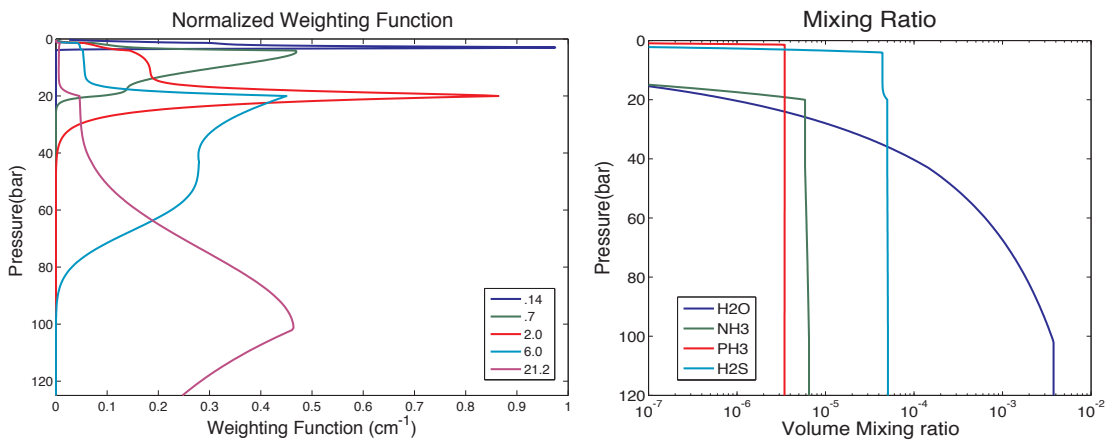

Figure 3.11 The normalized weighting functions for each observing wavelength- 0.14, 0.7, 2.0, 6.0, and 21.2 cm (left) and the mass mixing ratio of the condensables (right) for Case 1. The location of the cloud base is important as when the species are gaseous they have more of an influence on the opacity then when the species are liquid/solid.

NH_3 has previously been found to be severely depleted relative to solar N/H (Gulkis *et al.*, 1978; de Pater *et al.*, 1991) on Uranus. With the addition of the PH_3 cloud, we reexamined if NH_3 is still depleted. As noted earlier, the sulfur-to-nitrogen (S/N) ratio dictates which cloud, NH_3 or H_2S, is present in the upper troposphere of the ice giants. Cases were tried that would result in NH_3 being the upper-tropospheric cloud however no fits were found statistically significant. All of the fits found to match our radio data contained more sulfur than nitrogen, thus allowing the presence of a H_2S cloud. The fits that were found have variable S/N ratios of 7 to 30. This strongly indicates that it is highly likely that there is no NH_3 cloud present in the upper atmosphere, and the Gulkis *et al.* (1978) and de Pater *et al.* (1991) hypothesis is still upheld.

The remaining cases represent a variety of solutions. The two characteristics that the solutions all share are a depletion of NH_3 and the presence of a PH_3 haze/cloud. No satisfactory solution was found for models incorporating both undepleted NH_3 and a PH_3

cloud, allowing us to say with some confidence that NH_3 is likely depleted in the upper troposphere of Uranus. We can also draw the conclusion that PH_3 likely produces a haze or cloud in the upper troposphere. Better constraints on what is governing the opacity of the 21.2 cm wavelength are needed in order to make claims about the deeper atmosphere.

The statistically significant models that match the radio data are found to have cloud locations reminiscent of the Baines *et al.* (1995) two-cloud solution. There were no statistically significant fits that resulted in a cloud at 6 bar, therefore the Sromovsky and Fry (2006; 2007) two-cloud model is not favored. It should be noted that the Sromovsky and Fry (2006; 2007) measurements were taken in 2006, near equinox, contemporaneous with our radio data, while the Baines *et al.* (1995) measurements were acquired in 1980-1981 when Uranus was close to southern solstice with the sub-Earth latitude greater than 80 degrees S. Therefore, it is surprising that the Baines *et al.* (1995) model is a better fit than the Sromovsky and Fry (2006; 2007) model.

In summary, we find a range of possible values for the amount of condensables in the upper troposphere. Phosphorus can be set at 4 to 10 × solar, nitrogen of 0.008 to 0.6 × solar, oxygen of 0 to 10 × solar, and sulfur of 0.5 to 4 × solar. None of these enrichments match the enrichment of 20 to 30 × solar found for carbon (Herbert *et al.*, 1987; Gautier *et al.*, 1995). A summary of the resulting cloud structures can be seen in Fig. 3.10. Cases 5, 6, and 7 are shown as they represent the range of solutions found. Case 5 represents our two-cloud solution, which is similar to that of Baines *et al.* (1995), case 6 shows the no H_2O solution, and case 7 shows the no PH_3 cloud solution.

3.11 Conclusions

Using lower temperature laboratory PH_3 vapor measurements, a new saturation vapor pressure equation for PH_3 is derived that improves upon the previously used equation. When this new equation is applied to Uranus' atmosphere, it results in a cloud base approximately 0.1 bar lower in pressure than the previous equation, and a slightly lower density at the cloud base. This is not a significant change over the previous equation used in Encrenaz *et al.* (1996), but it was derived with lower temperature measurements that resemble the environment at Uranus. The PH_3 cloud is found to be present in the 0.9 to 2.2 bar region for enrichment factors of 0.1 × solar to 20 × solar. The concentration at the cloud base for these clouds varies from 10^{-10} g cm^{-3} to 10^{-8} g cm^{-3} before precipitation.

By adding the opacity of PH_3 to a radiative transfer model, and coupling this model with the ECCM, a more accurate picture of the atmosphere of Uranus is obtained. This coupled model was compared to radio observations at wavelengths from 0.14 to 21 cm, made at the VLA and SMA observatories between 2005 and 2009 and reported here. Comparing our radio data to the model, a variety of solutions are found that are consistent with the two-cloud solution proposed by Baines *et al.* (1995). No solutions are found to explain the two-cloud solution proposed by Sromovsky and Fry (2006; 2007). Seven different categories of fits are found, and one of the cases was found to be not statistically significant. This case was the only no-PH_3 cloud solution, which points to the likely presence of the PH_3 cloud. Furthermore, only one case is found to match the 21.2 cm data point. This points to this case either being correct or there is an unaccounted opacity source deep in the atmosphere that needs to be further studied. The range of

upper tropospheric elemental abundances we find to be consistent with the available radio and visible/near-IR data are: PH_3 of 4 to 10 × solar; NH_3 of 0.008 to 0.6 × solar; H_2O of 0 to 10 × solar and H_2S of 0.5 to 4 × solar. With recent improvements made to the VLA observatory and the completion of the Atacama Large Millimeter Array, we expect more observational constraints will be available in the near future.

Chapter 4 : INTERIOR OF URANUS

Interior measurements of the ice giants are limited to gravitational moment measurements from Voyager 2 and simulations performed on Earth (Weir *et al.*, 1996; Collins *et al.*, 1998; Nellis *et al.*, 1999). Voyager 2 detected a complex magnetic field whose origin is not fully understood (Connerney *et al.*, 1987; Kirk and Stevenson, 1987). Some of the possible sources are an ionic ocean or metallic water layer at the kbar level in Uranus. Tropospheric species elemental abundance may be a clue as to what is occurring in the deep interior. All Solar System formation models expect that the enrichment of elemental abundances in the gas planets are greater for planets further away from the Sun. Therefore, if species are not found to be enriched, then a deep sink may exist for these species, such as an ionic ocean. This problem will be addressed in greater detail in this chapter.

4.1 Interior Theory

The fields of planetary formation and interior structure have evolved during the past decade due to new high-pressure experiments. The deep heavy elemental abundances are still poorly constrained. The mass of the planets, their equatorial radiuses, and gravitational moments as measured by the Pioneer and Voyager 2

spacecraft missions were used to constrain the interiors of the giant planets (Weir *et al.*, 1996; Collins *et al.*, 1998; Nellis *et al.*, 1999). The gravitational moments of the ice giants are known to a lower accuracy than the gas giants, and are harder to constrain with models. The ice giants contain a smaller fraction of hydrogen and helium than the gas giants, which contributes to the composition of interiors of these planets being less certain as the heavy elements are not well constrained.

The three-layer model, consisting of a central "rock" core, an ice layer, and a hydrogen-helium gas envelop, has been proposed for the ice giants (Gulliot, 1999a). Figure 4.1 shows a schematic for the interior structure of the ice giants. Models that apply this homogeneity of layers and adiabatic temperature profile are unable to reproduce the gravitational moments observed at Uranus, which possibly implies that parts of the planet's interior are not homogeneously mixed (Podolak *et al.*, 1991b; Hubbard *et al.*, 1995; Podolak *et al.*, 1995). This potential non-homogeneity could explain why the heat flux at Uranus is smaller than the other giant planets, as heat may have to slowly escape by diffusion (Guillot, 1999b). The overall composition of the ice giants by mass is 25% rock, 60 to 70% ice, and 5 to 15% hydrogen and helium (Podolak *et al.*, 1991a; Podolak *et al.*, 1995).

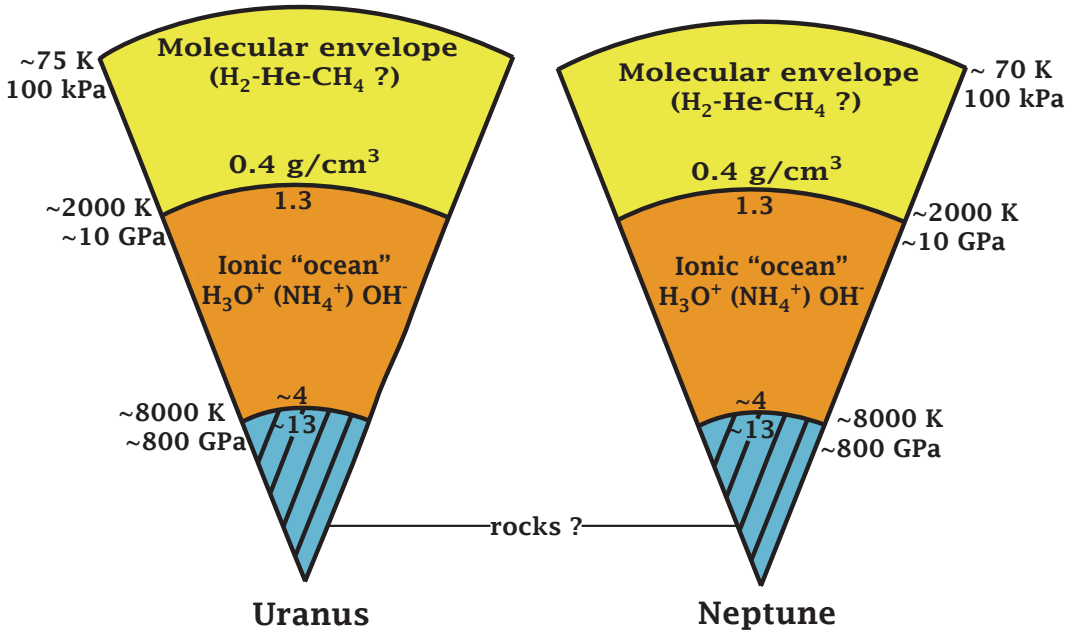

Figure 4.1 The interior structure of the ice giants. There are three hypothesized layers: core, ionic 'ocean' and molecular envelope (Guillot, 1999a). This is different from the gas giant where there is likely a metallic hydrogen that is responsible for the generation of the magnetic field.

The composition of the interior is thought to be responsible for the origin of the magnetic field. Voyager 2 discovered a large magnetic field at Uranus of up to 1 gauss (Connerney *et al.*, 1987). Therefore, something needs to be responsible for sustaining the electrical conductivities of 10 ohm^{-1} cm^{-1} that are needed to sustain the planetary dynamo mechanism (Kirk and Stevenson, 1987). The gas giants' interiors have a metallic hydrogen layer that is the likely source of their magnetic fields, but the ice giants lack this layer. Instead, it is thought that an ionic ocean or metallic water layer may be present in the interior of ice giants that generates the magnetic fields.

4.2 Ionic Ocean

Density profiles of the ice giants suggest that between the rocky core and a gaseous atmosphere there is a thick layer composed of "hot ices." These "hot ices" are predicted to be composed mostly of water with some hydrocarbons and ammonia (Hubbard, 1981). Computer models have been used to explore this region of the atmosphere. One of the earliest simulations was performed by Cavazzoni *et al.* (1999), and their simulation estimated the phase diagram of water and ammonia at pressures of 30 to 300 GPa and temperatures of 300 K to 7000 K. Figure 4.2 displays the calculated phase diagrams. Cavazzoni *et al.* (1999) also predicted that the ice layer is electronically insulating to $P < 300$ GPa. Molecular water generated a low ionic conductivity at low pressures. Deeper in the planet, water and ammonia were found to be metallic, which could make them responsible for the generation of the magnetic field.

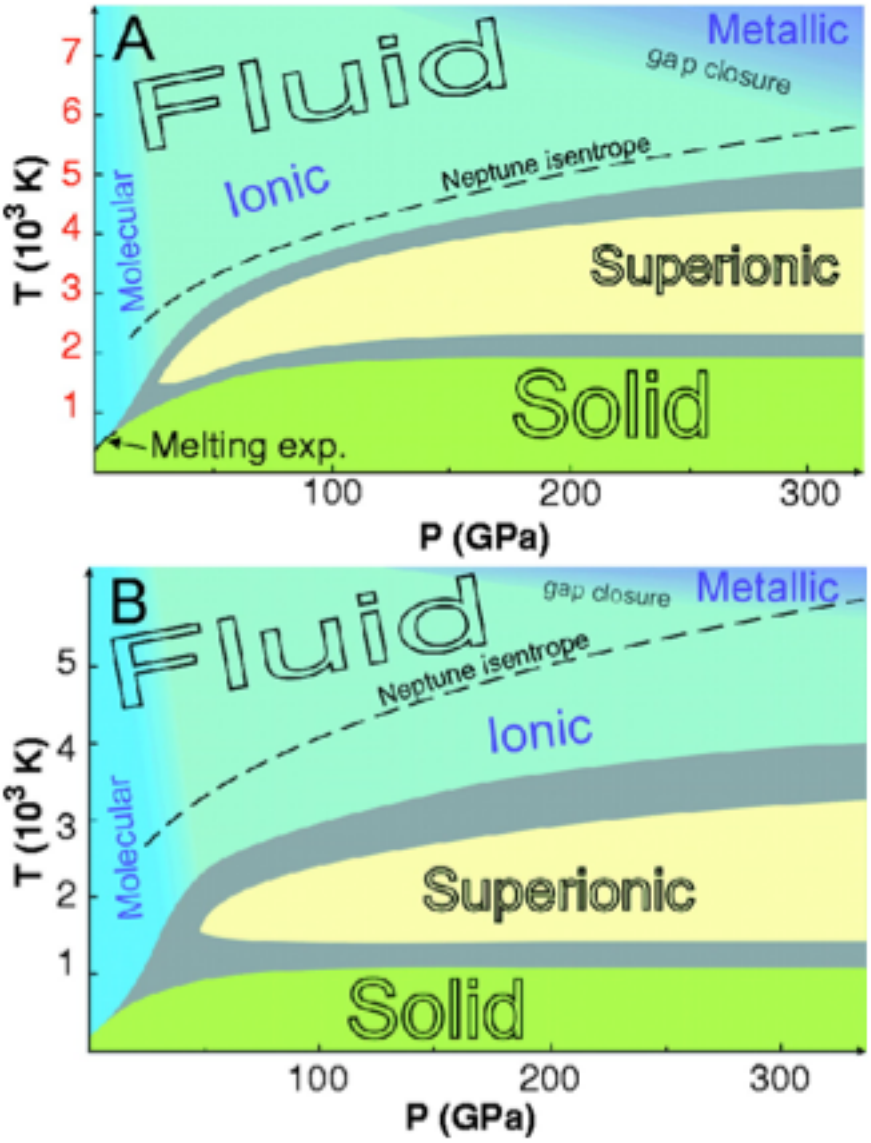

Figure 4.2 Phase diagram of water (A) and ammonia (B) from Cavazzoni (1999). The gray region indicates the error bar on the phase boundaries. The Neptune isentrop (dashed line) is from Podolak and Stevens (1995). Both the ammonia and water diagrams included multiple phases: the super ionic solid, the nonmetallic ionic liquid, and the metallic ionic liquid state. The ammonia phases were found at lower temperatures than their corresponding water phase.

Calculations performed after Cavazzoni *et al.* found that large amounts of water diffusion are characteristic of a fluid state (Schwegler *et al.*, 2000; Schwegler *et al.*, 2001). Studies of water in extreme conditions used to be limited to shock-wave compression investigation, however, a Raman study of shock-compressed water showed the persistence

of water molecules at 26 GPa, and identified the absence of hydrogen bonding (Holmes *et al.*, 1985). Goncharov *et al.* (2005) obtained the Raman Spectra for ice and liquid water at pressures from 5 to 56 GPa, at temperatures of 300 to 1500 K. These results were combined with molecular dynamic simulations. The results of Goncharov *et al.* (2005) suggested that water under extreme conditions will form a super ionic phase above 47 GPa, which is twice the pressure previously predicted. The composition of the super ionic phase would contain relatively short-lived species of H_2O, H_2O^+, and OH^-. The phase bound are between the liquid and super ionic state is steeper than was previously found. This work was expanded on by Goldman *et al.* (2005), who concentrated on bonding within the super ionic phase. Using molecular dynamics, three different phases were found. A new phase diagram was derived and can be seen in Figure 4.3 (Datchi *et al.*, 2000; Dubrovinskaia and Dubrovinsky, 2003; Frank *et al.*, 2004; Lin *et al.*, 2004).

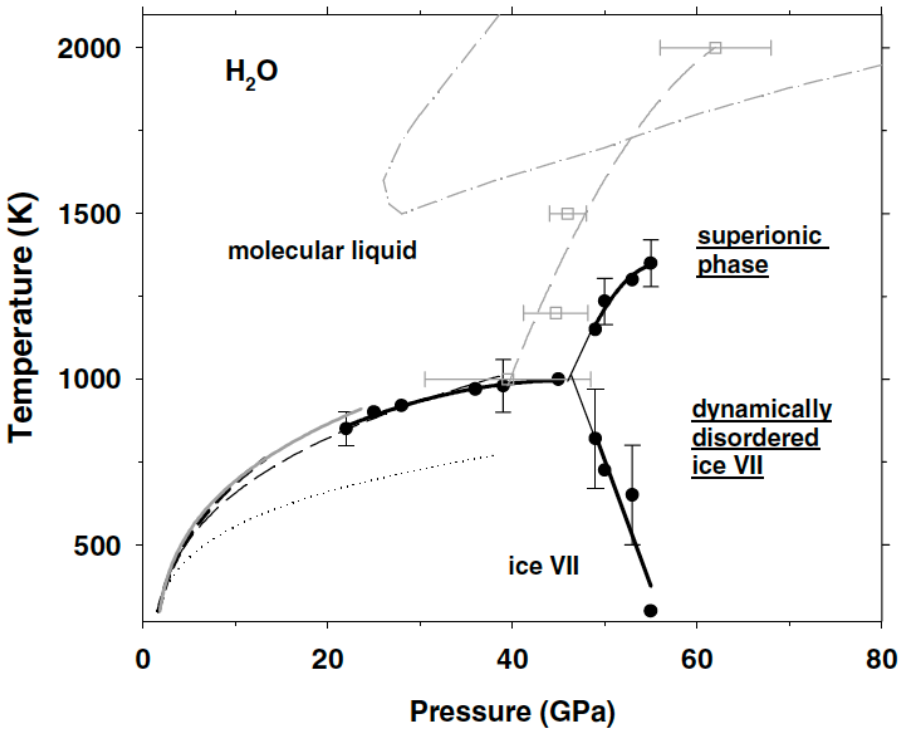

Figure 4.3 Phase diagram of water from Goncharov (2005). The solid circles correspond to the transformation points determined from spectral data, the thick solid lines are guides for the eye for experimental results, thin solid lines are extrapolations of measured lines, gray squares and dashed lines are theoretically computed conditions for freezing water, and the dashed lines are interpolated data from previous work (Datchi *et al.*, 2000; Dubrovinskaia and Dubrovinsky, 2003; Frank *et al.*, 2004; Lin *et al.*, 2004).

The proposed ionic ocean possibly exists at pressures of ~10 GPa with a primary composition of $H_3O^+ \bullet NH_4^+ \bullet OH^-$. Therefore, if the ionic ocean exists, then nitrogen and oxygen may be depleted in the troposphere of the ice giants. At room temperature, hydrogen sulfide and ammonia are soluble in water. Solubility is a function of temperature and pressure, and therefore we cannot know if hydrogen sulfide and ammonia will be soluble at pressures of ~100 kbar. If they are, then sulfur and nitrogen could both be depleted in the troposphere. The fits found to the VLA data in Chapter 3 will be used in the next section to further examine this relationship.

4.3 Implications

In situ measurements of the deep interior of the ice giants are currently impossible due to the harsh pressure environment. The elemental abundances of species in the troposphere may contain information about the deep interiors of the ice giants. From planetary formation theory and our knowledge of the composition of the other giant planets, a certain elemental abundance enrichment is probable. It is generally accepted that the elemental abundances of volatiles in the giant planets that are further away from the Sun will be more enriched than the giant planets closer to the Sun. Therefore, if the volatiles are found to be less enriched in Uranus than in Jupiter or Saturn, there may be an interior sink such as an ionic ocean.

As previously discussed, a relationship exists between the amounts of nitrogen and sulfur, which dictates the clouds in the upper troposphere. The presence of a hydrogen sulfide cloud indicates a lack of ammonia in the upper troposphere and a potential sink for the ammonia deeper in the ice giants. The measurements from the VLA, as seen in Chapter 3, point to depleted ammonia in the upper troposphere (Gulkis *et al.*, 1978; de Pater *et al.*, 1991); therefore, without an observation to prove otherwise, a deep sink for ammonia may exist. Figure 4.4 demonstrates the effect that decreasing nitrogen and oxygen can have on the clouds and the presence of an ionic ocean by showing how decreasing the nitrogen and water changes the cloud structure in the troposphere.

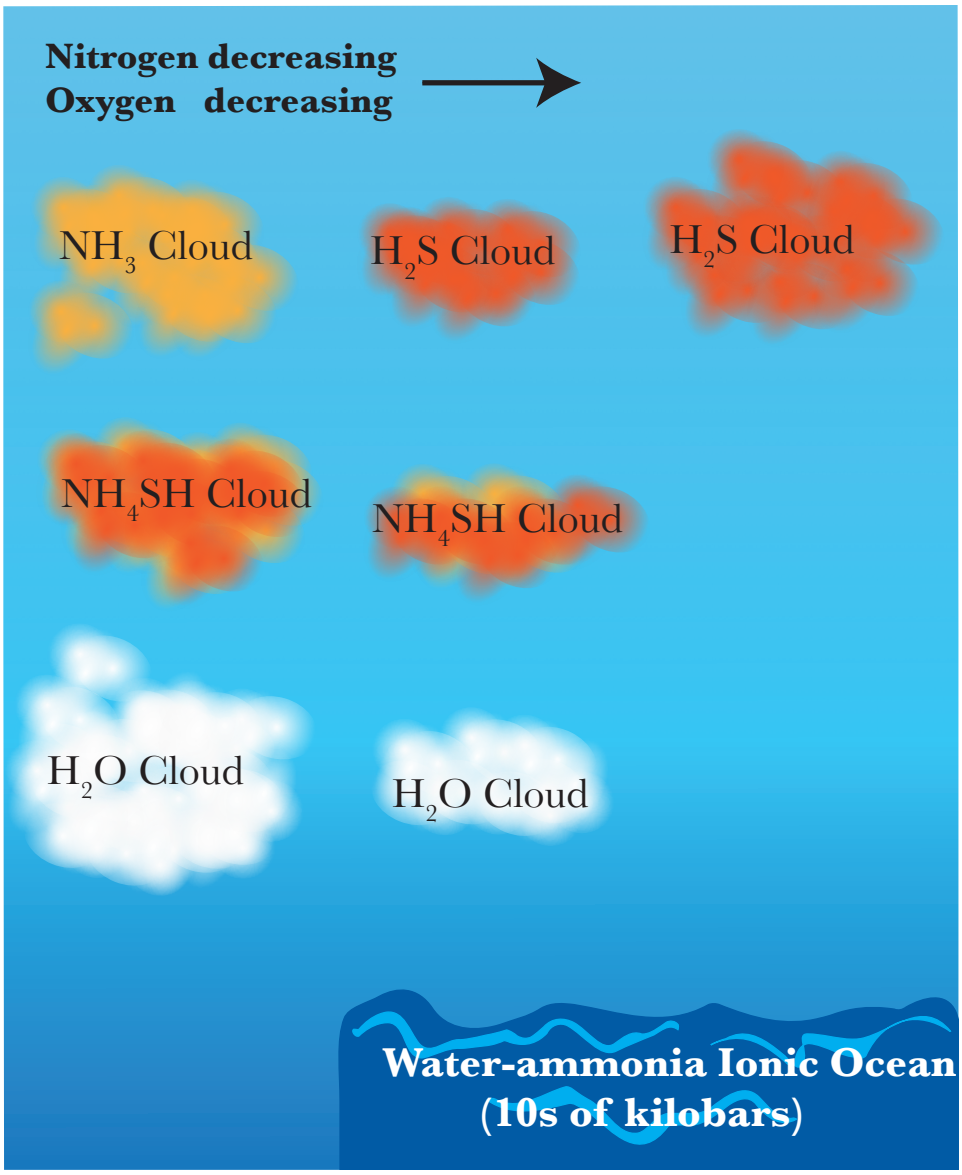

Figure 4.4 When there is more nitrogen in the atmosphere then sulfur, an ammonia cloud exists in the upper troposphere of Uranus. However, if sulfur enrichment stays the same as nitrogen is decreased, than a hydrogen sulfide cloud exists in the upper troposphere. Furthermore, as the amount of nitrogen decreases the hydrogen sulfide cloud will increase as not as much of the hydrogen sulfide is being used in the NH_4SH. If oxygen is similarly depleted, then an ionic ocean could exist at the kbar level.

The addition of the VLA data resulted in a more accurate understanding of the composition of the upper troposphere. In all of the fits found in Chapter 3, all of the condensables were enriched below what Voyager 2 measured for carbon (Herbert *et al.*, 1987; Gautier *et al.*, 1995). The sulfur to nitrogen ratios of the fits, which vary from 7 to

30, are seen in Table 4.1. None of the cases contained more nitrogen than sulfur. Ammonia, therefore, could have a deep sink in order to uphold current Solar System formation schemes. This sink can be a deep-water cloud, an ionic ocean, or a combination of both. Ammonia is more apt to have these sinks if water is also depleted in the upper troposphere as the ionic ocean requires both. The oxygen ratio varied from 0 to 10 × solar. It can be argued that water is going to be more enriched than the other volatiles if the clathrate formation model is true (Gautier *et al.*, 2001). Therefore, until more is known about the amount of the water in the atmosphere and the location of the water, nothing definitive can be said about the ammonia sink in the interior. All of the volatiles were less enriched then the expected carbon values, however, the actually elemental abundance is unknown in these planets.

Constraining each species' elemental abundance is further complicated by cloud microphysics, as the processes that occurred within the clouds affect the fits to the VLA data. Assuming the clouds are raining, the condensables will evaporate and condense again. When they are in the gas phase, they will have an effect on the opacity of the atmosphere in the radio wavelengths. The type of cloud helps determine the effect of microphysics. In a high cirrus cloud, precipitation is not likely to occur. The cirrus cloud, however, may be affected by the dynamics in the atmosphere. Winds could break apart the cloud and also supply new material for cloud formation. Therefore, it is only possible to give a range of potential elemental abundances until more is learned about the dynamics of Uranus' atmosphere.

Table 4.1 Sulfur to Nitrogen ratio for the VLA fit cases. This value varied from 8 to 160, and the hydrogen sulfide cloud was located between 3.7 to 4.7 bar.

S/N ratio for VLA fits

Case	S/N	H_2S cloud
1	15	3.8 bars
2	25	3.7 bars
3	30	4.2 bars
4	10	4.1 bars
5	7	4.0 bars
6	10	4.2 bars
7	23	4.7 bars

The enrichments at Uranus should be greater than that seen at Jupiter based on Solar System formation theory. While our results represent a variety of solutions, none of the solutions had species as enriched as carbon. The greatest enrichment factors found were 10 × solar for oxygen and phosphorus. Sulfur's maximum enrichment was found to be 4 × solar. Nitrogen was not found to be enriched, or even solar, in any of the cases. The relationship between Jupiter's elemental abundances and Uranus' can be seen in Figure 4.5. As seen in Chapter 1, the elemental abundances at Jupiter was 4.9 × solar for nitrogen, 0.54 time solar for oxygen, 3.23 × solar for sulfur, and 4.8 × solar for phosphorus using Asplund's (2009) solar abundances in the troposphere. At Saturn, the elemental abundances for nitrogen were 2-4 × solar, and phosphorus was 15.9 × solar in the troposphere. The elemental abundances at Uranus in the troposphere were found to be less enriched than at Jupiter and Saturn. Solar System formation theory requires that Uranus be more enriched than the gas giants. Using the results from Chapter 3, the

elemental abundance at Uranus can be compared to Jupiter's. On Uranus, nitrogen was depleted when compared to solar and when compared to the gas giants. The elemental abundance of oxygen was found to be greater than on Jupiter, however, the true measurement of oxygen is not known as the Galileo probe went through a hot spot (Niemann *et al.*, 1998a). Sulfur and phosphorus' elemental abundances were approximately the same as on the gas giants. As none of the species were definitively found to be more enriched than the species at the gas giants, a deep sink is likely.

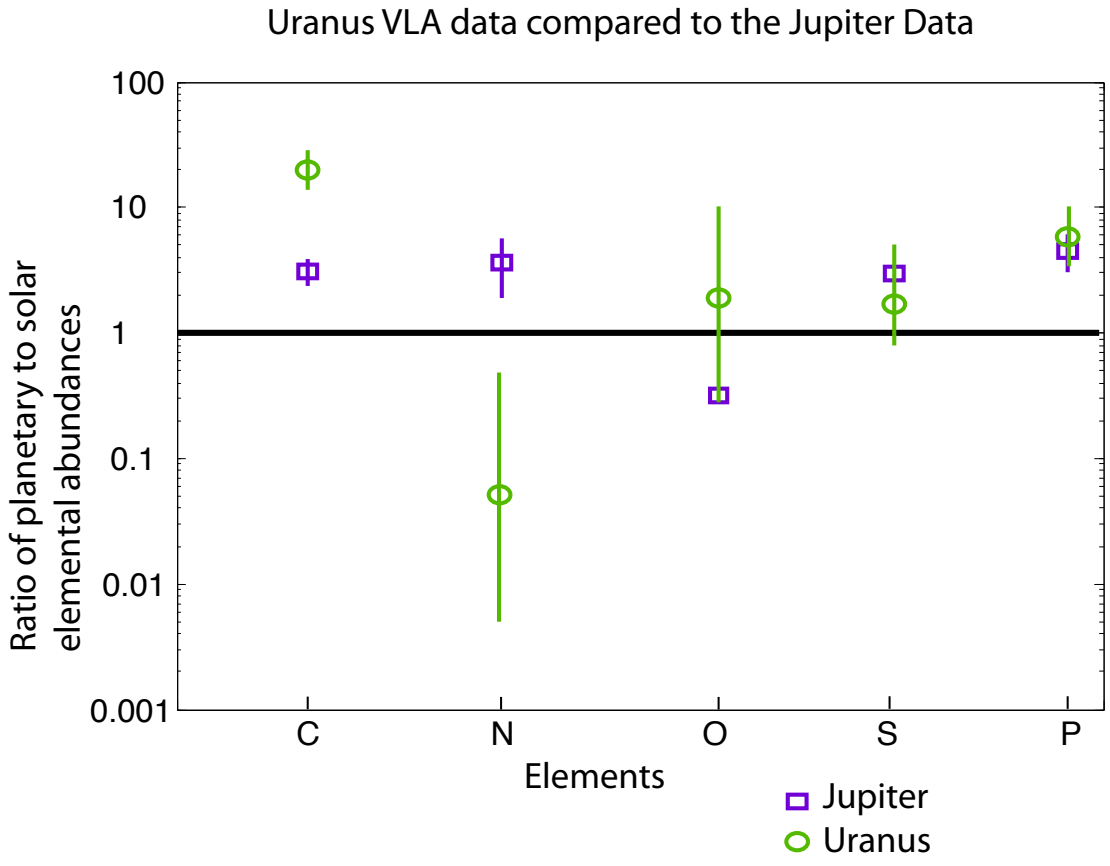

Figure 4.5 This figure represents a comparison between Jupiter measurements and Uranus data. The nitrogen, oxygen, sulfur, and phosphorus show the range of abundances inferred from radio data. Note the Uranus elemental abundances are comparable or less than that found for Jupiter, which points to a likely deep sink.

4.4 Fitting the Interior of Uranus

In Chapter 3, it was seen that the 21.2 cm wavelength was a difficult point to fit. Figure 3.11 shows the weighting functions for our best fit atmosphere. The two biggest controls on the 21 cm weighting function were ammonia and water. The weighting function of the 21.2 cm wavelength for case 6, the only case that fits this wavelength, is shown in Figure 4.6. This figure shows the weighting function and the opacities of each species. As expected, the opacity of phosphine and hydrogen sulfide has little influence. Ammonia's opacity is the dominant contributor in the first 90 bar of the atmosphere, and the water opacity is dominant below that point. The cloud base of the ammonia-water cloud is approximately 90 bar for this case, which explains the transition from a water dominant opacity to an ammonia dominated opacity. At 25.1 bar, the ammonia hydrogen sulfide cloud base is reached. The weighting function experiences a rapid drop off at this point. The weighting function peaks in the 90 to 25 bar region.

Case 6 has the second most nitrogen of any of the statistically significant fits, with nitrogen being 0.4 × solar. Oxygen, in this case, falls in the middle of the range of statistically significant fits, as it is enriched to 1 × solar. To fit the deeper 21.2 cm data point, more opacity from ammonia appears to be needed. This could signify that the ammonia-water solution may not be properly accounted for in the radiative transfer code, or that there is another source of opacity that is not being accounted for, such as carbon monoxide. There is opacity structure seen in the disk in this wavelength that has not been accounted for in the model. Furthermore, observation at this wavelength have the greatest uncertainty of any of the wavelengths examined. Unfortunately, at this time this is the only fit found for this point and, therefore, more cannot be said about this region.

Another possible solution is that there is a liquid ocean at this depth that is providing the observed opacity.

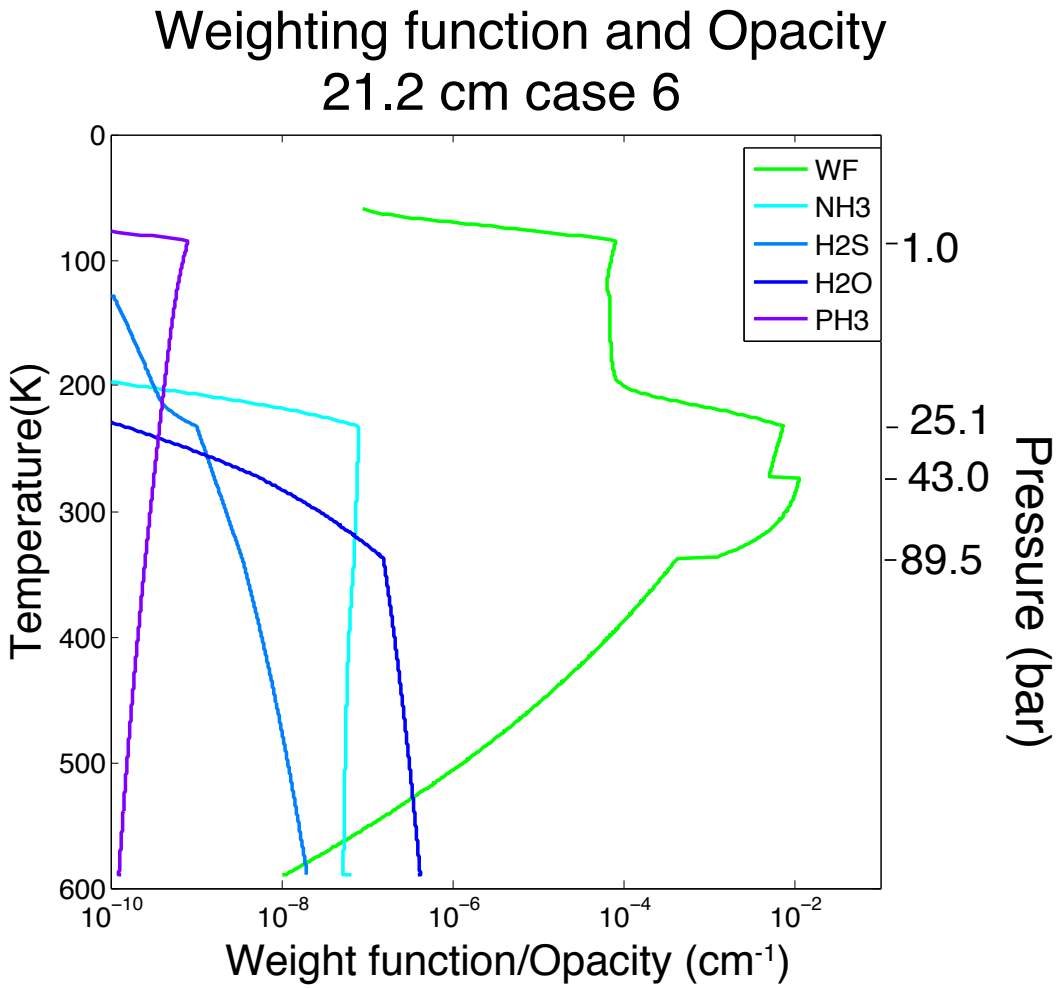

Figure 4.6 Weighting function of the 21.2 cm data point for case 6 is shown here, the only case to match this point. The opacities of the individual species are also displayed here. The deep 21.2 cm data point peak weighting function corresponds to the water cloud base.

A water ice reservoir is speculated to exist on Uranus and Neptune. Wiktorowicz and Ingersoll (2007) examined if an actual liquid water-hydrogen ocean could exist on Neptune at pressures less than ~20 kbar and temperatures less than ~800 K, and found

that Neptune had a 13% chance of having a liquid water ocean. They also speculated that in the future, after the Sun is a white dwarf, Neptune could cool enough to allow a liquid water ocean to exist. A temperature-entropy diagram for pure water identified the critical temperature for forming an ocean as 647 K. The authors acknowledged that the temperature-entropy curve is dependent on the composition of Neptune, therefore, the wrong composition results in the wrong critical temperature. A moist adiabat is assumed to descend from the upper atmosphere into the deeper atmosphere. This assumption is valid, as long as Neptune is divided into only a few layers, core, molecular envelope etc. If more layers are added, the adiabatic approximation fails (Hubbard *et al.*, 1995). The moist adiabat contains a gas and a condensed phase adiabat. A cloud base results if the gas phase adiabat reaches the deep interior-mixing ratio before the condensed phase adiabat. An ocean surface results if the condensed phase reaches the deep interior mixing ratio first.

Neptune is too dry for a deep-liquid water ocean, and instead allows a water cloud to form. Therefore, when there is not an ocean, there is still the possibility of a cloud. When a solar mixing ratio of oxygen is assumed in the deep interior with a mole fraction of 26.9%, a cloud base was formed at 10.7 kbar and 663 K. With less oxygen and a mole fraction of 17.4%, they formed a cloud base at 5.0 kbar and 623 K. This shows that if there is a lack of oxygen in the upper atmosphere of the ice giants, then a deep oxygen cloud at the kbar level is a possible sink of the water.

4.5 Conclusions about the Interiors

At this time, no conclusions about the interiors of the ice giants can be made. It can be stated that something is responsible for the generation of the magnetic field observed at these planets. The likely candidates are an ionic ocean or metallic water, but measurement of the interior are not possible to confirm either candidate. Liquid ocean water cannot exist at the current temperature inside the ice giants. Simulations have been performed to ascertain the phase of ammonia and water inside of the ice giants, but there are many uncertainties in these measurements making it difficult to determine if an ionic ocean exists and at what temperature and pressure levels it would be located. The tropospheric abundance can provide hints to understanding the interiors. With the volatiles in the troposphere found to be less enriched than expected, a deep sink is more likely to occur. At this time, nothing definitive can be said about the interiors of these planets.

Chapter 5 : CONCLUSIONS

5.1 Conclusions

The crux of this work dealt with solving two questions. The first question explored was understanding the effects of precipitation on the concentrations of the clouds. The second question explored was the addition of the phosphine cloud to the ECCM and radiative transfer code, and what can be learned about the atmosphere using this model and the radio data.

Cloud precipitation was examined at Jupiter and Earth. The method of Ackerman and Marley (2001) was used at Jupiter and Earth, as it provided a relationship between the upward motion and downward transport of the condensables via precipitation. This method was applied to Earth to validate it. Using the Ackerman and Marley approach the cloud's densities at Earth decreased by an order of magnitude from the standard lifting condensation model. Column abundances were calculated for both Earth with and without precipitation and were compared to the data. It was found that the Ackerman and Marley adapted ECCM fell within the range of the Earth data, while

the standard ECCM overestimated the value. The Ackerman and Marley formulation was then applied to Jupiter. Since the eddy diffusion coefficient is not known at this planet, a wide variety of potential eddy diffusion coefficients were used. Cloud densities were found to vary by a factor of 1.5 to 300 based on the eddy diffusion coefficient. The cloud densities from the ECCM are currently being overestimated, and the actual cloud densities should be 1 to 3 orders of magnitude less due to precipitation and dynamics in the atmosphere. Using Rossow (1978), the lifetime of a water cloud droplet, once it reaches the size of a rain droplet, in a cloud was found to be approximately three hours. The maximum precipitation rate was calculated between 8.6×10^{-8} and 1.2×10^{-4} g cm^{-2} s^{-1}, depending on the amount of water present and the updraft velocity.

Phosphine was added to both a radiative transfer model and the ECCM. Depending on phosphine's concentration, it condensed in both Uranus and Neptune in the upper 2 bar of the tropospheres. This was determined using a new vapor pressure equation for phosphine, which was derived using laboratory data collected at lower temperatures and pressures then were previously used which more accurately represents what is observed in the upper tropospheres of the ice giants. The opacity of phosphine had an effect on the radio wavelengths; therefore, it needed to be added to the radiative transfer code presented in Hofstadter and Butler (2003). The radiative transfer code was coupled with the ECCM, and runs were performed to match recent VLA & SMA data from 2005-2009. Constraints were placed on the location of clouds and the concentration of phosphine was considered. It was found that only one of the solutions did not contain a phosphine cloud and that solution was not statistically significant. The model types that resulted matched a variety of solutions for the interiors of the ice giants. Comparing our radio data to the model, a variety of solutions were found that could explain the two-

cloud solution proposed by Baines *et al.* (1995). No solutions were found that explained the two-cloud solution proposed by Sromovsky and Fry (2006). Seven different categories of fits were found. One of the cases was not statistically significant. Only one fit matched the 21.2 cm data point. This indicates that this fit is correct, or there is an unaccounted source for opacity deep in the atmosphere that needs further study. At this time, only a range of the elemental abundances in the upper troposphere were possible: phosphorus of 4 to 10 × solar, nitrogen of 0.008 to 0.6 × solar, oxygen of 0 to 10 × solar, and sulfur of 0.5 to 4 × solar-however. However, with the new VLA set-up and the completion of the Atacama Large Millimeter Array, more data and constraints should be available in the future.

5.2 Future Work

There are a few additional measurements that would aid in understanding the clouds on the giant planets. The first important measurement that will hopefully be obtained by the Juno spacecraft, currently in route to Jupiter, is the elemental abundance of oxygen. This is crucial to determining the formation scenario of the Solar System. Furthermore, obtaining this value at the other giant planets will provide additional data to expand our knowledge of Solar System formation. In the case of the ice giants, this can also inform about the interiors of these planets and aid in determining where the magnetic field is being generated, as discussed in Chapter 4.

The eddy diffusion coefficient is necessary to determine cloud precipitation. Currently, we have to use a range of eddy diffusion coefficients for the Ackerman and Marley (2001) calculation. A more accurate value for the eddy diffusion coefficient will

aid in understanding the actual density of the clouds. Modeling and measurements are needed to understand the dynamics in the atmospheres of the giant planets. Models such as the Explicit Planetary Isentropic Coordinate Model have incorporated the microphysics of water and ammonia clouds in their general circulations model (Palotai and Dowling, 2008). This model, however, still has a lot of assumptions. The Community Aerosol and Radiation Model for Atmosphere out of Boulder, Colorado can simulate the aerosol life cycle, including nucleation, condensation, coagulation, and deposition (Toon *et al.*, 1979; Turco *et al.*, 1979; Toon *et al.*, 1988). This model has been used for both 1-D and 3-D simulations on Earth. This model has been used to calculate the organic aerosols on Titian (Toon *et al.*, 1992), sulfuric acid clouds on Venus (James *et al.*, 1997), ice clouds on Mars (Michelangeli *et al.*, 1993; Colaprete *et al.*, 1999), and Martian dust storms (Murphy *et al.*, 1995). It could potentially be adapted to model the clouds on the giant planets. The final potential model that could be adapted to the giant planets is the Weather Researching and Forecasting model (WRF) which is a meso/microscale model used to forecast weather on Earth. This model has been updated to include a Martian General Circulation Model that was based off of the original WRF model. This model could be adapted further to be used for studies at the giant planets. The main issue with adapting any model to the giant planets is that there are more unknowns. Appropriate assumptions must be made until more data is available for these planets.

The influence the precipitation has on the lapse rate needs to be examined further. Our model is just a static model, and thus cannot properly determine the effect that water cycling will have on the lapse rate. Currently, all of the water is either used in the cloud or is used to scale down the cloud density as in the Ackerman and Marley

model. In an actual cloud, the water will precipitate and fall a certain distance before re-evaporating. Once it returns to a gaseous form, it may then be brought back up to the cloud level by dynamics, such as an updraft, where it can condense again. When it evaporates it will release heat just as it does when it condenses. This will change the temperature structure of the atmosphere, but until we better understand the precipitation and dynamics, we cannot know how this will actually change the system.

A few improvements can be made in the radio data and radiative transfer model. More data at different wavelengths would allow more constraints on the atmosphere, and would help limit the number of solutions. Furthermore, more accurate opacity measurements of the atmosphere's gases at the pressure and temperature regimes on these planets would improve the accuracy of the models. This becomes especially important when determining what is responsible for the opacity at 21.2 cm, as almost all of the model fits had warmer brightness temperature than the observations. When the temperature is too high, it means we are seeing deeper in the atmosphere and more absorbers need to be present. The addition of other constituents' opacities that have been observed in the atmospheres, such as carbon monoxide, may aid the interpretation. While we mainly focused on the clouds, other species in the atmosphere can have an effect on the radio data and thus must be included. However, to do this, not only does the opacity need to be known, but we also must know the concentration of the species.

The new Herschel Space Observatory, launched in 2009, collects data in the far infrared and sub millimeter wavebands that can be used to learn more about the ice giants. The Atacama Large Millimeter/sub-millimeter Array (ALMA) located in the desert of northern Chile, will become important in the coming years once it is completed. ALMA performed some observations in late 2011, but should be fully operational by the

end of 2012. The data from Herschel and ALMA will better constrain these atmospheres, and allow us to more accurately model these planets. The VLA recently has undergone improvements, which boast sensitivity improvement of 5 to 20 at all wavelength and will hopefully help better constrain the atmosphere of Uranus in the coming years.

5.3 Suggestions for Future Missions

Data from the ice giants is limited, as the ground- and space-based telescopes can only see into the upper troposphere of these planets. The only mission that visited these planets was Voyager 2, and it was not instrumented to obtain deep atmospheric data at these planets. Thus, we only have a range of elemental enrichments for carbon abundances in the atmosphere. A probe/orbiter mission to one or both of the ice giants is necessary to increase our understanding of these planets. This probe must be able to observe the elemental abundances of the condensables – nitrogen, carbon, phosphorus, sulfur, and oxygen– along with the elemental abundances of the noble gases present in the atmosphere. Further, the D/H ratio could be used to tell in what form the ices arrived at the ice giants, and thus constraint formation models. Basic meteorology should be examined as well, including, but not limited to, the temperature and pressure profile and the zonal and vertical wind speeds. The orbiter should contain some type of radiometer, similar to the microwave radiometer that is present on Juno, so we can confirm the elemental abundances found by the probe, and determine if the planet's atmosphere is well mixed. Figure 5.1 shows the weighting function for a purely water atmosphere at Uranus using several different wavelengths – 0.14, 0.7, 2.0, 6.0, 21.2, and

50 cm. All of these wavelengths are available with the SMA or the VLA except for 50 cm. The 50 cm weighting function peaks near 175 bar, but its wings extend much deeper in the atmosphere. If this wavelength could be obtained using a microwave radiometer it would aid in our understanding of the amount of oxygen present at Uranus.

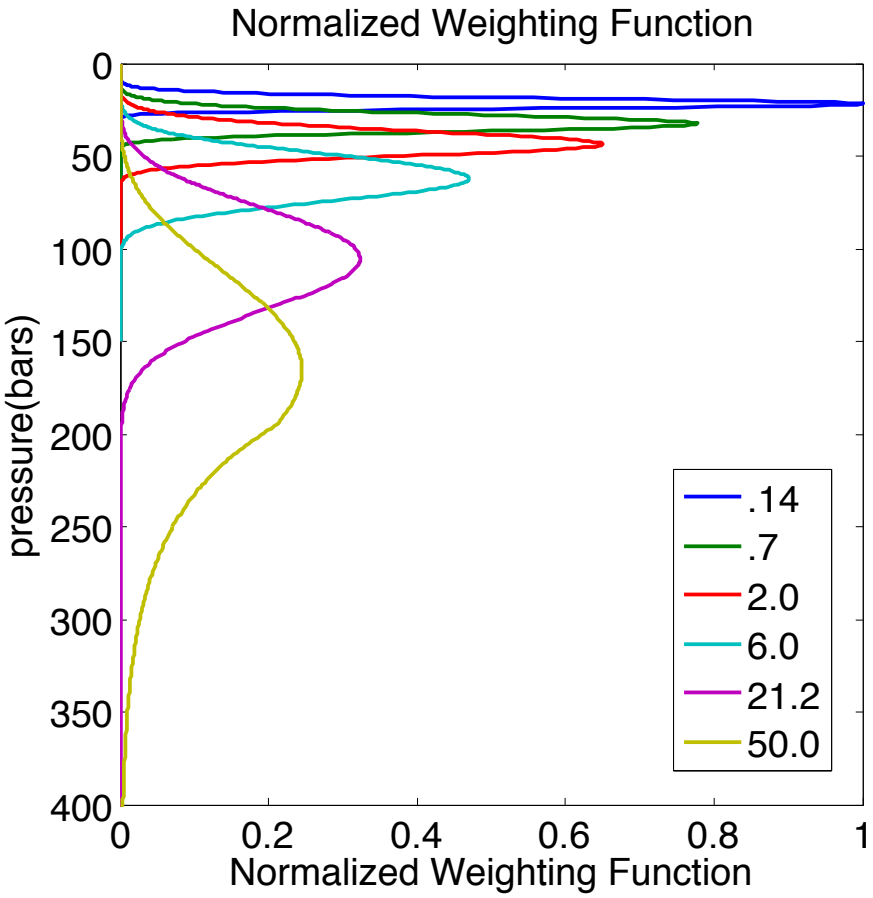

Figure 5.1 Weighting functions for a pure 10 × solar oxygen atmosphere at wavelengths of 0.14, 0.7, 2.0, 6.0, 21.2 and 50 cm. 50 cm is not currently measured by the VLA/SMA, but is similar to the wavelength of the microwave radiometer on JUNO. Even using 50 cm, we do not see to the level of ionic ocean (kilobars).

The interiors of the ice giants need further examination. The gravitational moments should be examined again, similar to what was measured by Voyager 2, so that we can better constrain the density profiles inside the planets. The magnetic field would also need to be reexamined to determine its strength and the location of the dipole. It was previously found to be both offset from the axis and off center of the planet at Uranus. This is just a short list of what should be included in a mission to Uranus, and what measurements would be useful in understanding this unique planet. Any mission to Uranus or Neptune would greatly increase our scientific knowledge.

5.4 Broader Impact

The giant planets sometimes seem like a strange area to investigate, as we will never be able to live on any of them. However, these planets hold the key to understanding the formation of the Solar System, and therefore are worth being studied. By studying the clouds and the atmosphere's of the giant planets we learn about the elemental abundances inside of these planets, which are one of the constraints used when evaluating Solar System formation theories. Understanding these planets can also help the expanding field of exoplanets and identifying solar systems like our own. While we may never live on any of these planets, they can tell us how we were able to live at all.

APPENDICES

APPENDIX A: NUMERIC METHOD OF ECCM

A.1 Lapse Rate

An ideal gas undergoing adiabatic expansion would give from the first law of thermodynamics:

$$\overline{C}_p dT - vdp + \sum_k \lambda_k dX_k = 0 \qquad \text{A.1}$$

where C_p is the mean molar heat capacity at constant pressure, dT is the differential change in absolute temperature, v is the molar volume, dP is the differential change in total pressure, λ_k is the molar enthalpy of condensation of the k^{th} gas, dX_k is the differential change in the number of moles of the k^{th} gas due to condensation.

Working with the third term of equation (A.1) and assuming an ideal mixture yields:

$$X_k = P_k/P \qquad \text{A.2}$$

where P_k is the partial pressure of gas k and P is the atmospheric pressure. Equation (A.1) results from the first law of thermodynamics where, Q is heat, and U is the internal energy:

$$dU = dQ - Pdv$$

$$\text{or } dQ = dU + Pdv \qquad \text{A.3}$$

but including enthalpy, H:

$$H = U + Pv \qquad \text{A.4a}$$

And differentiating:

$$dH = dU + Pdv + vdP \quad \text{A.4b}$$

Rearranging (A.4b) to create an expression for dU and substituting into equation (3):

$$dQ = dH - vdP \quad \text{A.5}$$

But differentiating enthalpy can also be defined as:

$$dH = C_p dT \quad \text{A.6}$$

Substituting equation (A.6) into (A.5) results in:

$$dQ = C_p dT - vdP \quad \text{A.7}$$

If one or more of the gases is condensing, then dH must also have a latent heat term:

$$\sum \lambda_k dX_k \quad \text{A.8}$$

where λ_k is the molar enthalpy of condensation of kth gas, also latent heat of condensation. Thus, for condensation, equation (A.7) becomes:

$$dQ = \overline{C}_p dT - vdP + \sum_k \lambda_k dX_k = 0 \quad \text{A.9}$$

for an adiabatic process. Where X_k is the same as equation (A.2). Next, an equation for the lapse rate, dT/dz, needs to be found. dP can be expressed in terms of dz using the hydrostatic equation:

$$\frac{dP}{P} = \frac{-g\mu dz}{nkT} \quad \text{A.10}$$

where m is the mass of a hydrogen atom which equals 1/N, N is the Avogadro's number, and μ is the mean molecular weight. Knowing that the ideal gas constant is equal to the Boltzmann constant and the Avogadro's number:

$$\frac{dP}{P} = \frac{g\mu dz}{(Nk)T} = -\frac{g\mu dz}{RT} \quad \text{A.11}$$

Differentiating equation (A.2) yields:

$$dX_k = \frac{dP_k}{P} - \frac{P_k}{P^2}dP \qquad \text{A.12}$$

From the Clausius-Clapeyron equation for the kth component, the vapor pressure is:

$$\frac{dP_k}{dT} = \frac{\lambda_k}{T\Delta v_k} \approx \frac{\lambda_k}{Tv_k} \qquad \text{A.13}$$

Taking equation (A.13) and substituting the ideal gas law for v:

$$dP_k = \frac{\lambda_k}{Tv_k}dT = \frac{\lambda_k}{T\left(\frac{RT}{P_k}\right)}dT = P_k\frac{\lambda_k dT}{RT^2} \qquad \text{A.14}$$

Rearranging equation (A.14):

$$\frac{dP_k}{P_k} = \frac{\lambda_k dT}{RT^2} \qquad \text{A.15}$$

By rearranging equation (A.12) and substituting equations (A.15) and (A.11):

$$dX = \frac{P_k}{P}\left(\frac{dP_k}{P} - \frac{dP}{P}\right) = X_k\left(\frac{\lambda_k dT}{RT^2} + \frac{g\mu}{RT}dz\right) \qquad \text{A.16}$$

Substituting equations (A.16) and (A.11) into equation (A.9) gives:

$$\text{dQ} = 0 = \overline{C}_p dT - v\left[-P\frac{\mu g}{RT}dz\right] + \sum_k \lambda_k\left[X_k\left(\frac{\lambda_k dT}{RT^2} + \frac{\mu g}{RT}dz\right)\right] \qquad \text{A.17a}$$

Combining like terms:

$$0 = dT\left[\overline{C}_p + \sum_k \frac{\lambda_k^2 X_k}{RT^2}\right] + dz\left[\left(\frac{Pv}{RT}\right)\mu g + \sum_k X_k\frac{\mu g}{RT}\lambda_k\right] \qquad \text{A.17b}$$

and using the fact that Pv/RT= 1 yields:

$$\frac{dT}{dz} = -\frac{\mu g}{\overline{C}_p}dT\frac{\left[1 + \sum_k \frac{\lambda_k X_k}{RT^2}\right]}{\left[1 + \sum_k \frac{\lambda_k^2 X_k}{\overline{C}_p RT^2}\right]} \qquad \text{A.18}$$

In equation (A.18), the condensation resulting because of the reaction of H_2S (g) with NH_3 (g) can also be included. This is not a condensation in the true sense of the word, but a chemical reaction leading to a change of phase of NH_4SH. To include it, the starting expression for energy should read as:

$$dQ=0= \overline{C}_p dT - vdP + \sum_k \lambda_k dX_k + \lambda_{R_X} dX_{H_2S} \qquad \text{A.19}$$

where λ_{R_X} is the molar heat of reaction, $NH_3(g) + H_2S(g) \rightarrow NH_4SH$ (s), and dX_{H_2S} is the differential change in the number of moles of H_2S due to condensation, i.e. on reaction with NH_3,

$$NH_3(g) + H_2S(g) \xrightarrow{K_p} NH_4SH\ (s) \qquad \text{A.20}$$

The equilibrium rate constant for this reaction is given by:

$$K_p = P_{NH_3} \bullet P_{H_2S} \qquad \text{A.21}$$

With P in atmospheres and T in °K, and from International Critical Tables:

$$\log_{10} K_p = 14.82 - \frac{4705}{T} \qquad \text{A.22}$$

Taking log of equation (A.21) gives:

$$\log_{10} K_p = \log_{10}(P_{NH_3} \bullet P_{H_2S}) = 14.82 - \frac{4705}{T} \qquad \text{A.23}$$

and in terms of ln:

$$\ln(P_{NH_3} \bullet P_{H_2S}) = 2.3026\left(14.82 - \frac{4705}{T}\right) \qquad \text{A.24a}$$

Knowing:

$$P_{H_2S} = P \bullet X_{H_2S}$$

$$P_{NH_3} = P \bullet X_{NH_3} \qquad \text{A.24b}$$

so that equation (A.24B) becomes:

$$\ln(P^2 \bullet X_{NH_3} \bullet X_{H_2S}) = 2.3026\left(14.82 - \frac{10833}{T}\right) \qquad \text{A.25}$$

Since we are after the terms dX_{H_2S} in equation (A.18), we differentiate equation (A.25):

$$\frac{(2PdP)X_{NH_3} \cdot X_{H_2S} + P^2(X_{NH_3}dX_{NH_3} + X_{H_2S}dX_{H_2S})}{P^2(X_{NH_3} \cdot X_{H_2S})} = \frac{10833}{T^2}dT \qquad \text{A.26}$$

But in a mixed atmosphere, the rate of change of concentrations of all species is the same, so that:

$$dX_{NH_3} = dX_{H_2S} \qquad \text{A.27}$$

Applying equation (A.27) and rearranging equation (A.26):

$$dX_{H_2S} = \left(\frac{10833}{T^2}dT - 2\frac{dP}{P}\right)\frac{X_{NH_3} \cdot X_{H_2S}}{X_{NH_3} + X_{H_2S}} \qquad \text{A.28}$$

But from equation (A.11):

$$dX_{H_2S} = \left(\frac{10833}{T^2}dT - 2\frac{\mu g}{RT}\right)\frac{X_{NH_3} \cdot X_{H_2S}}{X_{NH_3} + X_{H_2S}} \qquad \text{A.29}$$

substituting equation (A.29) in equation (A.18) gives, and using equation (16B):

$$\text{dQ=0} = dt\left[C_p + \frac{\sum_k \lambda_k^2 X_k}{RT^2}\right] + dz\left[\mu g + \sum_k X_k \lambda_k \frac{\mu g}{RT}\right] + \qquad \text{A.30}$$

$$\lambda_{R_x}\left(\frac{10833}{T^2}dT\right)\frac{X_{NH_3} \cdot X_{H_2S}}{X_{NH_3} + X_{H_2S}} + \lambda_{R_x}\frac{X_{NH_3} \cdot X_{H_2S}}{X_{NH_3} + X_{H_2S}}dz$$

However, another term is needed to take into account the energy released by the conversion of ortho H_2, which has a parallel proton spin, to para H_2, which has anti parallel proton spin. At high temperatures, $T \geq 400K$, the ortho to para ratio is 3/1. If, however, thermodynamic equilibrium is maintained the para H_2 fraction will increase as

the temperature drops at the expense of the ortho fraction. The ortho to para conversion is accompanied by a release of latent heat, $\lambda_{o\to p}$. The heat capacity of H_2 is also a function of temperature and that has to be taken into account. For every ortho H_2 that disappears due to the changing temperature a molecule of para H_2 is created, thus:

$$dX_{o\to p} = f_{H_2}\frac{dX_o}{dT}dT \qquad \text{A.31}$$

where dX_o/dT is the differential change in the fractional part of ortho H_2 with temperature, and f_{H_2} is the volume mixing ratio, a constant. Using Massie and Hunten (Hunten), X_o as a function of temperature is:

$$X_o = \frac{Z_{odd}}{Z_{odd} + Z_{even}} \qquad \text{A.32}$$

where:

$$Z_{odd} = \sum_{oddJ}^{\infty} d(J)\exp\left[\frac{-hc}{KT}F(J)\right] \qquad \text{A.33a}$$

$$Z_{even} = \sum_{evenJ}^{\infty} d(J)\exp\left[\frac{hc}{KT}F(J)\right] \qquad \text{A.33b}$$

$$d(J) = 3(2J+1)J_{odd}$$
$$d(J) = (2J+1)J_{even}$$
$$F(J) = 59.322J(J+1) - 4.71e-2*(J(J+1))^2 \qquad \text{A.33c}$$

Z is the partition function, d(J) are the degeneracies for the state, the ortho state is a triplet while the para state is a singlet, J is the rotational quantum number, F(J) the energy for J^{th} rotation level, hydrogen is assumed to be in the ground vibrational level, h is Planck's constant, k is Boltzmann's constant, and c is the speeding of light. Making:

$$y = \frac{hcF(J)}{kT} \qquad \text{A.34}$$

and applying the definitions in equation (A.33) to equation (A.32):

$$X_o = \frac{\sum_{oddJ}^{\infty} d(J)e^{-y}}{\sum_{evenJ}^{\infty} d(J)e^{-y}} \qquad \text{A.35}$$

Differentiating yields:

$$\frac{dX_o}{dT} = S = \frac{Z_{even}\sum_{oddJ}^{\infty} d(J)\frac{y}{T}e^{-y} - Z_{odd}\sum_{evenJ}^{\infty} d(J)\frac{y}{T}e^{-y} -}{(Z_{even} + Z_{odd})^2} \qquad \text{A.36}$$

thus:

$$\lambda_{o\to p} dX_{o\to p} = \lambda_{o\to p} f_{H_2} S dT \qquad \text{A.37}$$

Adding the new term to equation (A.30) and solving for the lapse rate yields:

$$\frac{dT}{dz} = \frac{-mg}{C_p}\left\{\frac{1 + \frac{1}{RT}\left[\sum_k L_k X_k + \frac{2L_{RX}(X_{H_2S} * X_{NH_3})}{(X_{H_2S} + X_{NH_3})}\right]}{1 + \frac{1}{C_p T^2}\left[\sum_k L_k^2 X_k + \frac{10844(X_{H_2S} * X_{NH_3})}{X_{H_2S} + X_{NH_3}} + \frac{L_{o\to p} S f_{H_2}}{C_p}\right]}\right\} \qquad \text{A.38}$$

A.2 Solution Cloud

In Uranus and Neptune (and, to some extent, Saturn also), a solution cloud of NH_3 in H_2O may form, beginning deep in the atmosphere. If the concentration of the solution is C in NH_3 on condensation, then 1-C moles of H_2O would condense, i.e.:

$$dX_{solution} = \frac{dX_{H_2O}}{1 - C} \qquad \text{A.39}$$

The L_kX_k term should reflect the heat due to condensation in the solution:

$$\frac{L_s dX_{H_2O}}{1-C} \qquad \text{A.40}$$

where L_s is the average heat of condensation of the solution. This will affect the lapse rate in equation (A.38), and consequently the atmospheric temperature.

The heat capacity of H_2, Cp_{H2}, is dependent on the ortho-para H_2 conversion, which is temperature sensitive. Therefore the ratio of ortho-para affects Cp_{H2} and thus affects the lapse rate. Cp_{H2} is a function of temperature and must be calculated from the partition function:

$$\begin{aligned} C_{p_{H_2}} &= \frac{5}{2}R + \frac{dU}{dT} \\ U &= \frac{RT^2}{Z} * \frac{dZ}{dT} \end{aligned} \qquad \text{A.41}$$

(Massie and Hunten), where U is the internal energy of the H_2 molecule and the summation for Z is over all J. Applying these two equations to each other yields:

$$C_{p_{H_2}} = R\left[\frac{5}{2} + \frac{T^2 d^2T}{z dT} + \frac{2T dT}{z dz} - \frac{T^2}{Z^2}\left(\frac{dT}{dZ}\right)^2\right] \qquad \text{A.42}$$

Expressing equation (A.42) in summation notation and simplifying gives:

$$C_{p_{H_2}} = R\left[\frac{5}{2} + \frac{\sum_{allJ}^{\infty} d(J) y^2 e^{-y}}{z} - \left(\frac{\sum_{allJ}^{\infty} d(J) y\ e^{-y}}{z}\right)^2\right] \qquad \text{A.43}$$

A.3 Calculation of Cloud Density

The calculation of the cloud density has evolved since the creation of the ECCM. To determine the cloud density, start by expressing the condition of hydrostatic equilibrium:

$$M^j = \frac{P^j}{g} \qquad \text{A.44}$$

where M^j is the mass per unit area of the atmosphere above level j and P^j is the pressure at level j. For a single constituent k, its mass per unit area in the atmosphere above j is:

$$M_k^j = w_k^j M^j \qquad \text{A.45}$$

where w_k^j is the weight fraction in the atmosphere. The average cloud density, D, between the levels I and j due to the condensing species k is:

$$D = (w_k^i - w_k^j)\frac{M}{dz} \qquad \text{A.46}$$

where M is the average mass per unit area in the condensing layer. Rewriting in terms of the mole fraction and pressure:

$$D = \frac{m_k(X_k^i - X_k^j)dp}{mgdz} \qquad \text{A.47}$$

where m_k is the molecular weight of the k^{th} constituent. When more than one species is condensing to form a cloud, the right hand side of equation (A.47) is summed over the condensing species. Equation A.47 results in an upper limit of the cloud density.

APPENDIX B: VARIABLES AND ACRONYMS

B.1 Variables

a Measure of attraction between molecules

a_s Absorption

A Area

A_j Absorption at the line center

b Volume excluded by molecules

b_w Wien's displacement constant

B diameter of the Gaussian convolving kernel

B_v Planck's Law

c Speed of light

c_s Speed of sound

C_p Specific heat

e_s Saturated vapor pressure

E_v Energy

f Voltage distribution in the atmosphere

f_{rain} Mass-weighted droplet precipitation velocity to w_*

F Heat flux

F(l,m) Flux Density

Ft Fourier transform

$\mathbf{F_v}$ Monochromatic flux

$\mathbf{F_{vvw}}$ Van Vleck Weisskopf lineshape

$\mathbf{g}$ Gravity

$\mathbf{G}$ Gravitational Constant

$\mathbf{H}$ Scale Height

$\mathbf{I}$ Observed radiation

$\mathbf{I_v}$ Monochromatic intensity

$\mathbf{k_B}$ Boltzmann Constant

$\mathbf{K}$ Eddy diffusion coefficient

$\mathbf{Kn}$ Knudsen number

$\mathbf{L}$ Ratio in mixture of Hydrogen to Helium

$\mathbf{L_{H2}}$ Pure mixture of Hydrogen

$\mathbf{L_{He}}$ Pure mixture of Helium

$\mathbf{L_m}$ Turbulent mixing length

$\mathbf{m}$ Mass of atmosphere

$\mathbf{n}$ Number of moles

$\mathbf{n_d}$ Number density

$\mathbf{Na}$ Avogadro's number

$\mathbf{P}$ Pressure

$\mathbf{q_c}$ Condensate mixing ratio

$\mathbf{q_s}$ Saturated mixing ratio

$\mathbf{q_t}$ Total mixing ratio

$\mathbf{q_v}$ Vapor mixing ratio

$\mathbf{q_w}$ Total mixing ratio

$\mathbf{Q_{H2}}$ Hydrogen cross section

$\mathbf{Q_{He}}$ Helium cross section

$\mathbf{Q_{H2\text{-}He}}$ Hydrogen-Helium cross section

r Particle radius

R Ideal gas constant

Re Reynolds number

$\mathbf{S_j}$ Intensity of line

t Transmittance

T Temperature

$\mathbf{T_B}$ Brightness Temperature

v Particle velocity

$\mathbf{v_{fall}}$ Terminal velocity

V Volume of the container

w* Convective velocity scale

W Weighting function

$\mathbf{X_w}$ Mixing ratio of water

z Height

$\boldsymbol{\alpha}$ Specific Volume

$\boldsymbol{\alpha_1}$ Absorption from collision broadened gas

$\boldsymbol{\Gamma_d}$ Dry lapse rate

$\boldsymbol{\Gamma_m}$ Moist lapse rate

ε The dimensionless ratio of the specific gas constant of dry air to the specific gas constant for water vapor

η_{H2} Dynamic viscosity of hydrogen

η Dynamic viscosity

η_{He} Dynamic viscosity of helium

θ Potential temperature

θ_e Equivalent potential temperature

κ Epicycle frequency

λ Wavelength

λ_m Mean free path

λ_{max} Wien's displacement law

λ_v Latent Heat

Λ Minimum Scaling

μ Mean molecular mass

π Pi

ρ Density

ρ_a Density of atmosphere

ρ_{cond} Mass density of condensate

ρ_e Density of the environment

ρ_g Gas density

ρ_p Density of the parcel

σ Surface density

σ_s Stefan-Boltzmann

τ	Optical depth
τ_{fall}	Precipitation time constant
υ	Frequency
Ω	Solid angle

B.2 Acronyms

AM	Ackerman and Marley 2001
CCN	Cloud Condensation Nuclei
CIRS	Composite Infrared Spectrometer
ECCM	Equilibrium Cloud Condensation Model
GPMS	Galileo Probe Mass Spectrometer
IRIS	Infrared Interferometer Spectrometer
ISO	Infrared Space Observatory
IUE	International Ultraviolet Explorer
SMA	Submillimeter Array
UVS	Ultraviolet Spectrometer
VLA	Very Large Array

REFERENCES

REFERENCES

Abraham, F. F. (1970). Functional dependence of drag coefficients of a sphere on Reynolds number *Phys. Fluids*, *13*, 2194-2195.

Ackerman, A. S., and M. S. Marley (2001). Precipitating condensation clouds in substellar atmospheres. *Astrophys J*, *556*, 2, 872-884.

Alibert, Y., O. Mousis, and W. Benz (2005). Modeling the Jovian subnebula - I. Thermodynamic conditions and migration of proto-satellites. *Astron Astrophys*, *439*, 3, 1205-1213.

Amelin, Y., A. N. Krot, I. D. Hutcheon, and A. A. Ulyanov (2002). Lead isotopic ages of chondrules and calcium-aluminum-rich inclusions. *Science*, *297*, 5587, 1678-1683.

Appleby, J. F. (1986). Radiative-convection equilibrium models of Uranus and Neptune. *Icarus*, *65*, 383-405.

Asplund, M., N. Grevesse, A. J. Sauval, and P. Scott (2009). The Chemical Composition of the Sun. *Annual Review of Astronomy and Astrophysics, Vol 47*, *47*, 481-522.

Atreya, S. K. (1986). Atmospheres and ionospheres of the outer planets and their satellites. *Berlin and New York, Springer-Verlag*, *15*.

Atreya, S. K. (2011), Atmospheric Moons Galileo Would Have Loved, in *Galileo's Medicean Moons Their Impact on 400 Years of Discovery*, edited by C. Barbieri, pp. 130-140, Cambridge University Press.

Atreya, S. K., and T. M. Donahue (1979). Models of the Jovian upper-atmosphere. *Rev Geophys*, *17*, 3, 388-396.

Atreya, S. K., and T. M. Donahue (1981). The atmosphere and ionosphere of Jupiter. *Vistas Astron*, *25*, 3, 315-335.

Atreya, S. K., and P. N. Romani (1985), Photochemistry and clouds of Jupiter, Saturn and Uranus, in *Planetary Meteorology*, edited.

Atreya, S. K., P. R. Mahaffy, H. B. Niemann, M. H. Wong, and T. C. Owen (2003). Composition and origin of the atmosphere of Jupiter - an update, and implications for the extrasolar giant planets. *Planet Space Sci*, *51*, 2, 105-112.

Atreya, S. K., A. S. Wong, K. H. Baines, M. H. Wong, and T. C. Owen (2005). Jupiter's ammonia clouds - localized or ubiquitous? *Planet Space Sci*, *53*, 5, 498-507.

Atreya, S. K., M. H. Wong, T. C. Owen, P. R. Mahaffy, H. B. Niemann, I. de Pater, P. Drossart, and T. Encrenaz (1999). A comparison of the atmospheres of Jupiter and Saturn: deep atmospheric composition, cloud structure, vertical mixing, and origin. *Planet Space Sci*, *47*, 10-11, 1243-1262.

Baines, K. H. (1982). Interpretation of the 6818.9Å CH4 feature observed on Uranus and Neptune. *Bulletin of the American Astronomical Society*, *14*, 760.

Baines, K. H., R. W. Carlson, and L. W. Kamp (2002). Fresh ammonia ice clouds in Jupiter - I. Spectroscopic identification, spatial distribution, and dynamical implications. *Icarus*, *159*, 1, 74-94.

Baines, K. H., M. E. Mickelson, L. E. Larson, and D. W. Ferguson (1995). The abundances of methane and ortho/para hydrogen on Uranus and Neptune - Implications of new laboratory 4-0 H-2 quadrupole line parameters. *Icarus*, *114*, 2, 328-340.

Berge, G. L., D. O. Muhleman, and R. P. Linfield (1988). Very Large Array observations of Uranus at 2.0-cm. *Astron J*, *96*, 1, 388-395.

Berry, E. X., and R. l. Reinhard (1974). Analysis of cloud drop growth by collection .4. new parameterization. *J Atmos Sci*, *31*, 8, 2127-2135.

Bezard, B., E. Lellouch, D. Strobel, J. P. Maillard, and P. Drossart (2002). Carbon monoxide on Jupiter: Evidence for both internal and external sources. *Icarus*, *159*, 1, 95-111.

Blum, J. W., G. (2008). The growth mechanisms of macroscopic bodies in protoplanetary disks. *Annu Rev Astron Astr*, *46*, 21.

Bodenheimer, P. (2006). *Planetary formation: Theory, observations, and experiments*.

Bodenheimer, P., and J. B. Pollack (1986). Calculations of the accretion and evolution of giant planets - the effects of solid cores. *Icarus*, *67*, 3, 391-408.

Borucki, W. J., A. Barnun, F. L. Scarf, A. F. Cook, and G. E. Hunt (1982). Lightning Activity on Jupiter. *Icarus*, *52*, 3, 492-502.

Boss, A. P. (2001). Gas giant protoplanet formation: Disk instability models with thermodynamics and radiative transfer. *Astrophys J*, *563*, 1, 367-373.

Boss, A. P. (2002). Formation of gas and ice giant planets. *Earth Planet Sc Lett*, *202*, 3-4, 513-523.

Bregman, J. D., D. F. Lester, and D. M. Rank (1975). Observation of Nu-2 band of PH3 in atmosphere of Saturn. *Astrophys J*, *202*, 1, L55-L56.

Briggs, F. H., and B. H. Andrew (1980). Microwave radiometry and interferometry of Uranus. *Icarus*, *41*, 2, 269-277.

Brooke, T. Y., R. F. Knacke, T. Encrenaz, P. Drossart, D. Crisp, and H. Feuchtgruber (1998). Models of the ISO 3-mu m reflection spectrum of Jupiter. *Icarus*, *136*, 1, 1-13.

Browning, K. A. (1977). *The structure and mechanism of hailstorms*, 1-39, Meteorolgical Monographs, American Meteorological Society.

Butler, B. J., and T. S. Bastian (1999). Synthesis Imaging in Radio Astronomy paper presented at Astronomical Socity of the Pacific Conference San Francisco.

Cai, K., R. H. Durisen, S. Michael, A. C. Boyle, A. C. Mejia, M. K. Pickett, and P. D'Alessio (2006). The Effects of Metallicty and Grain Size on Gravitational Instabilities in Protoplanetary disks. *Asto J.*, 636, L149-L152.

Cameron, A. G. W. (1978), Physics of the primitive solar accretion disk, in *Moons and the Planets*, edited.

Cameron, A. G. W. (1989), Comment following "The formation of the solar system: Consensus, alternaties, and missing factors," by G.W. Wetherill, in *The Formation and Evolution of Planetary Systems*, edited by H. A. Weaver and L. Danly, University of Cambridge Press, Cambridge.

Carlson, B. E., W. B. Rossow, and G. S. Orton (1988). Cloud microphysics of the giant planets. *J Atmos Sci*, *45*, 14, 2066-2081.

Cavazzoni, C., G. L. Chiarotti, S. Scandolo, E. Tosatti, M. Bernasconi, and M. Parrinello (1999). Superionic and metallic states of water and ammonia at giant planet conditions. *Science*, *283*, 5398, 44-46.

Colaprete, A., O. B. Toon, and J. A. Magalhaes (1999). Cloud formation under Mars Pathfinder conditions. *J Geophys Res-Planet*, *104*, E4, 9043-9053.

Collins, G. W., L. B. Da Silva, P. Celliers, D. M. Gold, M. E. Foord, R. J. Wallace, A. Ng, S. V. Weber, K. S. Budil, and R. Cauble (1998). Measurements of the equation of state of deuterium at the fluid insulator-metal transition. *Science*, *281*, 5380, 1178-1181.

Connerney, J. E. P., M. H. Acuna, and N. F. Ness (1987). The magnetic-field of Uranus. *J Geophys Res*, *92*, A13, 15329-15336.

Conrath, B. J., and D. Gautier (2000). Saturn helium abundance: A reanalysis of Voyager measurements. *Icarus*, *144*, 1, 124-134.

Conrath, B. J., F. M. Flasar, and P. J. Gierasch (1991). Thermal structure and dynamics of Neptune atmosphere from Voyager measurements. *J Geophys Res-Planet*, *96*, 18931-18939.

Conrath, B. J., D. Gautier, R. Hanel, G. Lindal, and A. Marten (1987a). The Helium Abundance of Uranus from Voyager Measurements. *J Geophys Res*, *92*, A13, 15003-15010.

Conrath, B. J., D. Gautier, R. Hanel, G. Lindal, and A. Marten (1987b). The helium abundance of Uranus from Voyager measurements. . *J. Geophys. Res.*, *92*, 15003-15010.

Cook, A. F., T. C. Duxbury, and G. E. Hunt (1979). 1st Results on Jovian Lightning. *Nature*, *280*, 5725, 794-794.

Courtin, R., D. Gautier, A. Marten, B. Bezard, R. Hanel (1984). The composition of Saturn's atmosphere at northern temperate latitudes for Voyager IRIS spectra: NH3, PH3, C2H2, C2H6, CH3D, CH4 and Saturian D/H isotopic ratio *Astrophys. J.*, *287*, 889.

Coustenis, A., A. Salama, E. Lellouch, T. Encrenaz, G. L. Bjoraker, R. Samuelson, T. de Graauw, H. Feuchtgruber, and M. F. Kessler (1998). Evidence for water vapor in Titan's atmosphere from ISO/SWS data. *Astron. Astrophys. Lett.*, *336*, 85-89.

CRC (1987). *CRC Handbook of Chemistry and Physics, 92nd Edition* National Institute of Standards and Technology, Boulder, Colorado.

Cunningham, E. (1910). On the velocity of steady fall of spherical particles through fluid medium. *P R Soc Lond a-Conta*, *83*, 563, 357-365.

Datchi, F., P. Loubeyre, and R. LeToullec (2000). Extended and accurate determination of the melting curves of argon, helium, ice (H2O), and hydrogen (H-2). *Phys Rev B*, *61*, 10, 6535-6546.

de Pater, I., and S. Gulkis (1988). VLA observations of Uranus at 1.3-20 cm. *Icarus*, *75*, 2, 306-323.

de Pater, I., P. N. Romani, and S. K. Atreya (1991). Possible microwave-absorption by H2S gas in Uranus and Neptune atmospheres. *Icarus*, *91*, 2, 220-233.

deGraauw, T., et al. (1997). First results of ISO-SWS observations of Saturn: Detection of CO2, CH3C2H, C4H2 and tropospheric H2O. *Astron Astrophys*, *321*, 2, L13-L16.

Delsemme, A. H., and P. Swings (1952). Hydrates de gaz dans les noyaux cométaires et les grains interstellaires. *Ann. Astrophys.*, *15*, 1-6.

Drossart, P., T. Fouchet, J. Crovisier, E. Lellouch, T. Encrenaz, H. Feuchtgruber, and J. P. Champion (1999). Fluorescence in the 3 micron bands of methane on Jupiter and Saturn from ISO/SWS observations. *Esa Sp Publ*, *427*, 169-172.

Dubrovinskaia, N., and L. Dubrovinsky (2003). Melting curve of water studied in externally heated diamond-anvil cell. *High Pressure Res*, *23*, 3, 307-311.

Dunham, E., J. L. Elliot, and P. J. Gierasch (1980). Upper-atmosphere of Uranus - mean temperature and temperature-variations. *Astrophys J*, *235*, 1, 274-284.

Dyudina, U. A., A. P. Ingersoll, G. E. Danielson, K. H. Baines, and R. W. Carlson (2001). Interpretation of NIMS and SSI images on the Jovian Cloud Structure. *Icarus*, *150*, 2, 219-233.

Dyudina, U. A., A. D. Del Genio, A. P. Ingersoll, C. C. Porco, R. A. West, A. R. Vasavada, and J. M. Barbara (2004). Lightning on Jupiter observed in the H-alpha line by the Cassini imaging science subsystem. *Icarus*, *172*, 1, 24-36.

Edelson, R. E., B. D. Madsen, E. K. Davis, and G. W. Garrison (1979). Voyager telecommunications - broadcast from Jupiter. *Science*, *204*, 4396, 913-921.

Edgington, S. G., S. K. Atreya, L. M. Trafton, J. J. Caldwell, R. F. Beebe, A. A. Simon, and R. A. West (1999). Ammonia and eddy mixing variations in the upper troposphere of Jupiter from HST Faint Object Spectrograph observations. *Icarus*, *142*, 2, 342-356.

Encrenaz, T., E. Serabyn, and E. W. Weisstein (1996). Millimeter spectroscopy of Uranus and Neptune: Constraints on CO and PH3 tropospheric abundances. *Icarus*, *124*, 2, 616-624.

Eshleman, V. R., G. L. Tyler, J. D. Anderson, G. Fjeldbo, G. S. Levy, G. E. Wood, and T. A. Croft (1977). Radio science investigations with Voyager. *Space Sci Rev*, *21*, 2, 207-232.

Fegley, B., and R. G. Prinn (1986). Chemical-models of the deep atmosphere of Uranus. *Astrophys J*, *307*, 2, 852-865.

Fegley, B., and K. Lodders (1994). Chemical-models of the deep atmospheres of Jupiter and Saturn. *Icarus*, *110*, 1, 117-154.

Feuchtgruber, H., E. Lellouch, T. deGraauw, B. Bezard, T. Encrenaz, and M. Griffin (1997). External supply of oxygen to the atmospheres of the giant planets. *Nature*, *389*, 6647, 159-162.

Feuchtgruber, H., E. Lellouch, T. Encrenaz, B. Bezard, A. Coustenis, P. Drossart, A. Salama, T. de Graauw, and G. R. Davis (1999). Oxygen in the stratospheres of the giant planets and Titan. paper presented at In The Universe as Seen by ISO, Noordwijk, The Netherlands.

Flasar, F. M., et al. (2005). Temperatures, winds, and composition in the saturnian system. *Science*, *307*, 5713, 1247-1251.

Fletcher, L. N., G. S. Orton, N. A. Teanby, and P. G. Irwin (2009a). Phosphine on Jupiter and Saturn from Cassini/CIRS. *Icarus*, *202*, 2, 543-564.

Fletcher, L. N., G. S. Orton, P. Yanamandra-Fisher, B. M. Fisher, P. D. Parrish, and P. G. Irwin (2009b). Retrievals of atmospheric variables on the gas giants from ground-based mid-infrared imaging. *Icarus*, *200*, 1, 154-175.

Forrest, W. J., et al. (2004). Mid-infrared spectroscopy of disks around classical T Tauri stars. *Astrophys J Suppl S*, *154*, 1, 443-447.

Frank, M. R., Y. W. Fei, and J. Z. Hu (2004). Constraining the equation of state of fluid H2O to 80 GPa using the melting curve, bulk modulus, and thermal expansivity of Ice VII. *Geochim Cosmochim Ac*, *68*, 13, 2781-2790.

French, R. G., and R. V. E. Lovelace (1983). Strong turbulence and atmospheric waves in stellar occultations. *Icarus*, *56*, 1, 122-146.

Fuchs, N. A. (1964). The Mechanics of Aerosols. *Pergamon, New York*.

Gautier, D., F. Hersant, O. Mousis, and J. I. Lunine (2001). Enrichments in volatiles in Jupiter: A new interpretation of the Galileo measurements (vol 550, pg L227, 2001). *Astrophys J*, *559*, 2, L183-L183.

Gautier, D., B. J. Conrath, T. Owen, I. de Pater, and S. K. Atreya (1995). The troposphere of Neptune. *Space Sci S*547-611.

Gierasch, P. J., A. Ingersoll, D. Banfield, S. Edberg, C. P. Helfenstein, A. A. Simon-Miller, A. R. Vasavada, H. H. Breneman, D. A. Senske, and G. I. Team (2000). Observation of moist convection in Jupiter's atmosphere. *Nature*, *403*, 628-630.

Gillett, F. C., and G. H. Rieke (1977). 5-20 micron observations of Uranus and Neptune. *Astrophys J*, *218*, 3, L141-L144.

Goldman, N., L. E. Fried, I. F. W. Kuo, and C. J. Mundy (2005). Bonding in the superionic phase of water. *Phys Rev Lett*, *94*, 21.

Goncharov, A. F., N. Goldman, L. E. Fried, J. C. Crowhurst, I. F. W. Kuo, C. J. Mundy, and J. M. Zaug (2005). Dynamic ionization of water under extreme conditions. *Phys Rev Lett*, *94*, 12.

Grevesse, N., M. Asplund, and A. J. Sauval (2005). The new solar chemical composition. *Eas Publications*, *17*, 21-30.

Griffith, C. A., and R. V. Yelle (1999). Disequilibrium chemistry in a brown dwarf's atmosphere: Carbon monoxide in Gliese 229B. *Astrophys J*, *519*, 1, L85-L88.

Guericke, O. v. (1672). Experimenta nova (ut vocantur) Magdeburgica de vacuo spatio. - Repreint from the first edition in Latin. Halle 2002.

Guillot, T. (1999a). A comparison of the interiors of Jupiter and Saturn. *Planet Space Sci*, *47*, 10-11, 1183-1200.

Guillot, T. (1999b). Interiors of giant planets inside and outside the Solar System. *Science*, *286*, 5437, 72-77.

Guillot, T. (2005). The interiors of giant planets: Models and outstanding questions. *Annu Rev Earth Pl Sc*, *33*, 493-530.

Gulkis, S., and I. de Pater (1984), A review of the millimeter and centimeter observations of Uranus, in *Uranus and Neptune*, edited by J. T. Bergstralh, pp. 225-262.

Gulkis, S., E. T. Olsen, M. J. Klein, and T. J. Thompson (1983). Uranus - Variability of the microwave-spectrum. *Science*, *221*, 4609, 453-455.

Gulkis, S., M. A. Janssen, and E. T. Olsen (1978). Evidence for the Depletion of Ammonia in the Uranus Atmosphere. *Icarus*, 34, 10.

Haisch, K. E., E. A. Lada, and C. J. Lada (2001). Disk frequencies and lifetimes in young clusters. *Astrophys J*, *553*, 2, L153-L156.

Hanel, R., et al. (1986). Infrared observations of the Uranian system. *Science*, *233*, 4759, 70-74.

Hansen, C. F. (1979). Viscosity and thermal conductivity of model Jupiter atmospheres. *NASA Tech. Memo., NASA-TM--78556, 24 p.*

Henning, F., and A. Stock (1921). Zeitschrift fur Physik. *4*, *226*.

Herbert, F., B. R. Sandel, R. V. Yelle, J. B. Holberg, A. L. Broadfoot, D. E. Shemansky, S. K. Atreya, and P. N. Romani (1987). The upper-atmosphere of Uranus - EUV occultations observed by Voyager-2. *J Geophys Res*, *92*, A13, 15093-15109.

Hobbs, P. V. (1974). *Ice Physics.*, *Clarendon Press, Oxford*.

Hoffman, J. P., P. G. Steffes, and D. R. DeBoer (1999). Laboratory measurements of phosphine's microwave opacity: Implications for planetary radio science. *Icarus*, *140*, 1, 235-238.

Hoffman, J. P., P. G. Steffes, and D. R. DeBoer (2001). Laboratory measurements of the microwave opacity of phosphine: Opacity formalism and application to the atmospheres of the outer planets. *Icarus*, *152*, 1, 172-184.

Hofstadter, M. D., and D. O. Muhleman (1989). Latitudinal variations of ammonia in the atmosphere of Uranus - an analysis of microwave observations. *Icarus*, *81*, 2, 396-412.

Hofstadter, M. D., and B. J. Butler (2003). Seasonal change in the deep atmosphere of Uranus. *Icarus*, *165*, 1, 168-180.

Hofstadter, M. D., and M. J. Klein (2006). Long-term variations in the microwave brightness temperature of the Uranus atmosphere. *Icarus*, *184*, 1, 170-180.

Hofstadter, M.D., B. Butler, M. Gurwell, G. Sandell, S. Atreya, and K. Mihalka (2011). Structure and variability of Uranus' troposphere. EPSC-DPS 2011 Conference Abstracts.

Holmes, N. C., W. J. Nellis, W. B. Graham, and G. E. Walrafen (1985). Spontaneous raman-scattering from shocked water. *Phys Rev Lett*, *55*, 22, 2433-2436.

Hubbard, W. B. (1981). Interiors of the giant planets. *Science*, *214*, 4517, 145-149.

Hubbard, W. B., J. C. Pearl, M. Podolak, and D. J. Stevenson (1995), Neptune and Trition, edited by D. P. Crikshank, pp. 109-138, Univiersity of Arizona Press, Tucson, AZ.

Hueso, R., and A. Sanchez-Lavega (2001). A three-dimensional model of moist convection for the giant planets: The Jupiter case. *Icarus*, *151*, 2, 257-274.

Hunten, D. M. (1975), Vertical transport in atmosphere, in *Atmospheres of earth and the planets*, edited by B. M. McCormac, Dordrecht, D. Reidel Publishing Co., Dordrecht, Holland.

Hunten, D. M. (1982). Thermal and nonthermal escape mechanisms for terrestrial bodies. *Planet Space Sci*, *30*, 8, 773-783.

Ikoma, M., K. Nakazawa, and H. Emori (2000). Formation of giant planets: Dependences on core accretion rate and grain opacity. *Astrophys J*, *537*, 2, 1013-1025.

Ingersoll, A., T. E. Dowling, P. Gierasch, G. Orton, P. L. Read, A. Sanchez-Lavega, A. P. Showman, A. A. Simon-Miller, and A. R. Vasavada (2004). *Dynamics of Jupit'er atmosphere*, Cambrigde Universtiy press, Cambridge

Irwin, P. G., L. A. Sromovsky, E. K. Strong, K. Sihra, N. A. Teanby, N. Bowles, S. B. Calcutt, and J. J. Remedios (2006). Improved near-infrared methane band models and k-distribution parameters from 2000 to 9500 cm-1 and implications for interpretation of outer planet spectra. *Icarus*, *181*, 1, 309-319.

Jaffe, W. J., G. L. Berge, T. Owen, and J. Caldwell (1984). Uranus - microwave images. *Science*, *225*, 4662, 619-621.

James, E. P., O. B. Toon, and G. Schubert (1997). A numerical microphysical model of the condensational Venus cloud. *Icarus*, *129*, 1, 147-171.

Jeans, J. H. (1929). *Astronomy and Cosmogony*. 2 ed., Cambridge University Press, Cambridge.

Johansen, A., H. Klahr, and T. Henning (2006). Gravoturbulent formation of planetesimals. *Astrophys J*, *636*, 2, 1121-1134.

Karpowicz, B. M., and P. G. Steffes (2011). In search of water vapor on Jupiter: Laboratory measurements of the microwave properties of water vapor under simulated jovian conditions (vol 212, pg 210, 2011). *Icarus*, *214*, 2, 783-783.

Kellermann, K. I. (1966). On the interpretation of radio-source spectra and the evolution of radio galaxies and quasi-stellar sources. *The Astrophysical Journal*, *146*, 621.

Kirk, R. L., and D. J. Stevenson (1987). Hydromagnetic constraints on deep zonal flow in the giant planets. *Astrophys J*, *316*, 2, 836-846.

Klein, M. J., and T. V. Seling (1966). Radio emission from Uranus at 8 Gc/S. *Astrophys J*, *146*, 2, 599-602.

Klein, M. J., and J. A. Turegano (1978). Evidence of an increase in the microwave brightness temperature of Uranus. *Astrophys.* , *224*, L31-L34.

Kunz, O., R. Klimeck, W. Wagner, and M. Jaeschke (2006). The GERG-2004 wide-range reference equation of statee for natural gases and other mixutres. Technical monograph, VDI-Verlag.

Lalas D. P., F. E. (1973). On the correct use of the wet adiabatic lapse rate in stability criteria of a saturated atmosphere. *Journal of Applied Meteorology*, *13*, 318-324.

Lellouch, E., H. Feuchtgruber, T. de Graauw, T. Encrenaz, B. Bezard, and M. Griffin (1997). Deuterium and oxygen in the giant planets. paper presented at In First ISO Workshop on Analytical Spectroscopy, Noordwijk, The Netherlands.

Lellouch, E., H. Feuchtgruber, T. Encrenaz, B. Bezard, P. Drossart, M. Griffin, and G. R. Davis (1998). D/H ratio and oxygen source: A Jupiter-Saturn comparison. paper presented at In The Jovian System After Galileo. The Saturnian System before Cassini–Huygens, International Symposium, Nantes, 11–15 May 1998.

Lellouch, E., B. Bezard, J. I. Moses, G. R. Davis, P. Drossart, H. Feuchtgruber, E. A. Bergin, R. Moreno, and T. Encrenaz (2002). The origin of water vapor and carbon dioxide in Jupiter's stratosphere. *Icarus*, *159*, 1, 112-131.

Lemmon, E. W., and R. T. Jacobsen (2004). Equations of state for mixtures of R-32, R-125, R-134a, R-143a, and R-152a. *J Phys Chem Ref Data*, *33*, 2, 593-620.

Levin, Z., W. J. Borucki, and O. B. Toon (1983). Lightning Generation in Planetary-Atmospheres. *Icarus*, *56*, 1, 80-115.

Lewis, J. S. (1969). The clouds of Jupiter and the NH3-H2O and NH3-H2S systems. *Icarus*, *10*.

Lewis, J. S., and R. G. Prinn (1980). Kinetic inhibition of Co and N-2 reduction in the solar nebula. *Astrophys J*, *238*, 1, 357-364.

Lin, J. F., B. Militzer, V. V. Struzhkin, E. Gregoryanz, R. J. Hemley, and H. K. Mao (2004). High pressure-temperature Raman measurements of H2O melting to 22 GPa and 900 K. *J Chem Phys*, *121*, 17, 8423-8427.

Lindal, G. F., J. R. Lyons, D. N. Sweetnam, V. R. Eshleman, D. P. Hinson, and G. L. Tyler (1987). The atmosphere of Uranus - results of radio occultation measurements with Voyager-2. *J Geophys Res*, *92*, A13, 14987-15001.

Little, B., C. D. Anger, A. P. Ingersoll, A. R. Vasavada, D. A. Senske, H. H. Breneman, W. J. Borucki, and G. S. Team (1999). Galileo images of lightning on Jupiter. *Icarus*, *142*, 2, 306-323.

Lunine, J. I., and D. M. Hunten (1987). Moist Convection and the Abundance of Water in the Troposphere of Jupiter. *Icarus*, *69*, 3, 566-570.

Lunine, J. I., W. B. Hubbard, A. Burrows, Y. P. Wang, and K. Garlow (1989). The effect of gas and grain opacity on the cooling of brown dwarfs. *Astrophys J*, *338*, 1, 314-337.

Macy, W., and W. Sinton (1977). Detection of methane and ethane emission on Neptune but not on Uranus. *Astrophys J*, *218*, 2, L79-L81.

Magalhaes, J. A., A. Seiff, and R. E. Young (2002). The stratification of Jupiter's troposphere at the Galileo probe entry site. *Icarus*, *158*, 2, 410-433.

Mahaffy, P. R., H. B. Niemann, A. Alpert, S. K. Atreya, J. Demick, T. M. Donahue, D. N. Harpold, and T. C. Owen (2000). Noble gas abundance and isotope ratios in the atmosphere of Jupiter from the Galileo Probe Mass Spectrometer. *J Geophys Res-Planet*, *105*, E6, 15061-15071.

Marley, M. S., C. Gelino, D. Stephens, J. I. Lunine, and R. Freedman (1999). Reflected spectra and albedos of extrasolar giant planets. I. Clear and cloudy atmospheres. *Astrophys J*, *513*, 2, 879-893.

Massie, S. T., and D. M. Hunten (1982). Conversion of para-hydrogen and ortho-hydrogen in the Jovian planets. *Icarus*, *49*, 2, 213-226.

Mayer, L., T. Quinn, J. Wadsley, and J. Stadel (2004). The evolution of gravitationally unstable protoplanetary disks: Fragmentation and possible giant planet formation. *Astrophys J*, *609*, 2, 1045-1064.

Mccready, L. L., J. L. Pawsey, and R. Paynescott (1947). Solar Radiation at Radio Frequencies and Its Relation to Sunspots. *Proc R Soc Lon Ser-A*, *190*, 1022, 357-375.

Michaud, G., D. Tarasick, Y. Charland, and C. Pelletier (1983). Diffusion, meridional circulation, and mass-loss in fm-am stars. *Astrophys J*, *269*, 1, 239-249.

Michelangeli, D. V., O. B. Toon, R. M. Haberle, and J. B. Pollack (1993). Numerical simulations of the formation and evolution of water ice clouds in the Martian atmosphere. *Icarus*, *102*, 2, 261-285.

Mihalka, K.M., M.D. Hofstadter, S.K. Atreya, K. H. Baines, B. J. Butler, M. A. Gurwell, and M. Hitzig (in prep). Evidence for phopshine in the upper troposphere of Uranus.

Miller, S. L. (1961). A theory of gaseous anesthetics. *Proc. Nat. Acad. Sci.*, *47*, 9, 1515-1524.

Moseley, H., B. Conrath, and R. F. Silverberg (1985). Atmospheric-temperature profiles of Uranus and Neptune. *Astrophys J*, *292*, 2, L83-L86.

Moses, J. I., B. Bezard, E. Lellouch, G. R. Gladstone, H. Feuchtgruber, and M. Allen (2000). Photochemistry of Saturn's atmosphere - I. Hydrocarbon chemistry and comparisons with ISO observations. *Icarus*, *143*, 2, 244-298.

Murphy, J. R., J. B. Pollack, R. M. Haberle, C. B. Leovy, O. B. Toon, and J. Schaeffer (1995). Three-dimensional numerical simulation of Martian global dust storms. *J Geophys Res-Planet*, *100*, E12, 26357-26376.

Nellis, W. J., S. T. Weir, and A. C. Mitchell (1999). Minimum metallic conductivity of fluid hydrogen at 140 GPa (1.4 Mbar). *Phys Rev B*, *59*, 5, 3434-3449.

Niemann, H. B., et al. (1998a). The composition of the Jovian atmosphere as determined by the Galileo probe mass spectrometer. *J Geophys Res-Planet*, *103*, E10, 22831-22845.

Niemann, H. B., et al. (1998b). Chemical composition measurements of the atmosphere of Jupiter with the Galileo Probe mass spectrometer. *Adv Space Res*, *21*, 11, 1455-1461.

Normand, C. (1946). Energy in the Atmosphere. *Quart. J. R. Met. Soc.*, *72*, 145.

Orton, G. S. (1986). Thermal spectrum of Uranus - Implications for large helium abundance. *Science*, *231*, 4740, 836-840.

Orton, G. S., A. T. Tokunaga, and J. Caldwell (1983). Observational constraints on the atmospheres of Uranus and Neptune from new measurements near 10-mu-m. *Icarus*, *56*, 1, 147-164.

Palotai, C., and T. E. Dowling (2008). Addition of water and ammonia cloud microphysics to the EPIC model. *Icarus*, *194*, 1, 303-326.

Pickett, H. M., R. L. Poynter, and E. A. Cohen (1981). Pressure broadening of phosphine by hydrogen and helium. *J Quant Spectrosc Ra*, *26*, 3, 197-198.

Podolak, M. (2003). The contribution of small grains to the opacity of protoplanetary atmospheres. *Icarus*, *165*, 2, 428-437.

Podolak, M., W. B. Hubbard, and D. J. Stevenson (1991a), Model of Uranus' interior and magnetic field, in *Uranus*, edited by J. T. Bergstralh, E. D. Miner and M. S. Matthews, pp. 29-61, Univ. of Arizona Press, Tuscon, Az.

Podolak, M., W. B. Hubbard, and D. Stevens (1991b). *Models of Uranus' interior and magnetic field*, 29-64.

Podolak, M., A. Weizman, and M. Marley (1995). Comparative models of Uranus and Neptune. *Planet Space Sci*, *43*, 12, 1517-1522.

Pollack, J. B., and P. Bodenheim (1989), Theories of the origin and evolution of the giant planets in *Origin and Evolution of Planetary and Satellite Atmospheres.* , edited by S. K. Atreya, J. B. Pollack and M. S. Matthews, pp. 564-602, University of Arizona Press, Tuscon.

Pollack, J. B., O. Hubickyj, P. Bodenheimer, J. J. Lissauer, M. Podolak, and Y. Greenzweig (1996). Formation of the giant planets by concurrent accretion of solids and gas. *Icarus*, *124*, 1, 62-85.

Prandtl, L. (1953). Essentails of Fluid Dynamics. *Blackie, London*.

Prinn, R. G., and J. S. Lewis (1973). Uranus atmosphere - structure and composition. *Astrophys J*, *179*, 1, 333-342.

Prinn, R. G., and S. S. Barshay (1977). Carbon-monoxide on Jupiter and implications for atmospheric convection. *Science*, *198*, 4321, 1031-1034.

Prinn, R. G., and E. P. Olaguer (1981). Nitrogen on Jupiter - a deep atmospheric source. *J Geophys Res-Oc Atm*, *86*, Nc10, 9895-9899.

Prinn, R. G., and B. Fegley (1989). *Solar nebula chemistry: origin of planetary, satellite, and comentary volatiles*, 78-136, Univ. of Arizona press, Tucson.

Pruppacher, H. R., and J. D. Klett (1978). *Microphysics of Clouds and Precipitation*, D. Reidel Publishing Company, Dordrecht, Holland.

Ragent, B., D. S. Colburn, K. A. Rages, T. C. D. Knight, P. Avrin, G. S. Orton, P. A. Yanamandra-Fisher, and G. W. Grams (1998). The clouds of Jupiter: Results of the

Galileo Jupiter Mission Probe Nephelometer Experiment. *J Geophys Res-Planet*, *103*, E10, 22891-22909.

Refsdal, A. (1930). Der feuchtlabile Niederschlag. *Geofys. Publ.*, *5*, 12.

Reuter, D. C., et al. (2007). Jupiter cloud composition, stratification, convection, and wave motion: A view from new horizons. *Science*, *318*, 5848, 223-225.

Richling, S., D. Hollenbach, and H. Yorke (2006), Theory, Observations, and Experiments, in *Planet Formation*, edited by H. Klahr and W. Brander.

Ridgway, S. T., L. Wallace, and G. R. Smith (1976). 800-1200 Inverse centimeter absorption-spectrum of Jupiter. *Astrophys J*, *207*, 3, 1002-1006.

Roos-Serote, M., S. K. Atreya, M. K. Wong, and P. Drossart (2004). On the water abundance in the atmosphere of Jupiter. *Planet Space Sci*, *52*, 5-6, 397-414.

Rossow, W. B. (1978). Cloud microphysics - analysis of clouds of Earth, Venus, Mars, and Jupiter. *Icarus*, *36*, 1, 1-50.

Saumon, D., and T. Guillot (2004). Shock compression of deuterium and the interiors of Jupiter and Saturn. *Astrophys J*, *609*, 2, 1170-1180.

Schwegler, E., G. Galli, and F. Gygi (2000). Water under pressure. *Phys Rev Lett*, *84*, 11, 2429-2432.

Schwegler, E., G. Galli, F. Gygi, and R. Q. Hood (2001). Dissociation of water under pressure. *Phys Rev Lett*, *87*, 26.

Seiff, A., D. B. Kirk, T. C. D. Knight, R. E. Young, J. D. Mihalov, L. A. Young, F. S. Milos, G. Schubert, R. C. Blanchard, and D. Atkinson (1998). Thermal structure of Jupiter's atmosphere near the edge of a 5-mu m hot spot in the north equatorial belt. *J Geophys Res-Planet*, *103*, E10, 22857-22889.

Simon-Miller, A. A., B. Conrath, P. J. Gierasch, and R. F. Beebe (2000). A detection of water ice on Jupiter with Voyager IRIS. *Icarus*, *145*, 2, 454-461.

Simon-Miller, A. A., N. J. Chanover, G. S. Orton, M. Sussman, I. G. Tsavaris, and E. Karkoschka (2006). Jupiter's white oval turns red. *Icarus*, *185*, 2, 558-562.

Smith, B. A., et al. (1979). Galilean Satellites and Jupiter - Voyager-2 Imaging Science Results. *Science*, *206*, 4421, 927-950.

Smith, B. A., et al. (1989). Voyager-2 at Neptune - Imaging science results. *Science*, *246*, 4936, 1422-1449.

Sromovsky, L. A., and P. M. Fry (2010a). The source of widespread 3-mu m absorption in Jupiter's clouds: Constraints from 2000 Cassini VIMS observations. *Icarus*, *210*, 1, 230-257.

Sromovsky, L. A., and P. M. Fry (2010b). The source of 3-mu m absorption in Jupiter's clouds: Reanalysis of ISO observations using new NH(3) absorption models. *Icarus*, *210*, 1, 211-229.

Sromovsky, L. A., P. G. J. Irwin, and P. M. Fry (2006). Near-IR methane absorption in outer planet atmospheres: Improved models of temperature dependence and implications for Uranus cloud structure. *Icarus*, *182*, 2, 577-593.

Sromovsky, L. A., P. M. Fry, H. B. Hammel, I. de Pater, K. A. Rages, and M. R. Showalter (2007). Dynamics, evolution, and structure of Uranus' brightest cloud feature. *Icarus*, *192*, 2, 558-575.

Stephenson, C. C., and W. F. Giaque (1937). A test of the third law of thermodynamics by means of two crystalline forms of phosphine: The heat capacity, heat of vaporization, and vapor pressure of phosphine. Entropy of the gas. *J. Chem. Phys.*, *5*, 149-158.

Stevenson, D. J. (1984). On forming the gian planets quickly (superganymedian puffballs!). *Lunar Planet. Sci.* , *15*, 822-823.

Stoker, C. R. (1986). Moist Convection - a Mechanism for Producing the Vertical Structure of the Jovian Equatorial Plumes. *Icarus*, *67*, 1, 106-125.

Stone, P. H. (1976), The Meterology of the jovian atmosphere, in *Jupiter*, edited by T. Gehrels, pp. 586-618, University of Arizona Press, Tucson.

Strom, K. M., S. E. Strom, S. Edwards, S. Cabrit, and M. F. Skrutskie (1989). Circumstellar material associated with solar-type pre-main-sequence stars - a possible constraint on the timescale for planet building. *Astron J*, *97*, 5, 1451-1470.

Stull, D. R. (1947). Industrial & Engineering Chemistry. *39*, *517*.

Sugiyama, K., M. Odaka, K. Kuramoto, and Y. Y. Hayashi (2006). Static stability of the Jovian atmospheres estimated from moist adiabatic profiles. *Geophys Res Lett*, *33*, 3.

Sutton, O. G. (1932). A Theory of Eddy Diffusion in the Atmosphere. *Proceedings of the Royal Societ of London. Series A, Containing Papers of a Mathematical and Physical Character*, *135*, 826, 143-165.

Tokunaga, A. T., G. S. Orton, and J. Caldwell (1983). New observational sonstraints on the temperature inversions of Uranus and Neptune. *Icarus*, *53*, 1, 141-146.

Toon, O. B., C. P. Mckay, C. A. Griffith, and R. P. Turco (1992). A physical model of Titans aerosols. *Icarus*, *95*, 1, 24-53.

Toon, O. B., R. P. Turco, P. Hamill, C. S. Kiang, and R. C. Whitten (1979). One-Dimensional Model Describing Aerosol Formation and Evolution in the Stratosphere .2. Sensitivity Studies and Comparison with Observations. *J Atmos Sci*, *36*, 4, 718-736.

Toon, O. B., R. P. Turco, D. Westphal, R. Malone, and M. S. Liu (1988). A Mmltidimensional model for aerosols - Description of computational analogs. *J Atmos Sci*, *45*, 15, 2123-2143.

Turco, R. P., P. Hamill, O. B. Toon, R. C. Whitten, and C. S. Kiang (1979). One-Dimensional model describing aerosol formation and evolution in the stratosphere .1. physical processes and mathematical analogs. *J Atmos Sci*, *36*, 4, 699-717.

Turcotte, S., and R. F. Wimmer-Schweingruber (2002). Possible in situ tests of the evolution of elemental and isotopic abundances in the solar convection zone. *J Geophys Res*, *107*, A12.

Turcotte, S., J. Richer, G. Michaud, C. A. Iglesias, and F. J. Rogers (1998). Consistent solar evolution model including diffusion and radiative acceleration effects. *Astrophys J*, *504*, 1, 539-558.

Tyler, G. L., D. N. Sweetnam, J. D. Anderson, J. K. Campbell, V. R. Eshleman, D. P. Hinson, G. S. Levy, G. F. Lindal, E. A. Marouf, and R. A. Simpson (1986). Voyager-2 radio science observations of the Uranian system - Atmosphere, rings, and satellites. *Science*, *233*, 4759, 79-84.

Udry, S., and N. C. Santos (2007). Statistical properties of exoplanets. *Annu Rev Astron Astr*, *45*, 397-439.

United States Committee on Extension to the Standard Atmosphere (1976). *U.S. standard atmosphere 1976* U.S. Govt. Print. Off., Washington.

Waller, A. (1847). Microscopic Observations on the so-called vesicular vapours of water, as existing in the vapours of steam, and in clouds. *Philosophical Transactions of the Royal Society of London*, *137*, 23-30.

Weidenschilling, S. J., and J. S. Lewis (1973). Atmospheric and cloud structures of Jovian planets. *Icarus*, *20*, 4, 465-476.

Weir, S. T., A. C. Mitchell, and W. J. Nellis (1996). Metallization of fluid molecular hydrogen at 140 GPa (1.4 mbar). *Phys Rev Lett*, *76*, 11, 1860-1863.

Weisstein, E. W., and E. Serabyn (1994). Detection of the 267 Ghz J=1-0 rotational transition of PH3 in Saturn with a new frourier-transform spectrometer. *Icarus*, *109*, 2, 367-381.

Weisstein, E. W., and E. Serabyn (1996). Submillimeter line search in Jupiter and Saturn. *Icarus*, *123*, 1, 23-36.

Wiktorowicz, S. J., and A. P. Ingersoll (2007). Liquid water oceans in ice giants. *Icarus*, *186*, 2, 436-447.

Wong, M. H., G. L. Bjoraker, M. D. Smith, F. M. Flasar, and C. A. Nixon (2004a). Identification of the 10-mu m ammonia ice feature on Jupiter. *Planet Space Sci*, *52*, 5-6, 385-395.

Wong, M. H., P. R. Mahaffy, S. K. Atreya, H. B. Niemann, and T. C. Owen (2004b). Updated Galileo probe mass spectrometer measurements of carbon, oxygen, nitrogen, and sulfur on Jupiter. *Icarus*, *171*, 1, 153-170.

Wong, M. H., I. de Pater, X. Asay-Davis, P. W. Marcus, and C. Y. Go (2011). Vertical structure of Jupiter's Oval BA before and after it reddened: What changed? *Icarus*, *215*, 211-225.

Wong, M. H., K. M. Mihalka, S. K. Atreya, W. R. Kuhn, and P. N. Romani (2012). Revised method for calculating cloud densities in equilibrium models. In preparation.

Wuchterl, G. (1995). Giant planet formation - A comparative view of gas-accretion. *Earth Moon Planets*, *67*, 1-3, 51-65.

Young, R. E. (2003). The Galileo probe: how it has changed our understanding of Jupiter. *New Astron Rev*, *47*, 1, 1-51.

Zuchowski, L. C., Y. H. Yamazaki, and P. L. Read (2009). Modeling Jupiter's cloud bands and decks 2. Distribution and motion of condensates. *Icarus*, *200*, 2, 563-573.